UNIVERSITY OF CALIFORNIA SAN DIEGO

# Gravity from altimetry, bathymetry from gravity, and tectonics from space

A dissertation submitted in partial satisfaction of the
requirements for the degree Doctor of Philosophy

in

Earth Sciences

by

Hugh Harper

Committee in charge:

Professor David T. Sandwell, Chair
Professor Jeff Gee
Professor Dave May
Professor Ross Parnell-Turner
Professor Jose Restrepo

2023

Copyright

Hugh Harper, 2023

All rights reserved.

The Dissertation of Hugh Harper is approved, and it is acceptable in quality and form for publication on microfilm and electronically.

University of California San Diego

2023

DEDICATION

*To Fig*

TABLE OF CONTENTS

LIST OF FIGURES

ACKNOWLEDGEMENTS

I have many thanks to give, more than I could hope to express.

First of all, I want to thank my advisor David Sandwell, who is immeasurably generous and a strong advocate for me and all of his students. He is, for many reasons, a legend at Scripps, and I feel very lucky to have had him as a mentor.

I want to also thank my co-authors who, during our relatively brief collaborations, have been great mentors to me. I was fortunate to have the guidance of Brook Tozer in my first few years here, who went out of his way on my behalf. Sometimes when a project isn't working out like you hoped, it's not at all clear where you're headed or even what your next move is. Karen Luttrell has a way of cutting through this fog, and she helped me to organize my thoughts and process and to turn my jumbled thoughts into something coherent.

I thank my committee members–Jeff Gee, Dave May, Ross Parnell-Turner, and Jose Restrepo–for their patience and honesty, and for their feedback on manuscripts. A special thanks to Ross who welcomed me into his marine geophysics group meetings.

Things are a lot easier if you're among friends, and I was always among friends here. I understand that is not always true in graduate school, so I am very grateful for my IGPP cohort, my colleagues in the Sandwell lab, and many others at IGPP whom I am happy to call my friends. Because of them, I feel that time has passed too quickly.

Finally, I want to thank my family and my girlfriend, Grayson. They are the most important people to me.

Chapter 1, in full, is a reprint of the material as it appears in the Journal of Geophysical Research Solid Earth: Harper, H., Tozer, B., Sandwell, D. T., Hey, R. N. "Marine vertical gravity gradients reveal the global distribution and tectonic significance of "seesaw" ridge propagation", *JGR: Solid Earth*, 2021. The dissertation author was the primary investigator and author of this paper.

Chapter 2, in full, is a reprint of material that has been submitted for publication in the Journal of Geophysical Research Solid Earth: Harper, H.; Luttrell, K.; Sandwell, D. T. "Ridge

propagation and the stability of small mid-ocean ridge offsets", in rev. The dissertation author was the primary investigator and author of this paper.

Chapter 3, in full, is currently being prepared for publication as Harper, H. and Sandwell, D. T. "Global predicted bathymetry using neural networks". The dissertation author was the primary investigator and author of this material.

## VITA

2015 B. S. in Geology, Appalachian State University

2017 M. S. in Geophysics, University of Alaska, Fairbanks

2023 Ph. D. in Earth Sciences, University of California San Diego

## PUBLICATIONS

**Harper, H.** and Sandwell, D. T. "Global predicted bathymetry using neural networks", in prep.

**Harper, H.**; Luttrell, K.; Sandwell, D. T. "Ridge propagation and the stability of small mid-ocean ridge offsets", *in review*

Devine, S.; **Harper, H.**; Marshall, S. T. "Mechanical Models of Fault-Slip Rates in the Transverse and Peninsular Ranges, California", *Seismological Research Letters*, 2022

Sandwell, D. T.; Goff, J. A.; Gevorgian, J.; **Harper, H.**; Kim, S-.S.; Yu, Y.; Tozer, B.; Wessel, P.; Smith, W. H. F. "Improved bathymetric prediction using geological information: SYNBATH", *Earth and Space Science*, 2022

Sandwell, D. T.; **Harper, H.**; Tozer, B.; Smith, W. H. F. "Gravity field recovery from geodetic altimeter missions", *Advances in Space Research*, 2021

**Harper, H.**; Tozer, B.; Sandwell, D. T.; Hey, R. N. "Marine vertical gravity gradients reveal the global distribution and tectonic significance of "seesaw" ridge propagation", *JGR: Solid Earth*, 2021

Watts, A. B.; Tozer, B.; **Harper, H.**; Boston, B.; Shillington, D. J.; Dunn, R. "Evaluation of shipboard and satellite-derived bathymetry and gravity data over seamounts in the northwest Pacific Ocean", *JGR: Solid Earth*, 2020

ABSTRACT OF THE DISSERTATION

Gravity from altimetry, bathymetry from gravity, and tectonics from space

by

Hugh Harper

Doctor of Philosophy in Earth Sciences

University of California San Diego, 2023

Professor David T. Sandwell, Chair

The ocean floor, more than 70% of the solid earth surface, remains mostly unmapped by conventional echo-sounding methods. Measurements from satellite altimetry precipitated maps of marine gravity with uniform global coverage which have improved markedly as repeated measurements have reduced noise. Such maps allow us to see the ocean floor that was previously hidden.

The structures revealed on the seafloor reflect processes of plate tectonics. We describe a new type of tectonic feature revealed in maps of marine vertical gravity gradient (VGG). So-called seesaw propagators reflect ridge propagation that reverses direction. SSPs are ubiquitous on seafloor that formed at half spreading rates between 10–40 mm $yr^{-1}$, their propagation

directions do not appear to be correlated over large length scales, and they occur where the ridge offset is less than 30 km. This suggests the yield strength of the lithosphere at large MOR offsets prevents propagation. We develop a model framework based on a force balance wherein forces driving propagation must exceed the integrated shear strength of the offset zone. We apply this model framework to 4 major propagating ridges, 55 seesaw propagating ridges, and 69 transform faults. The model correctly predicts the migration of major propagating ridges and the stability of transform faults, but the results for SSPs are less accurate. This model framework simplifies deformation in the shear zone, but can possibly explain why non-transform deformation is preferred at short offsets.

Finally, we give a new method for predicting bathymetry from gravity using a machine learning approach. We design and train a neural network on a collection of 50 million depth soundings to predict bathymetry globally using gravity anomalies. Our final predicted depth model improves on the old predicted model rms by 18%, from 165 m to 136 m. Additionally, we recommend a strategy for partitioning depth sounding data such that the problem conforms with the assumption of data independence required by many machine learning algorithms.

# Introduction

It's well known, even among laypeople, that only a small portion of our world's oceans have been explored. It's familiar to hear that we know more about the surfaces of nearby planets than we do about the abyss here at home. Because this is a fact, it's hard to outright object, but I do think it gives the wrong impression sometimes. What I mean to say is it's not the whole story, and we do know a bit more about the ocean floor than the statement might suggest.

Why is it important that we know the structure of the seafloor? From a human/societal perspective, such knowledge is essential to establishing international boundaries and determining law of the sea (Jakobsson et al.; 2003); for commercial purposes like seafloor mining (e.g. Ellis et al.; 2017) or fiber optic cable routing (Wölfl et al.; 2019); and for understanding and avoiding navigational hazards. Maybe the most striking examples of the latter are high-profile submarine groundings of recent memory (USS San Francisco in 2005, USS Connecticut in 2021) which quite clearly suggest a need for reasonable depth maps. There are equally good reasons from a more purely scientific point of view. Various aspects of modeling in ocean science, such as tidally-generated ocean mixing (e.g. Goff and Arbic; 2010) or tsunami propagation (Sepúlveda et al.; 2020) depend on knowledge of bathymetry. From a solid earth perspective, the seafloor structure is useful in studying plate tectonics (e.g. Müller et al.; 2018). It was in the oceans that the theory of plate tectonics took its shape (e.g. Kearey et al.; 2009), and maps of the seafloor can still reveal many subtleties of plate creation and destruction.

If only a small fraction of the seafloor has been mapped, and mapping the gaps is many years and many millions of dollars away, then what are the means by which we can infer the structure of the seafloor? To address the scarcity of depth measurements in the oceans, we have

a powerful tool in gravity. Because of the density contrast of rock and water, we can relate small changes in the influence of gravity to the depth of the water column. Although this idea was first suggested by Siemens (1876), it would be 100 years before such a tool existed that could fully exploit this relationship. Following the advent of satellite altimeters, which could recover the marine gravity field from space, Dixon et al. (1983) showed the feasibility of bathymetric prediction from gravity. The following decade, such a mapping of the oceans was a reality (Smith and Sandwell; 1994, 1997).

The principles of altimetry over the oceans are straightforward. The instrument measures the two-way travel time of a radar pulse between itself and the sea surface and converts this to a range. To determine the sea surface height (SSH), the ranging measurement is subtracted from the distance of the satellite to some reference surface (the reference ellipsoid). The true SSH anomaly is a combination of several phenomena operating at different length and time scales (e.g. Sandwell; 1991), but for the purposes of solid earth gravity recovery, oceanographic signals such as dynamic topography (e.g. Nerem and Koblinsky; 1993) are considered noise. The time-independent signal corresponds to the geoid–a theoretical surface of gravity equipotential.

By taking the slope of the SSH measurement along the track of the satellite, we reduce the long wavelength signal and noise and the biases inherent in the absolute height measurement (Smith; 1998). We decompose the along-track slope into north and east deflections of the vertical (where the vertical is normal to the ellipsoid), and a solution of Laplace's equation allows us to recover gravity anomaly (e.g. Haxby et al.; 1983; Sandwell; 1992; Smith; 1998). A 1 $\mu$rad deflection corresponds to approximately 1 mgal. While the native range precision of an altimeter is nowhere near this level, we can approach this precision with waveform retracking and repeat profile stacking (e.g. Sandwell and Smith; 2005; Garcia et al.; 2014).

Short wavelength gravity anomalies on the sea floor are rapidly attenuated by upward continuation to the sea surface (Parker; 1972), limiting the resolution of recovered features to a few times the regional water depth. To directly quote Smith (1998): "The value of satellite altimeter data for tectonic studies is not the clarity with which individual structures are imaged,

but the fact that the technique provides nearly global coverage with essentially uniform resolution." Gravity-based maps of the seafloor have revealed, on a grand scale: the distribution of seamounts (e.g. Kim and Wessel; 2011; Gevorgian et al.; 2023); thermal contraction-induced gravity rolls (Sandwell and Fialko; 2004); mid-ocean ridge segmentation, fabrics related to spreading rate (Small and Sandwell; 1994), and associated features such as fracture zones (e.g Matthews et al.; 2011) and propagating ridges (e.g. Morgan and Sandwell; 1994). An investigation of a class of propagating ridges is the subject of the first two chapters.

In chapter 1, we analyze new satellite-derived vertical gravity gradient (VGG) data, which reveal an abundance of off-axis seafloor features that are oblique to ridges and transform faults and thus reflect the occurrence of ridge propagation at some segment boundaries. However, unlike many propagating ridges, these features commonly reverse direction leaving W-shaped signatures in the seafloor which we refer to as "seesaw propagators" (SSPs). Using the VGG, we document these features globally and find that: (1) SSPs are ubiquitous on seafloor that formed at half spreading rates between 10–40 mm $yr^{-1}$ and their total length is about 1/3 that of fracture zones. (2) The lithospheric age offset across SSPs (0–2.5 Ma) is less than transform faults (2–10 Ma), which likely reflects a rheological threshold, whereby only young and weak lithosphere allows for "non-rigid" SSP behavior. (3) Isostatic modelling of well-surveyed SSPs confirms that they formed on young and thin (3 km) lithosphere. (4) The directional changes of SSPs in both time and space appear largely uncorrelated and cannot be explained by previous regional-scale models invoked to explain unidirectional ridge propagation and thus require a different driving force.

In chapter 2, we continue the investigation of SSPs, focusing on the ridge offset length of such features. For slow- and intermediate-spreading ridges, there appears to be an offset length threshold above which adjacent ridges do not propagate so remain as stable transform faults. We propose this threshold is due to the yield strength of the lithosphere, and we develop a model framework based on a force balance wherein forces driving propagation must exceed the integrated shear strength of the offset zone. We apply this model framework to 4 major

propagating ridges, 55 seesaw propagating ridges, and 69 transform faults. The model correctly predicts the migration of major propagating ridges and the stability of transform faults, but the results for SSPs are less accurate. Model predictions for direction of ridge propagation are mixed as well. This model framework simplifies deformation in the shear zone, but can possibly explain why non-transform deformation is preferred at short offsets.

While recovery of the gravity field is independently of great use in studying tectonics, it's through a combination of shipboard measurements of depth and gravity that we can infer the depth of the seafloor. The third chapter describes a machine learning-based update to the depth prediction method established by Smith and Sandwell (1994). We design and train a neural network on a collection of 50 million depth measurements to predict bathymetry globally using gravity anomalies. We find the best result is achieved by pre-filtering depth and gravity in accordance with the admittance theory given by Smith and Sandwell (1994). Our final predicted depth model improves on the old predicted model RMSE by 16%, from 165 m to 138 m. Additionally, we recommend a strategy for partitioning a dataset such that the problem conforms with the assumption of data independence required by many machine learning algorithms.

# References


Dixon, T. H., Naraghi, M., McNutt, M. K. and Smith, S. M. (1983). Bathymetric prediction from seasat altimeter data, *Journal of Geophysical Research* **88**: 1563–1571.

Ellis, J., Clark, M., Rouse, H. and Lamarche, G. (2017). Environmental management frameworks for offshore mining: the new zealand approach, *Marine Policy* **84**: 178–192.

Garcia, E. S., Sandwell, D. T. and Smith, W. H. (2014). Retracking cryosat-2, envisat and jason-1 radar altimetry waveforms for improved gravity field recovery, *Geophysical Journal International* **196**(3): 1402–1422.

Gevorgian, J., Sandwell, D. T., Yu, Y., Kim, S.-S. and Wessel, P. (2023). Global distribution and morphology of small seamounts, *Earth and Space Science* **10**(4): e2022EA002331. e2022EA002331 2022EA002331.

Goff, J. A. and Arbic, B. K. (2010). Global prediction of abyssal hill roughness statistics for use in ocean models from digital maps of paleo-spreading rate, paleo-ridge orientation, and sediment thickness, *Ocean Modelling* **32**: 36–43.
**URL:** *http://dx.doi.org/10.1016/j.ocemod.2009.10.001*

Haxby, W. F., Karner, G. D., LaBrecque, J. L. and Weissel, J. K. (1983). Digital images of combined oceanic and continental data sets and their use in tectonic studies, *Eos, Transactions American Geophysical Union* **64**: 995–1004.

Jakobsson, M., Mayer, L. A. and Armstrong, A. (2003). Analysis of data relevant to establishing outer limits of a continental shelf under law of the sea article 76.

Kearey, P., Klepeis, K. A. and Vine, F. J. (2009). *Global Tectonics*, 3 edn, John Wiley & Sons Ltd.

Kim, S. S. and Wessel, P. (2011). New global seamount census from altimetry-derived gravity data, *Geophysical Journal International* **186**: 615–631.

Matthews, K. J., Muller, R. D., Wessel, P. and Whittaker, J. M. (2011). The tectonic fabric of the ocean basins, *Journal of Geophysical Research: Solid Earth* **116**: 1–28.

Morgan, J. P. and Sandwell, D. T. (1994). Systematics of ridge propagation south of 30 degrees s, *Earth and Planetary Science Letters* **121**.

Müller, R. D., Matthews, K. J. and Sandwell, D. T. (2018). Advances in imaging small-scale seafloor and sub-seafloor tectonic fabric using satellite altimetry, *in* D. Stammer and A. Cazenave (eds), *Satellite Altimetry Over Oceans and Land Surfaces*, CRC Press, Boca

Raton, pp. 523–546.

Nerem, R. S. and Koblinsky, C. J. (1993). The geoid and ocean circulation, *Geoid and Its Geophysical Interpretations*, CRC press, pp. 321–335.

Parker, R. L. (1972). The rapid calculation of potential anomalies, *Geophysical Journal of the Royal Astronomical Society* **31**: 447–455.

Sandwell, D. and Fialko, Y. (2004). Warping and cracking of the pacific plate by thermal contraction, *Journal of Geophysical Research: Solid Earth* **109**: 1–12.

Sandwell, D. T. (1991). Geophysical applications of satellite altimetry, *Reviews of Geophysics* **29**(S1): 132–137.

Sandwell, D. T. (1992). Antarctic marine gravity field from high-density satellite altimetry, *Geophysical Journal International* **109**: 437–448.

Sandwell, D. T. and Smith, W. H. (2005). Retracking ers-1 altimeter waveforms for optimal gravity field recovery, *Geophysical Journal International* **163**(1): 79–89.

Sepúlveda, I., Tozer, B., Haase, J. S., Liu, P. L.-F. and Grigoriu, M. (2020). Modeling uncertainties of bathymetry predicted with satellite altimetry data and application to tsunami hazard assessments, *Journal of Geophysical Research: Solid Earth* **125**(9): e2020JB019735.

Siemens, C. (1876). On determining the depth of the sea without the use of a sounding line, london: Philos, *Trans R. Soc. London* .

Small, C. and Sandwell, D. T. (1994). Imaging mid-ocean ridge transitions with satellite gravity, *Geology* **22**: 123–126.

Smith, W. H. F. (1998). Seafloor tectonic fabric from satellite altimetry, *Annual Review of Earth and Planetary Sciences* **26**: 697–738.

Smith, W. H. and Sandwell, D. T. (1994). Bathymetric prediction from dense satellite altimetry and sparse shipboard bathymetry, *Journal of Geophysical Research* **99**.

Smith, W. H. and Sandwell, D. T. (1997). Global sea floor topography from satellite altimetry and ship depth soundings, *Science* **277**: 1956–1962.

Wölfl, A.-C., Snaith, H., Amirebrahimi, S., Devey, C. W., Dorschel, B., Ferrini, V., Huvenne, V. A. I., Jakobsson, M., Jencks, J., Johnston, G., Lamarche, G., Mayer, L., Millar, D., Pedersen, T. H., Picard, K., Reitz, A., Schmitt, T., Visbeck, M., Weatherall, P. and Wigley, R. (2019). Seafloor mapping – the challenge of a truly global ocean bathymetry, *Frontiers in Marine Science* **6**.

# Chapter 1

# Marine vertical gravity gradients reveal the global distribution and tectonic significance of "seesaw" ridge propagation

## 1.1 Introduction

Segmentation of the global mid ocean ridge (MOR) system is one of the most prominent features of the ocean floor, yet many details regarding the tectonic processes that occur at the segment discontinuities remain poorly understood. Transform faults are the most obvious form of ridge discontinuity, exhibiting large lateral offsets ($>$ 30 km) of the ridges (Wilson; 1965); because they are stable in time and space, they produce the pronounced off-axis fracture zones that record the spreading motion of the plates. Along both slow (e.g. Sempéré et al.; 1990) and fast spreading ridges (e.g. MacDonald et al.; 1988) there also exist smaller-scale, and less stable forms of ridge discontinuity. These features became apparent once detailed bathymetric and magnetic surveying of the ridges began (Schouten and White; 1980), after which, the prevalence and wide variety of ridge discontinuities was quickly recognized (Macdonald et al.; 1991), including stable transform faults, propagating ridges (also known as rifts, (Hey et al.; 1986)), overlapping spreading centers (MacDonald et al.; 1988), and even smaller-scale discontinuities (Macdonald et al.; 1991), including deviation in ridge axis linearity, changes in ridge petrology (Langmuir et al.; 1986), and disruptions in the continuity of the magma lens (Kent et al.; 1990).

A thorough review of ridge segmentation can be found in Carbotte et al. (2016).

As these features continued to be discovered, it soon became apparent that the overall morphology of ridges and the style of their segmentation are intrinsically related to the seafloor spreading rate, and hence, the thermal structure and strength of the oceanic plates (e.g. Macdonald; 1982; Macdonald et al.; 1987; Small and Sandwell; 1989; Chen and Morgan; 1990; Morgan and Chen; 1993; Small and Sandwell; 1994; Dunn; 2015). Such variations include, for example, the presence of an axial valley or axial high, changes in the along strike spacing and ridge-to-ridge width of transform faults, and the presence of ridge propagation or microplate development (e.g. Hey et al.; 1995). Several authors (Small and Sandwell; 1994; Chen and Morgan; 1990; Malinverno; 1991) have proposed that a major transition in the style of MOR tectonics occurs over the half spreading rate range of $\sim$25-40 mm yr$^{-1}$. At rates lower than this (i.e., intermediate- to slow-spreading), the ridges are characterized by axial valleys and transform faults and fracture zones have prominent troughs that are typically spaced $\sim$50–80 km apart. Conversely, at higher spreading rates (i.e., fast-spreading) the ridge axis has an axial high, the transform faults are more widely spaced along axis ($\sim$100–1000 km) and the fracture zones have both ridges and troughs with smaller amplitudes.

The process of ridge propagation has been documented at all spreading rates with the exception of ultraslow spreading centers (e.g. Hey et al.; 1986; Morgan and Sandwell; 1994; Korenaga and Hey; 1996; Dannowski et al.; 2011; Zheng et al.; 2019). Ridge propagators were originally characterized by Hey (1977) who observed the off-axis V-shaped pseudofault pairs in marine magnetic anomalies. Figure1.1a shows a schematic for a typical propagating ridge (PR). There is a small transform-like offset in the spreading ridge, which, over time, "migrates" parallel to the ridge leaving behind a pseudofault on the left (P1 in the figure). This "outer" pseudofault represents a small age offset ($\sim$1 Ma) in the seafloor and has a topographic expression that resembles that of a fracture zone. On the right is a broader sheared zone, bounded by the "inner" pseudofault and failed rift, that consists of crust that originally formed on the left plate and was transferred to the right plate. This transfer produces a sheared zone (S1 in the figure) having a

width that is equal to the offset of the transform. The morphology of the sheared zone is wider and more complex than the outer pseudofault and thus one can distinguish between the outer pseudofault and sheared zone in the seafloor morphology.

Along slow- and intermediate-spreading ridges, there exists a unique but poorly documented type of propagating offset. These behave similarly to PRs but produce distinctive W-patterns in the ridge flanks (e.g. Figure1.1c). These features have previously been referred to as "discordant zones" (Grindlay et al.; 1991) and "non-transform discontinuities" (NTDs) (e.g. Rea; 1978; Hey et al.; 1980, 1986; McKenzie; 1986; MacDonald et al.; 1988) but few have been mapped off axis at high resolution using multibeam sonar (e.g. Grindlay et al.; 1991; Cochran and Sempéré; 1997). A recent study by Zheng et al. (2019) examined the long-term evolution of NTDs. They found NTDs show structures typical of rift propagation (inner and outer pseudofaults) and crustal blocks transferred between ridge flanks by discontinuous jumps of the propagating ridge tip. The main difference between NTDs and the propagators found at higher spreading rates is that the rate of propagation is highly variable and the direction of propagation eventually reverses (e.g. Figure 1.1 and Figure 1 of Zheng et al. (2019)). Short reversals in propagation direction have also been observed at PRs at faster spreading ridges and have been dubbed "dueling propagators" (MacDonald et al.; 1988; Macdonald et al.; 1991; Johnson et al.; 1983; Wilson; 1990). Because—as we document in this paper—such features now appear so ubiquitous in the VGG at slow and intermediate spreading regimes, we have adopted the term "seesaw propagators" (SSPs) to describe these NTDs. We refer to off-axis features as "fossil" SSPs and the discontinuities at which they arise as NTDs or "active" SSPs.

In our more global analysis, we follow the recent terminology of (Zheng et al.; 2019) and refer to NTDs within a propagating ridge framework. Their detailed analysis of a region of the Mid-Atlantic Ridge between 24 and 27.5 N uses multibeam bathymetry, marine magnetic anomalies, and satellite-derived gravity to document the traces and age offsets of the NTDs. They find that all the NTDs are consistent with the propagating rift model where propagation usually occurs in discrete steps (i.e., the discontinuous propagation model of Hey et al. (1986)).

They noted several differences between the detailed propagation mechanism of NTDs in slower spreading crust as compared with the model developed at intermediate and fast spreading ridges. First, because the slower spreading rift tips abut relatively cold lithosphere, propagation is restricted to where the crust is relatively thin and the shallower than normal mantle is likely to be weakened by serpentinization from seawater penetration. Second, the slower spreading rift has a 20-30 km wide rift valley that can accommodate lateral jumps in the rift axis. They conclude that that their model of NTDs has all the fundamental features of the standard propagating rift model. Our more global analysis does not usually include such high-resolution data, so we adopt the conclusions of the Zheng et al. (2019) study and assert the off-axis traces of all NTDs reflect a different style of rift propagation.

Some of the features included in our new global catalogue were included in the previous regional/global compilations of Morgan and Sandwell (1994); Briais and Rabinowicz (2002); Matthews et al. (2011), who, in lieu of bathymetry data, used satellite-derived vertical gravity gradient (VGG) maps to identify these features. Since these studies, the amount and quality of satellite altimetry data has increased substantially, thus improving the accuracy and resolution of the global free-air gravity and VGG grids (Sandwell et al.; 2019). The newest gravity grid has a spatial resolution of about 16 km compared to a resolution of 22 km in the grid used by Matthews et al. (2011) (Sandwell et al.; 2019). In this study, we take advantage of these improvements (e.g., Figure 1.2) to analyze SSPs globally. Our study comprises five components:

1. We use the new VGG maps to identify and digitize SSP pairs. Many of these are refined digitizations of features identified by Matthews et al. (2011). Though many were classified broadly as discordant zones, we categorize them as NTD/SSPs, and we also added previously unidentified SSPs. We use 224 features (112 pairs) identified by Matthews et al. (2011), many of which we have modified to fit new VGG maps. We identify an additional 146 features (73 pairs), for a total 370 SSPs (185 pairs), most of which are located in the Atlantic and Indian Ocean basins.

2. We quantify the range of spreading rates where we observe this style of propagation and determine the range of age offsets across the ridge discontinuities as compared with transform faults.

3. We investigate the detailed morphology and isostatic compensation of off-axis SSPs using high-resolution multibeam bathymetric data collected as part of the search for the missing Malaysia Airlines Flight 370 (MH370). This shows these off-axis features are isostatically compensated by locally thinned crust in agreement with Zheng et al. (2019).

4. We demonstrate that traces of SSPs are symmetric about the ridge such that propagation direction reversals can be used as a new data type for detailed plate reconstructions.

5. Finally, we test the validity of models previously proposed to explain the direction of propagation for unidirectional propagators for the case of seesaw propagation.

## 1.2 Data

### 1.2.1 Marine vertical gravity gradient

To identify and digitize SSPs globally, we primarily used the VGG grid version 29. Details regarding the acquisition of these data and derivation of the gridded global map can be found in previous papers (e.g. Sandwell et al.; 2019).

The VGG is $g_z(\mathbf{x}) = \partial g(x)/\partial z$, where $\mathbf{x}$ is the horizontal position vector. The VGG is used to highlight the shorter wavelength variations in the gravity field (e.g. Wessel and Lyons; 1997), that are better suited to mapping relatively fine-scale seafloor tectonic structures. In practice, the VGG is the curvature of the ocean surface as measured by satellite altimetry. The geoid height $N$, which is equal to the height of the ocean surface above the reference ellipsoid, is related to the gravitational potential $U$ by Brun's formula $N = U/g_0$ where $g_0$ is the average acceleration of gravity. The potential satisfies Laplace's equation $\frac{\partial^2 U}{\partial x^2} + \frac{\partial^2 U}{\partial y^2} + \frac{\partial^2 U}{\partial z^2} = 0$ and the vertical gravity gradient is $g_z = -\frac{\partial^2 U}{\partial z^2}$, so $g_z = g_0\left(\frac{\partial^2 N}{\partial x^2} + \frac{\partial^2 N}{\partial y^2}\right)$. Unfortunately, by taking

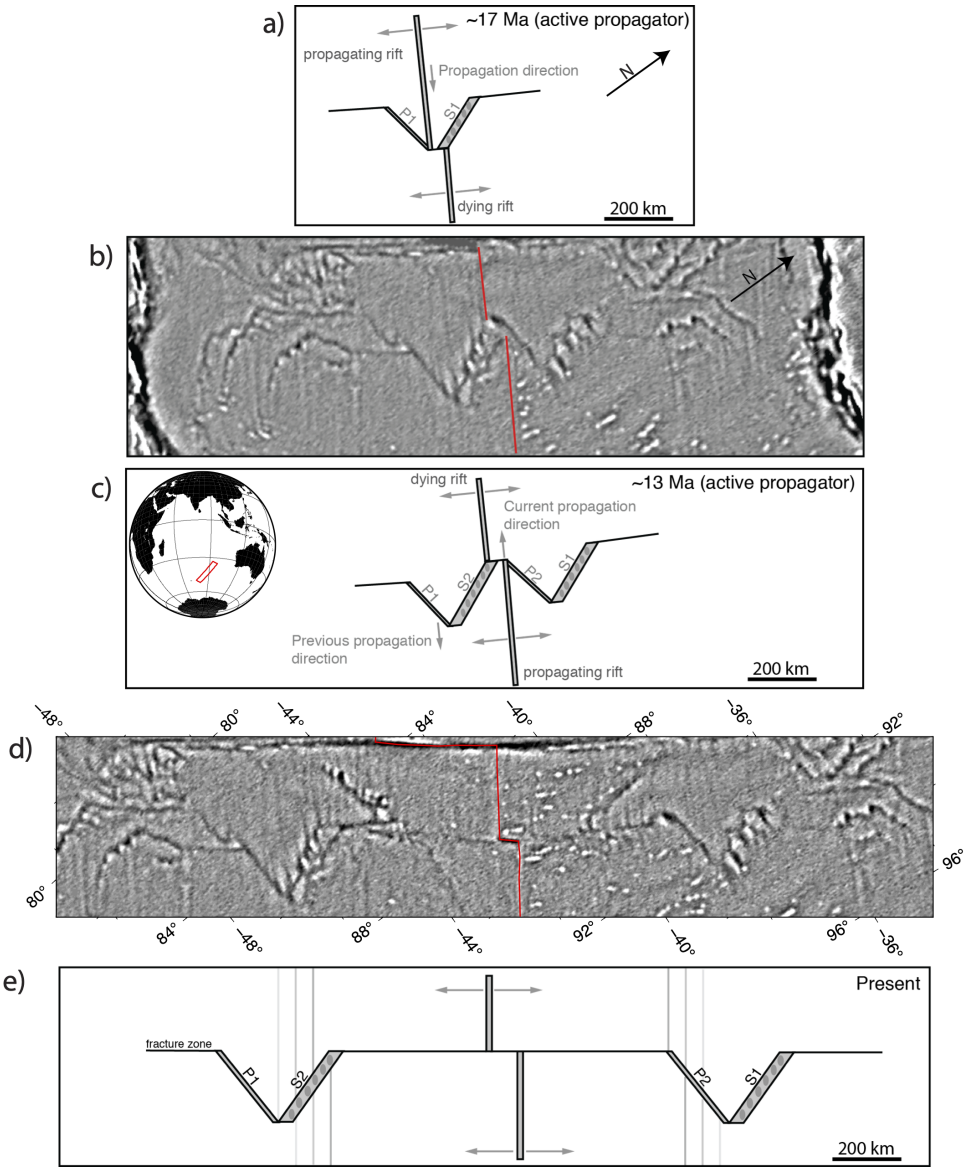


**Figure 1.1.** Evolution of a seesaw propagator in the Southeast Indian Ocean. The vertical gravity gradient (VGG) is rotated so ridges are up-down and transforms are left-right. (a) Reconstruction of VGG at 17 Ma shows the "outer" pseudofault (P1 left) and sheared zone (S1 right) of an ordinary eastward propagating ridge. The outer pseudofault has a straight trough while the sheared zone has a series of rotated blocks (i.e., the discontinuous propagation model of Hey et al. (1986)). (b-c) The direction of propagation reverses resulting in a W-shaped scar in the VGG at 13 Ma. (d-e) The transform offset increases by asymmetric spreading which stops ridge propagation resulting in an ordinary fracture zone with symmetrical V's at the distal ends. A seesaw propagator has one or more reversals in the direction of propagation.

this derivative, the signal of the short wavelength background noise (predominantly from ocean waves) is also amplified. Improvements in the accuracy and spatial resolution of the VGG–owing to the inclusion of a wealth of new data obtained over the past eight years from altimeters CryoSat-2, Jason-1/2, and the first non-repeat Ka-band altimeter, SARAL/AltiKa–have, however, resulted in a significantly lower noise level (e.g. Figure 1.2). This has helped reveal the small-scale tectonic structures including abyssal hills, small seamounts, and now seesaw propagators. SSPs were evident in older VGG maps (e.g. Matthews et al.; 2011), but it is the extra clarity provided by these new data that have revealed their symmetry across the ridges and their similarities with ordinary propagating ridges.

### 1.2.2 Multibeam bathymetry

Multibeam sonar data provide higher-resolution details of SSP morphology compared to the VGG, thus revealing clearer details of their tectonic histories. However, such data are scarce, particularly away from active ridge axes. Previous studies near the ridge axis include those of, for example: Carbotte et al. (1991); Fox et al. (1991); Grindlay et al. (1991), who analyzed discontinuities along the South Mid-Atlantic Ridge (MAR); Sempéré et al. (1993), along the north MAR; Cochran and Sempéré (1997) and West et al. (1999) along the Southeast Indian Ridge; and more recently Dannowski et al. (2018) and Zheng et al. (2019), who analyzed the behavior of non-transform discontinuities (many of which we consider SSPs), along a section of the North MAR.

In this study, we make use of a publicly available multibeam dataset, recently acquired as part of the search for missing Malaysia Airlines Flight 370 (MH370) by the Governments of Australia, Malaysia and the People's Republic of China 2017 (Picard et al.; 2018). This consists of $\sim$279,000 km$^2$ of multibeam bathymetry data concentrated along a $\sim$180 km wide central swath that runs sub-parallel to the Australian plates flowline in the Southeast Indian Ocean (SEIO). A portion of these data are shown in Figure 1.3, where the search path fortuitously mapped two off-axis SSPs, providing the best record of off-axis SSP morphology to date. We

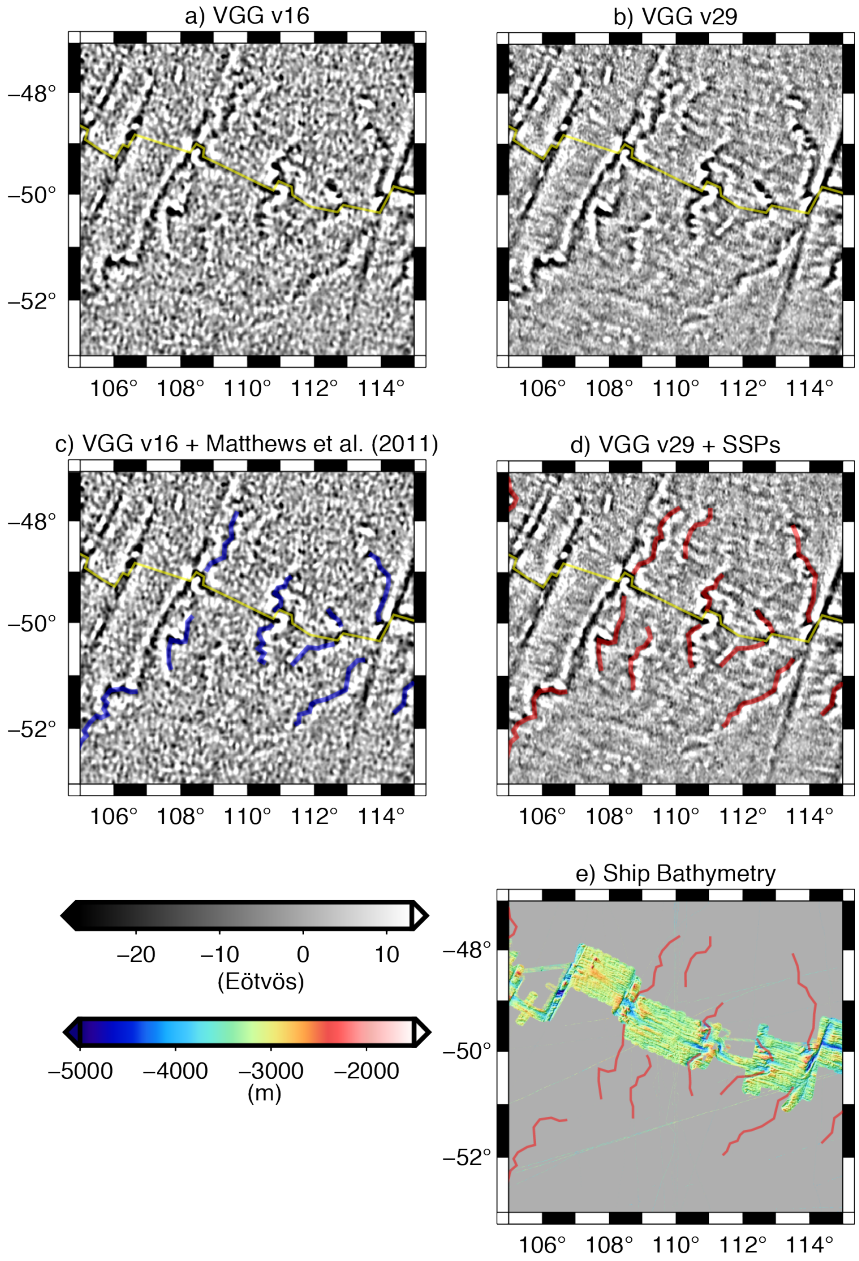


**Figure 1.2.** Comparison between (a) VGG v16 (used by Matthews et al. (2011)) and (b) v29 (used in this study). Note the significantly reduced noise level reveals several previously unidentified SSPs and the extra clarity allows for a more confident identification of the traces of others. The yellow lines trace Southeast Indian Ridge. Features identified in Matthews et al. (2011) (as DZs) are shown in (c). Identified SSPs of this study are shown in (d) as red lines, and available shipboard bathymetry in the region is shown in (e) (Cochran and Sempéré; 1997). Shipboard data shows high resolution morphology of the propagators near the ridge, and satellite data shows a complex history of propagation.

use these data to assess SSP morphology as well as determine the effective elastic thickness of the lithosphere ($T_e$) associated with these features by analyzing them in conjunction with satellite-derived free-air gravity anomalies.

## 1.3 Results and Discussion

### 1.3.1 Identification and digitization of SSPs

SSPs appear as continuous Eötvös lows in the VGG, typically with amplitudes of $\sim$20 Eötvös relative to their surroundings. They trend dominantly in the direction of spreading but with an oblique component that flips polarity ("seesaws") typically on timescales of a few million years (e.g. Figure 1.1). SSPs that are presently "active" can be traced to their associated ridge discontinuities, and like unidirectional propagators, fracture zones and abyssal hills, are approximately symmetric about the ridge axis. The signal of off-axis "fossil" SSPs is similar to those found near the ridges, and in some cases, appears as prominent as fracture zones, even thousands of kilometers from the ridge axis (Figure 1.4).

In order to catalog both active and fossil SSPs globally, we used a variety of data including the satellite derived VGG and free-air gravity anomalies (Sandwell et al.; 2019), multibeam bathymetry (where available) and earthquake locations (Engdahl et al.; 1998). We also re-digitized those MOR segments in close proximity to SSPs (and transform faults) from traces previously published by Sandwell and Smith (2009). Using the VGG grid, our new picks of the ridge axis have inflection points in locations of VGG lows. This required relaxing the ridge/transform orthogonality adhered to in the Sandwell and Smith (2009) study and only transforms which have clear fracture zone extensions were included.

We began our SSP cataloguing by modifying the interpretations of features Matthews et al. (2011) made by analyzing VGG v16. An identical set of digitized features was also included in the supplemental materials of Wessel et al. (2015) as part of the GSFML database. In their analysis, these features were classified as "discordant zones". The "discordant zone" label has

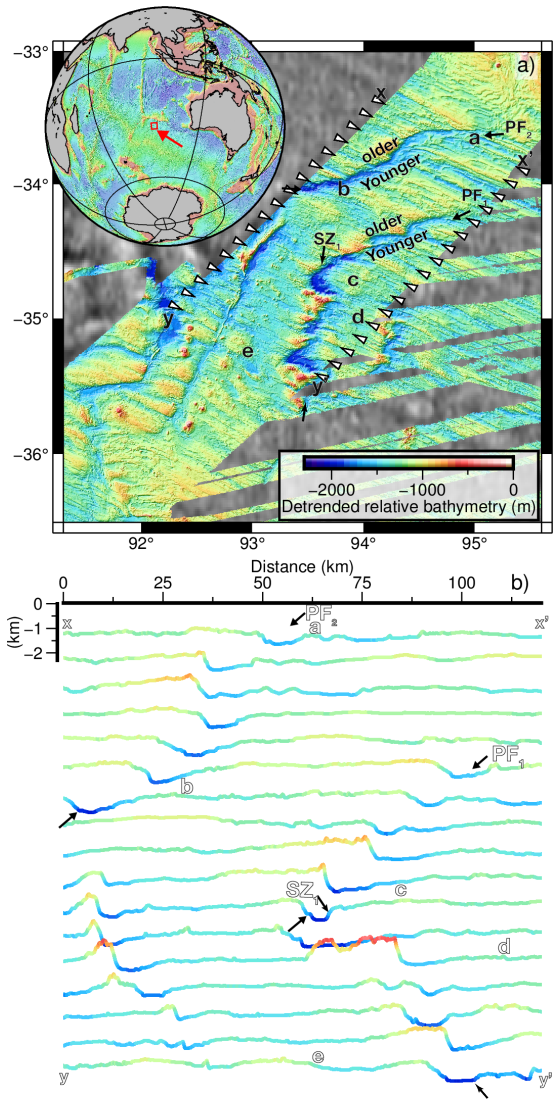


**Figure 1.3.** (a) Multibeam bathymetry over two off-axis SSPs collected in the Southeast Indian Ocean as part of the search for missing flight MH370 (Governments of Australia, Malaysia & the People's Republic of China; 2017). Note, to highlight the morphology of the SSPs with respect to their surroundings, these data have been detrended to remove the regional deepening with age trend and plotted relative to the shallowest depth within the mapped region. Mapping of the northernmost SSP captured only the outer pseudofault (PF2) section, while mapping of the southern SSP reveals both outer pseudofault (PF1) and subsequent sheared zone (SZ1), which formed following a reversal in propagation direction. White triangles indicate the locations of the profiles shown in (b). The inset globe shows the location of (a) (red box). (b) Bathymetric profiles showing the gross morphology of the two outer pseudofaults (PF) and a sheared zone (SZ). The letter labels match the locations shown in (a). Note the SSP bathymetric depressions are $\sim$ 10-15 km wide with amplitudes up to $\sim$ 1 km relative to their flanks.

not seen use in recent literature, and some features identified by Matthews et al. (2011) have been called simply NTDs and interpreted as propagating ridges (e.g. Dannowski et al.; 2018; Zheng et al.; 2019). Because of the complex temporal and spatial propagation patterns these features exhibit, we feel "seesaw propagator" is an appropriate and descriptive term. Since these original picks were made, the improvement in the quality of the VGG data has revealed many more SSP traces and subtle reversals in polarity that were previously unidentifiable (Figure 1.2). We use 224 features (112 pairs) identified by Matthews et al. (2011), many of which we have modified to fit new VGG maps. We identify an additional 146 features (73 pairs), for a total 370 SSPs (185 pairs), most of which are located in the Atlantic and Indian Ocean basins.

Our approach for digitizing SSPs followed two main rules: First, because SSPs create bathymetric valleys (e.g. Figure 1.3), they are always expressed as local Eötvös lows in the VGG, we therefore digitized along the central axes of these lows. Second, both conjugate pairs (i.e., the outer pseudofault and sheared zone) had to be identifiable and symmetric about the spreading axis. For active SSPs, which can be traced from the ridge axis, there is little ambiguity here (e.g. Figure 1.4e-g). However, for fossil SSPs located off-axis, satisfying this criterion can be difficult. This is particularly a problem for features located on old seafloor, where the signal may be suppressed by the accumulation of sediments and the subsidence of the lithosphere and/or overprinted by other bathymetric fabrics (e.g. Figure 1.4a-d). Where these ambiguities prevented the identification of either conjugate feature or where either trace was unclear, we omitted them from our database. Thus, our SSP count and the related statistics may be considered lower bounds. The total length of the digitized SSPs is about 110,000 km; the total length of fracture zones within the same basins is about 340,000 km. Thus, in the slow and intermediate spreading basins, SSPs are about 30% as abundant as fracture zones in the oceanic crust.

### 1.3.2 Spreading rates and age offsets of SSPs

In order to better understand the relationships between the distribution of SSPs and transform faults with respect to seafloor spreading rate and the age offset across a given ridge

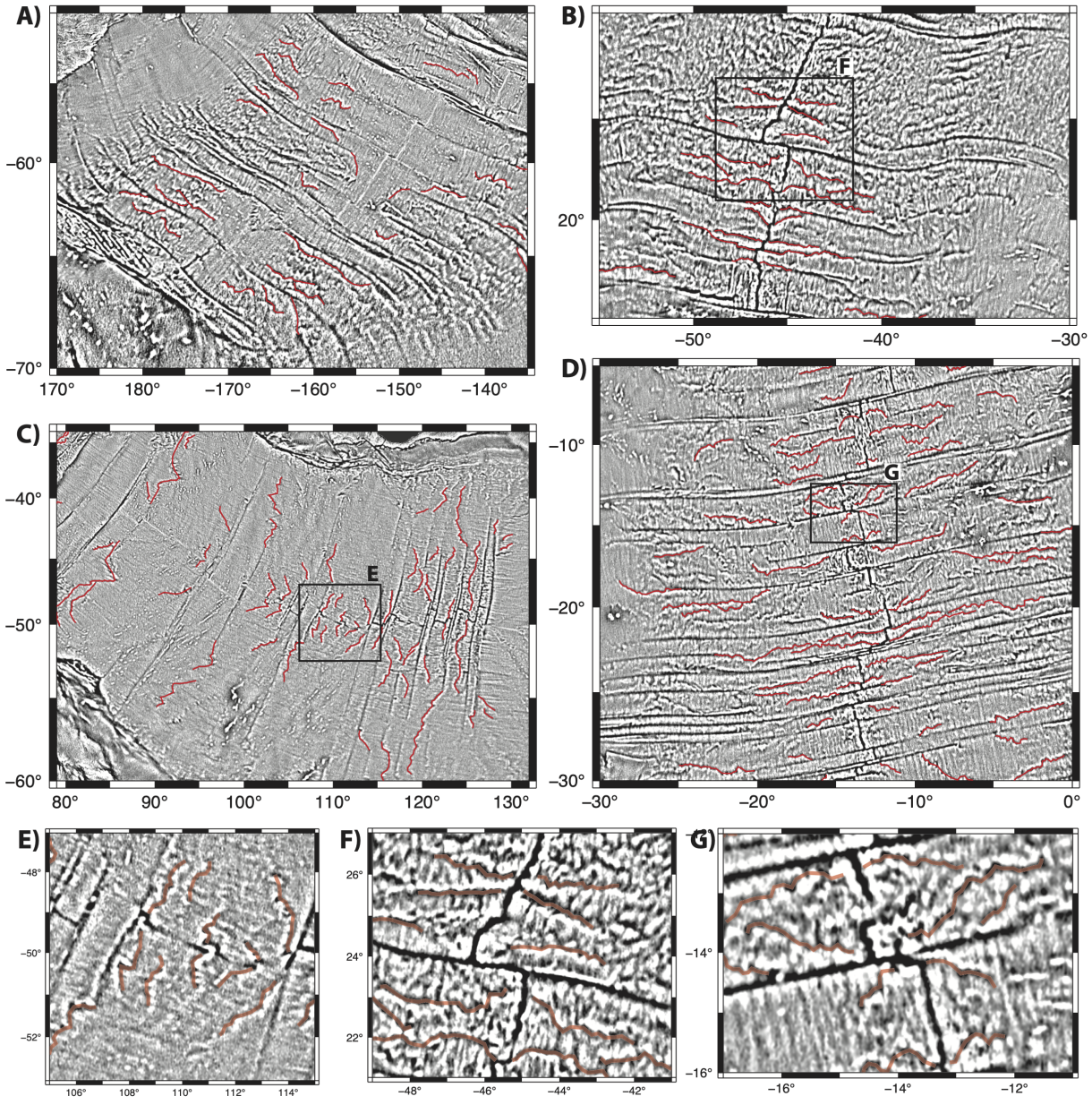


**Figure 1.4.** (upper) SSPs in four different basins: (a) South Pacific, (b) North Atlantic, (c) Southeast Indian, (d) South Atlantic. SSPs form in pairs symmetric about the spreading ridge and can be identified by their symmetry even in old oceanic crust. Virtually all active SSPs occur along axial valley ridge morphologies (VGG lows). (lower) Zoom of three areas along spreading ridges where propagators are presently propagating in both directions within single or nearby segments.

discontinuity, we analyzed our new SSP and transform fault catalogue in conjunction with the global age and spreading rate grids of Müller et al. (2016). To obtain the spreading rate at the time of formation of each SSP, we computed the centroid and length of each digitized SSP polyline segment and sampled the centroid on the global spreading rate grid. This spreading rate distribution with respect to half spreading rate (binned at 2 mm $yr^{-1}$) is shown in Figure 1.5a. The distribution peaks at 22 mm $yr^{-1}$ half-rate and drops to zero at both ultraslow ($<$ 10 mm $yr^{-1}$) ridges and fast ridges ($>$ 40 mm $yr^{-1}$). The upper spreading rate limit is broadly coincident with the transition range in ridge topography from axial valley to axial high. This limit in the distribution doesn't necessarily suggest that SSPs only occur at axial valley-type ridges, but that the relief created in the seafloor at axial valley SSPs is sufficient enough to be visible in the satellite VGG data. Due to upward continuation, bathymetric features with a smaller spatial wavelength ($<$ 12 km) and/or less relief cannot be reliably detected in satellite VGG (Sandwell et al.; 2019). Pseudofaults at fast-spreading ridges are often harder to observe in the bathymetry (e.g. Cormier and Macdonald; 1994; Hey et al.; 1995). Similarly, bathymetric variations created by NTDs at fast spreading ridges are subtle or indistinguishable from the surrounding seafloor, although these have been identified by high-resolution mapping of variations in crustal thickness (Boulahanis et al.; 2020).

To determine the distribution of transform faults and SSPs with respect to age offset, we measured the transform fault and SSP ridge offset lengths and divided by the current half spreading rate. Since active SSPs are primarily found along the Mid Atlantic Ridge (MAR) and the Southeast Indian Ridge (SEIR), we restricted this analysis to these ridges. These two distributions are shown in Figure 1.5b. SSPs have a maximum age offset of about 2.5 Ma, while transform faults usually have age offsets greater than 2 Ma; these results are consistent with other studies of non-transform offsets (MacDonald et al.; 1988; Macdonald et al.; 1991; Grindlay et al.; 1991). Since depth-integrated lithospheric strength increases with the age of the lithosphere, we speculate that seesaw propagation is not possible when the age offset is greater than about 2.5 Ma. This is consistent with the inferences of Grindlay et al. (1991), who suggested that a

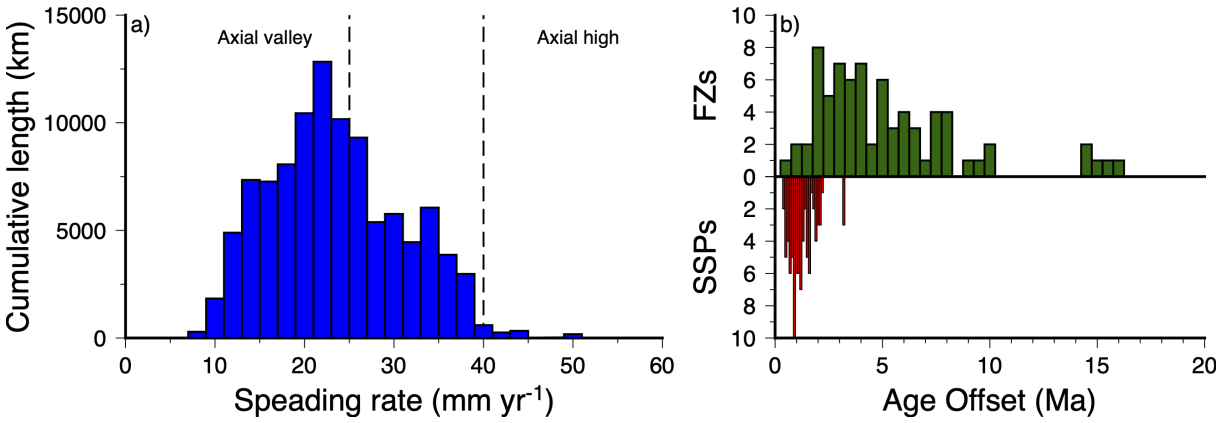


**Figure 1.5.** (a) The distribution of SSPs with respect to half spreading rate. The upper limit of $<$ 25–40 mm yr$^{-1}$ is coincident with the transition from axial valley to axial ridge morphology (when the transition is expressed as a function of spreading rate only) (Small and Sandwell; 1994; Chen and Morgan; 1990; Malinverno; 1991). We see no SSPs at ultraslow ridges ($<$ 10 mm yr$^{-1}$)–in these environments (Southwest Indian ridge or the Arctic), neither the ridge segmentation or the off-axis tectonic fabrics are well developed. (b) Distribution of lithospheric age offset across active discontinuities along the Mid-Atlantic Ridge and Southeast Indian Ridge. SSPs (red) generally have offsets less than 2.5 million years, whereas transform faults (green) usually have larger age offsets.

mechanical transition from non-rigid to rigid deformation occurs in MOR discontinuities when the segment offset length is larger than $\sim$30 km.

### 1.3.3 Morphology and isostatic compensation of SSPs

We investigate the detailed morphology and isostatic compensation of off-axis SSPs using high-resolution multibeam bathymetric data collected as part of the search for the missing Malaysia Airlines Flight 370 (MH370). The detailed bathymetry for one complete "seesaw" propagation cycle of a fossil SSP (PF1 and SZ1), as well as an additional outer pseudofault (PF2) from another SSP is shown in Figure 1.3. The bathymetry has been detrended to remove the effect of the seafloor subsidence with age and reveals that both outer pseudofault valleys are 15–20 km wide and exhibit a deepening of several hundred meters over age. They also exhibit pronounced bathymetric highs on the older sides (in front of the direction of propagation) and broad lows towards the younger side. This high-low morphology is also evident in the sheared zone (SZ1), although the relationship is reversed (i.e. the bathymetric highs occur on the younger

side). Based on this analysis, as well as the recent multibeam analysis by Zheng et al. (2019), we propose that SSPs typically form 1-2 km of relief, similar to oceanic fracture zones that form at the same spreading rate. As the overall length of the SSPs is about 30% of the length of fracture zones, they therefore represent a major component of global seafloor roughness. Rough seafloor can generate substantial internal tides as tidal currents interact with topography, and internal tides contribute to mixing in the deep ocean (Garrett; 2003). How much SSP topography, independent of abyssal hills and fracture zones, affects internal tide generation remains to be studied.

As shown above, the age offsets across SSPs forming today are less than about 2.5 Ma which suggests that all SSPs form on very young lithosphere where the bathymetric troughs of the SSPs is locally compensated by thinner than normal crust (Zheng et al.; 2019). In contrast, transform faults usually have larger age offsets and therefore much of the topography is formed on lithosphere that is somewhat older (2-10 Ma). This difference in age should be evident as a difference in the effective elastic thickness ($T_e$), a proxy for lithosphere strength that usually increases with age as the plate cools. To test this hypothesis, we modelled the free-air gravity anomalies expected from the MH370 bathymetry and its isostatic compensation using a thin elastic plate flexure model. Two areas were selected (i.e., (a) and (b) in Figure 1.6); the SSP area (a) has a seafloor age of 22–35 Ma while the Geelvinck fracture region (b) has a seafloor age of 11–20 Ma. We adopted a forward modelling approach (e.g. Watts et al.; 2006), and compared the modelled gravity with the satellite-derived gravity. The steps below outline our method using GMT (Wessel et al.; 2019) which we applied for a range of constant $T_e$ values between 0–30 km:

1. High-pass filter the bathymetry (SRTM15+V2, Tozer et al. (2019)) and free-air anomalies (Sandwell et al.; 2019) to remove the long wavelength component from the gravity field which is not associated with isostatic compensation of the seafloor features, such as deep mantle dynamics and fully compensated bathymetry (e.g. Watts and Moore; 2017). These filters were applied to spherical harmonic representations of the data using a cut-off wavelength of $\sim$400 km (degree n=100) cosine tapered to $\sim$571 km (degree n=70).

2. For a uniform plate, calculate the Moho topography required to compensate for the bathymetry load given a prescribed $T_e$ value.

3. Calculate the gravity anomaly produced by the bathymetry and its isostatic compensation (i.e., the Moho topography) using the method of Parker (1972), expanding the series to four terms. For these calculations, standard parameter values were used, as outlined in the table inset of Figure 1.6. In order to avoid edge effects, the root-mean-square (RMS) misfit calculations were restricted to multibeam bathymetry coverage within the areas (a) and (b) shown in Figure 1.6, while the calculations were performed for regions extending 300 km beyond these using predicted bathymetry from Tozer et al. (2019).

4. Compute the RMS misfit between the calculated and observed gravity anomalies.

The results are shown in the inset of Figure1.6. For both areas, the RMS misfit versus $T_e$ has a broad minimum reflecting a mixture of tectonic processes in each region. Nevertheless, the best-fit $T_e$ for the SSPs of 3 km is significantly less than the 8 km for the Geelvinck Fracture Zone. We interpret the low $T_e$ value for the SSPs as reflecting the "frozen-in" strength of the lithosphere at the time of formation. That is, these features formed across a narrow discontinuity on very thin and weak lithosphere near the ridge axis. The bathymetric troughs are associated with thin crust and thus shallower than normal mantle in agreement with the analysis of Zheng et al. (2019). In contrast, the value across the Geelvinck Fracture Zone–which separates seafloor with a much larger age contrast ($\sim$ 5 Ma)–reflects the averaged signal of the time-dependent flexural compensation required to maintain this feature (e.g. Sandwell and Schubert; 1982). This involves the flexure of older, and hence stronger lithosphere, which is reflected in the larger $T_e$ value.

### 1.3.4 Symmetry of SSPs and new data type for reconstructions

One of the important characteristics of SSPs is that the symmetric kinks in their off-ridge traces provide a new type of data that can be used to refine detailed plate reconstructions.

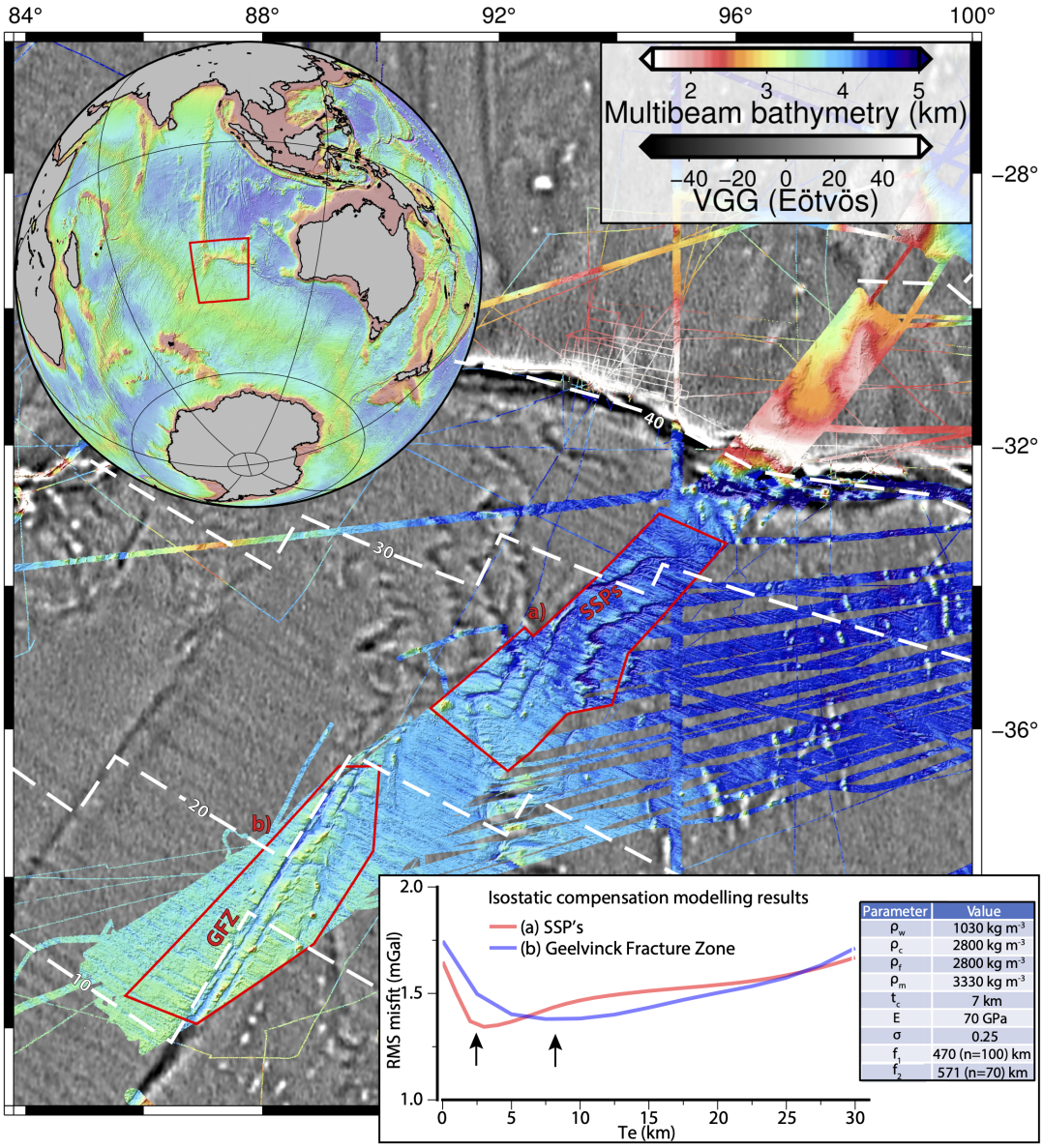


**Figure 1.6.** Multibeam bathymetry acquired during the search for missing flight MH370 (Governments of Australia, Malaysia & the People's Republic of China; 2017) overlain on the regional VGG grid. Red boxes show the areas used for RMS calculations in the isostatic modelling of the SSPs (a) and Geelvinck Fracture Zone (b). Dashed lines = seafloor age contours (Ma) from Müller et al. (2016). The globe Inset shows the location of the main map (red box). The box inset shows RMS misfits for isostatic compensation models calculated using the given $T_e$ values. Values for other physical parameters used for the modelling are listed in the inset table ($\rho_w$ – water density; $\rho_c$ – crustal density; $\rho_f$ – infill density; $\rho_m$ – mantle density; $t_c$ – crustal thickness; $E$ – Young's modulus; $\sigma$ – Poisson's ratio; $f_{1,2}$ – filter parameters). The black arrows indicate the best-fit $T_e$ values for each region (i.e. 3 km for the SSPs and 8 km for the Geelvinck Fracture Zone).

Moreover, it is not just the kinks in the traces, but the overall shape of the traces that should be symmetrical about a spreading ridge (assuming purely symmetric spreading). We tested this hypothesis using four prominent SSP traces along the SEIR. For each pair, we approximated a pole of opening for that age range by fitting a pole to a nearby fracture zone. We measured the deviation of the SSP trace from the small circle of opening, and plotted this deviation against the age of the plate as sampled from the Müller et al. (2016) age map (Figure 1.7). The shapes of the SSP deviations match well in this coordinate system—which verifies that the "excursions" from the small circle path are age-concurrent for each SSP pair. There are, however, some incongruities that are not so easily explained. Additionally, by plotting these data in this coordinate system, we can easily see the approximate rate of propagation along a ridge axis and how abruptly it may change.

### 1.3.5 Assessment of SSP propagation models

Several hypotheses have been proposed to explain unidirectional ridge propagation. Dannowski et al. (2018) recently reviewed these mechanisms, which include: (1) reorientation of the ridge axis in response to large-scale changes in plate motion (e.g. Hey and Wilson; 1982; Lonsdale; 1985); (2) propagation down a regional topography or gravity gradient (e.g. Morgan and Sandwell; 1994) or as a result of asthenospheric flow (West et al.; 1999); and (3) propagation in response to hotspot volcanism (Hey and Vogt; 1977; Hey et al.; 1980; Morgan and Parmentier; 1985). These hypotheses are not exclusive and they are often invoked together. Importantly, each of these processes would produce predictable patterns in SSP behavior that are testable. Figure 1.8 shows SSPs in the South Atlantic and uses this basin as a case study for qualitative testing of these hypotheses. SSPs that intersect the ridge and have a clear propagation direction are marked as arrows above the profile plots (Figures 1.8b-d).

Hypothesis (1) predicts that when there is a change in plate motion, all active ridges should propagate uniformly toward the pole of plate rotation during clockwise changes in spreading direction and, conversely, away from the pole of opening during anticlockwise changes

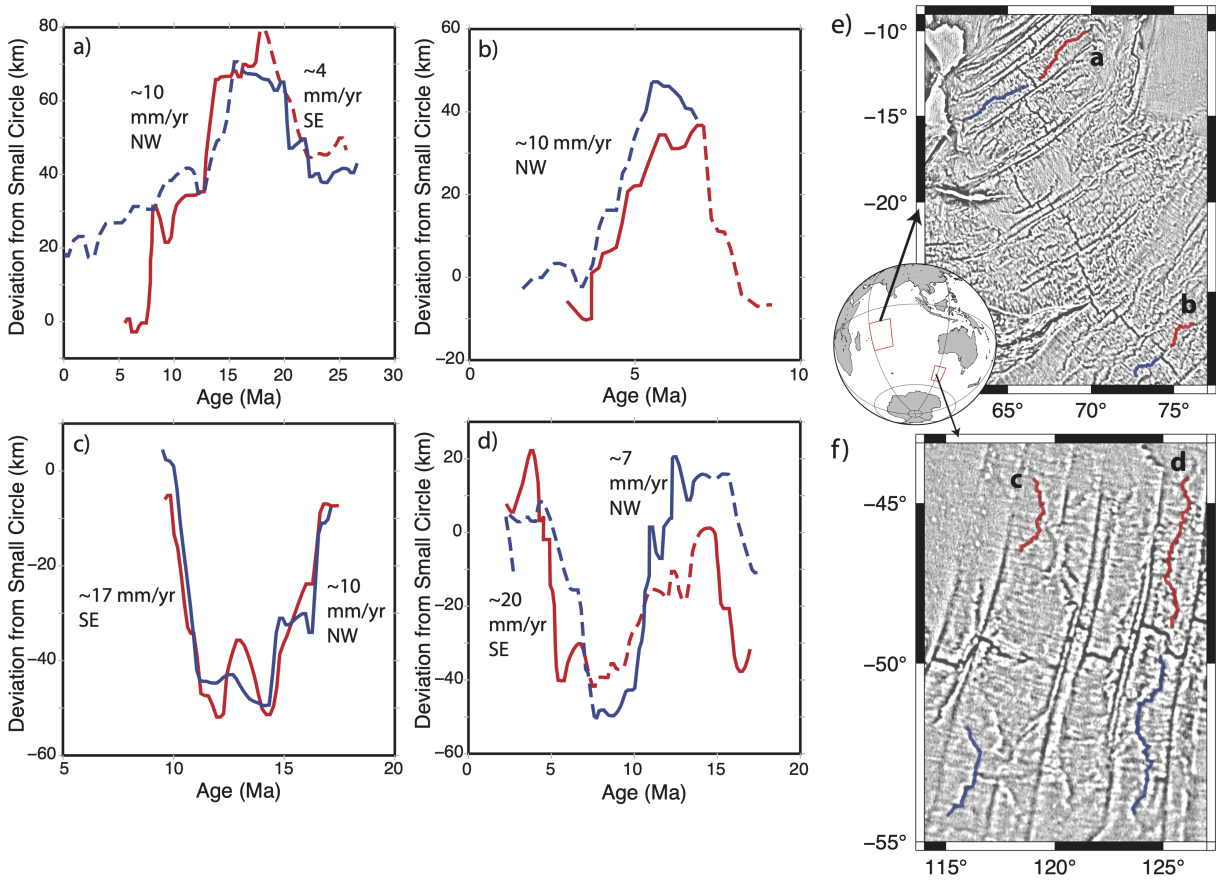


**Figure 1.7.** Four prominent SSP pairs in in the Southeast Indian Ocean and their deviation from the small circle of plate spreading with respect to age (red – Australian Plate, blue – Antarctic Plate (African Plate for a). A solid line indicates the outer pseudofault branch of the segment, and a dashed line indicates the sheared zone (no distinction is made for (c) where neither the sense of offset nor morphology is clear). Location maps for the SSPs are shown in (e-f). The match of the deviations across the ridge reveals their symmetry. Mismatches may be due to asymmetric spreading, small errors in the age grid, and/or errors in identifying the center of the relatively wide sheared zones.

(Lonsdale; 1985), such that, the direction of propagation would be the same for all SSPs along a given isochron since the pole change is a simple function of age. Clearly this does not explain the observed distribution of active SSPs along the MAR, which show many reversals in propagation direction along the ridge. Additionally, we have estimated ages at SSP "inflection points" where the direction of propagation changes and found no clustering of these changes around plate reorganization events (e.g. Lonsdale; 1985) and instead see a more random distribution of changes through time (Figure 1.8f).

Hypothesis (2) predicts that all the propagators move down a regional topography or gravity gradient. To test this hypothesis, we low-pass filtered both the gravity and the bathymetry with 0.5 gain at 160 km wavelength as shown in Figure 1.8a,c. The filtered gravity and bathymetry at the ridge axis are shown as red curves in Figure 1.8b,d. The propagators are marked as black dots and the arrows show the direction of propagation. There is no clear correlation between currently active SSPs and the regional bathymetric and gravity gradients. Moreover, there are numerous examples of active propagation in the up-gradient direction, suggesting this process is not the primary driver of this style of ridge propagation. Propagation driven by asthenospheric flow, such as in West et al. (1999), has a similar pattern of regionally coherent propagation, which is not observed.

Hypothesis (3) predicts that the propagators move away from the upwelling hotspots. Three South Atlantic hotspots are marked as black dots in Figure 1.8a,c. Although it is difficult to rule out an influence of hotspot activity on propagation entirely, it can be seen from the widespread distribution of SSPs relative to the scarce existence of hotspots, that forces generated by these features are also unlikely to be primary drivers in most cases.

We conclude that the processes proposed to explain unidirectional ridge propagation are, alone, not capable of accounting for the seesaw behavior of SSPs. It therefore appears that a driving mechanism operating on a local scale is more likely. We speculate that SSP propagation may occur as a response to a dynamic magma delivery system, in which, complex upward transport of material from a magma source (e.g. Sempéré et al.; 1993; Michael et al.;

1994; Gente et al.; 1995; Tucholke et al.; 1997; Martinez and Hey; 2017; Dannowski et al.; 2018) causes ridge propagation away from the magma foci. Figure 1.8a shows that several, but not all, active SSPs near the ridge axis are propagating away from local positive anomalies, which we interpret as representing present day local magma upwellings. Depending on the time scales of such local magma "pulses," they may be capable of producing the propagation patterns we observe. Moreover, local curvature of the spreading ridge topography may reflect these processes. At slow-spreading axial valleys, we see high curvature in general. However, this remains purely conceptual, and we cannot, at this time, comment on the true nature of sub-axial magma chambers. Ultimately, testing this hypothesis must involve dedicated 3D imaging of a slow-spreading axial magma system beneath a system of active SSPs.

## 1.4 Conclusions

In this study we have documented the global distribution of seesaw propagators, analyzed their distribution and nature with respect to tectonic setting and tested mechanisms to explain their formation and behavior. We draw the following conclusions:

- Seesaw ridge propagation is a ubiquitous phenomenon that occurs at slow and intermediate spreading ridges (i.e., half spreading rates between 10-40 mm $yr^{-1}$). The total length of the identified seesaw propagators is about 30% of the total length of fracture zones within the slow and intermediate spreading basins.

- SSPs form almost exclusively at discontinuities with lithospheric age contrasts less than $\sim$2.5 Ma. This likely reflects a rheological threshold, whereby only young and weak lithosphere allows for "non-rigid" SSP behavior (Grindlay et al.; 1991).

- Seesaw propagation results in W-shaped bathymetric valleys $\sim$10–20 km wide and $\sim$1-2 km deep with respect to the surrounding seafloor. These valleys are asymmetric with steep slopes on the older side of outer pseudofaults and broad shallower slopes towards the younger side. This morphology is mirrored for the sheared zones.

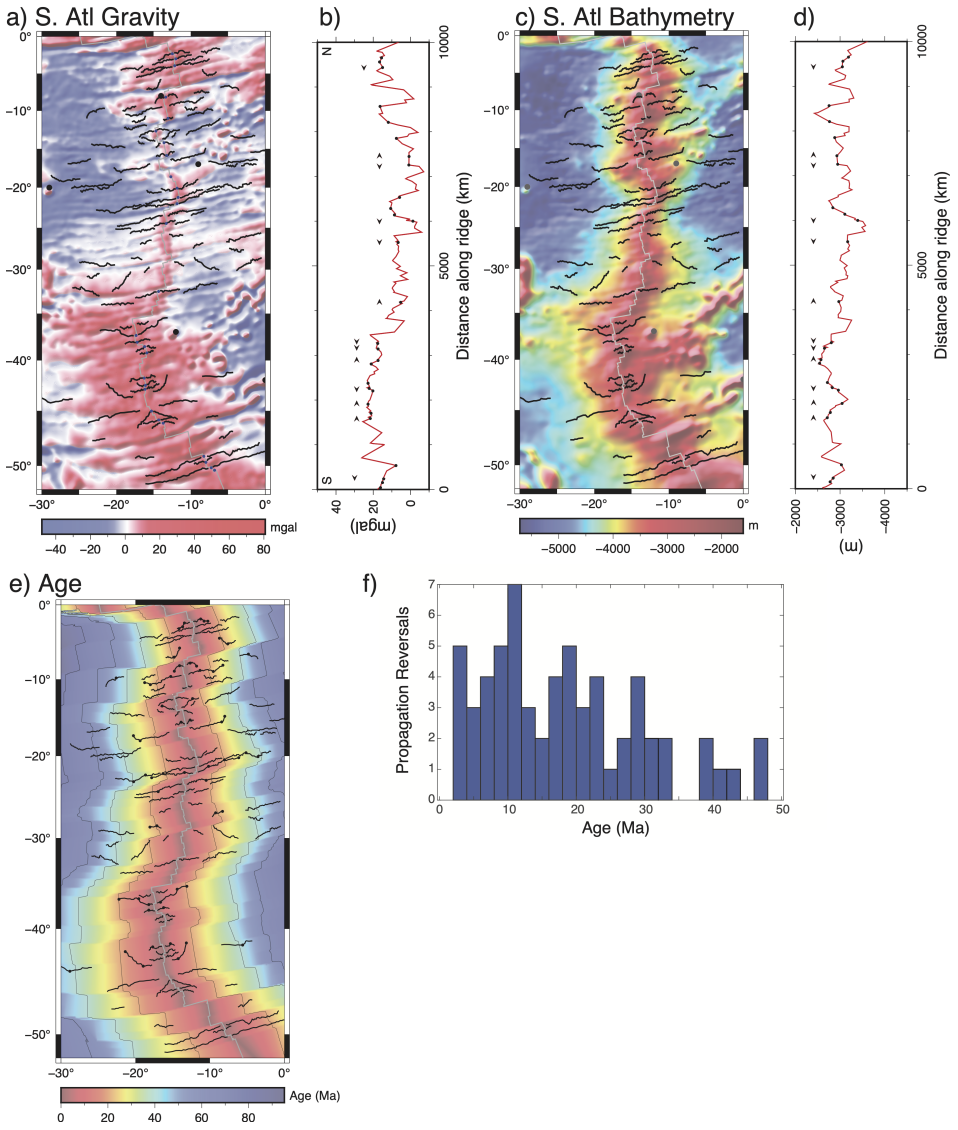


**Figure 1.8.** (a) Low-pass filtered gravity anomaly with present-day ridge axis (gray) and digitized SSPs (black). (b) The depth versus distance along ridge shows regional gravity gradients, and the propagation direction at intersection points of SSPs and the ridge are shown by small arrows. (c-d) Same as (a-b) except for low-pass filtered bathymetry (Tozer et al.; 2019). (e) The Müller et al. (2016) age grid and interpreted SSPs. Within this region, we selected points on SSPs that indicated changes in propagation direction or major change in rate and sampled these points on the age grid. (f) Shows the distribution of these changes through time. There isn't an obvious clustering of the propagation changes with time, but there is a noticeable decrease—this is due to our conservative selection of SSPs and the propagation changes which aren't as clear in older crust.

- The elastic thickness of two fossil SSPs was found to be very low ($\sim$3 km) confirming they formed on hot, young lithosphere near the ridge axis.

- Because SSPs are symmetric about ridge axes, the inflection points (where they reverse direction) of fossil SSPs can be used to improve the accuracy of plate reconstructions as these points must meet at the ridge axis when reconstructed to the time of formation of the given SSP pairs.

- Processes previously proposed to explain unidirectional ridge propagation appear unable to account for SSP behavior. We therefore speculate that local spatial and temporal variations in magma supply may provide the driving forces required to produce SSPs (e.g. Zheng et al.; 2019).

## 1.5 Acknowledgements

We thank ESA, NASA, ISRO and CNES for the open policy and access to the raw waveform data on all the altimeter datasets. We extend our thanks to the reviewers who helped us improve the focus and presentation of this work. This work was supported by the NASA SWOT program (NNX16AH64G) and the Office of Naval Research (N00014-17-1-2866). The Generic Mapping Tools (Wessel et al.; 2019) were used extensively in data analysis and to generate figures. The latest vertical gravity gradient products can be found at ftp://topex.ucsd.edu/pub/global_grav_1min/, and the SRTM15+V2 bathymetry (Tozer et al.; 2019) can be found at ftp://topex.ucsd.edu/pub/srtm15_plus/. Cryosat-2 waveform data can be found at https://science-pds.cryosat.esa.int/. Jason-1/2 and SARAL/AltiKa waveform data can be found at https://www.aviso.altimetry.fr/en/data/products/sea-surface-height-products/global/waveforms.html. MH370 search bathymetry can be found at https://portal.ga.gov.au/persona/marine.

This chapter, in full, is a reprint of the material as it appears in the Journal of Geophysical Research Solid Earth: Harper, H., Tozer, B., Sandwell, D. T., Hey, R. N. “Marine vertical gravity gradients reveal the global distribution and tectonic significance of ”seesaw” ridge propagation”,

*JGR: Solid Earth*, 2021. The dissertation author was the primary investigator and author of this paper.

# References


Boulahanis, B., Carbotte, S. M., Huybers, P. J., Nedimović, M. R., Aghaei, O., Canales, J. P. and Langmuir, C. H. (2020). Do sea level variations influence mid-ocean ridge magma supply? a test using crustal thickness and bathymetry data from the east pacific rise, *Earth and Planetary Science Letters* **535**.

Briais, A. and Rabinowicz, M. (2002). Temporal variations of the segmentation of slow to intermediate spreading mid-ocean ridges 1. synoptic observations based on satellite altimetry data, *Journal of Geophysical Research* **107**.

Carbotte, S. M., Smith, D. K., Cannat, M. and Klein, E. M. (2016). Tectonic and magmatic segmentation of the global ocean ridge system: A synthesis of observations, *Geological Society Special Publication* **420**: 249–295.

Carbotte, S., Welch, S. M. and MacDonald, K. C. (1991). Spreading rates, rift propagation, and fracture zone offset histories during the past 5 my on the mid-atlantic ridge; 25deg-27deg30' s and 31deg-34deg30' s, *Marine Geophysical Researches* **13**: 51–80. A key paper, part of the 1984-1987 MAR cruises.

Chen, Y. J. and Morgan, W. J. (1990). Rift valley/no rift valley transition at mid-ocean ridges, *Journal of Geophysical Research* **95**: 17571–17581.

Cochran, J. R. and Sempéré, J. C. (1997). The southeast indian ridge between 88e and 118e: gravity anomalies and crustal accretion at intermediate spreading rates, *Journal of Geophysical Research* **102**.

Cormier, M. H. and Macdonald, K. C. (1994). East pacific rise 18deg-19degs: asymmetric spreading and ridge reorientation by ultrafast migration of axial discontinuities, *Journal of Geophysical Research* **99**: 543–564.

Dannowski, A., Grevemeyer, I., Morgan, J. P., Ranero, C. R., Maia, M. and Klein, G. (2011). Crustal structure of the propagating tammar ridge segment on the mid-atlantic ridge, 21.5degn, *Geochemistry, Geophysics, Geosystems* **12**: 1–18.

Dannowski, A., Morgan, J., Grevemeyer, I. and Ranero, C. (2018). Enhanced mantle upwelling/melting caused segment propagation, oceanic core complex die off, and the death of a transform fault: the mid-atlantic ridge at 21.5n, *Journal of Geophysical Research: Solid Earth* **123**.

Dunn, R. A. (2015). *Crust and Lithospheric Structure - Seismic Structure of Mid-Ocean Ridges*, Vol. 1, Elsevier B.V.

Engdahl, E. R., van der Hilst, R. and Buland, R. (1998). Global teleseismic earthquake relocation with improved travel times and procedures for depth determination, *Bulletin of the Seismological Society of America* **88**: 722–743.

Fox, P. J., Grindlay, N. R. and MacDonald, K. C. (1991). The mid-atlantic ridge (31degs-34deg30's): Temporal and spatial variations of accretionary processes, *Marine Geophysical Researches* **13**: 1–20. Where are the maps for this? Those could be helpful.

Garrett, C. (2003). Internal tides and ocean mixing, *Science* **301**: 1858–1859.

Gente, P., Pockalny, R. A., Durand, C., Deplus, C., Maia, M., Ceuleneer, G., Mével, C., Cannat, M. and Laverne, C. (1995). Characteristics and evolution of the segmentation of the mid-atlantic ridge between 20degn and 24degn during the last 10 million years, *Earth and Planetary Science Letters* **129**: 55–71.

Governments of Australia, Malaysia & the People's Republic of China (2017). MH370 Search Phase 1 Raw and Processed datasets.

Grindlay, N. R., Fox, P. J. and MacDonald, K. C. (1991). Second-order ridge axis discontinuities in the south atlantic: Morphology, structure, and evolution, *Marine Geophysical Researches* **13**: 21–49. Probably the key paper to cite.

Hey, R. (1977). A new class of "pseudofaults" and their bearing on plate tectonics: A propagating rift model, *Earth and Planetary Science Letters* **37**: 321–325.

Hey, R., Duennbier, F. K. and Morgan, W. J. (1980). Propagating rifts on midocean ridges, *Journal of Geophysical Research* **85**: 3647–3658.

Hey, R. N., Johnson, P. D., Martinez, F., Korenaga, J., Somers, M. L., Huggett, Q. J., LeBas, T. P., Rusby, R. I. and Naar, D. F. (1995). Plate boundary reorganization at a large-offset, rapidly propagating rift, *Nature* **378**.

Hey, R. N., Kleinrock, M. C., Miller, S., Atwater, T. and Searle, R. (1986). Sea beam / deep-tow investigation of an active oceanic propagating rift system, galapagos 95.5w, *Journal of Geophysical Research* **91**: 3369–3393.

Hey, R. N. and Wilson, D. S. (1982). Propagating rift explanation for the tectonic evolution of the northeast pacific-the pseudomovie, *Earth and Planetary Science Letters* **58**: 167–184.

Hey, R. and Vogt, P. (1977). Spreading center jumps and sub-axial asthenosphere flow near the galapagos hotspot, *Tectonophysics* **37**: 41–52.

Johnson, H. P., Karsten, J. L., Delaney, J. R., Davis, E. E., Currie, R. G. and Chase, R. L. (1983). A detailed study of the cobb offset of the juan de fuca ridge: evolution of a propagating rift,

*Journal of Geophysical Research* **88**: 2297–2315.

Kent, G. M., Harding, A. J. and Orcutt, J. A. (1990). Evidence for a smaller magma chamber beneath the east pacific rise at 9deg30' n, *Nature* **344**: 650–653.

Korenaga, J. and Hey, R. N. (1996). Recent dueling propagation history at the fastest spreading center, the east pacific rise, 26deg-32degs, *Journal of Geophysical Research B: Solid Earth* **101**: 18023–18041.

Langmuir, C. H., Bender, J. F. and Batiza, R. (1986). Petrological and tectonic segmentation of the east pacific rise, 5deg30'-14deg30' n, *Nature* **322**: 422–429.

Lonsdale, P. (1985). Nontransform offsets of the pacific-cocos plate boundary and their traces on the rise flank, *Bulletin of the Geological Society of America* **96**: 313–327.

Macdonald, K. C. (1982). Mid-ocean ridges: fine scale tectonic, volcanic and hydrothermal processes within the plate boundary zone., *Annual Review of Earth and Planetary Sciences* **10**: 155–190.

MacDonald, K. C., Fox, P. J., Perram, L., Eisen, M., Haymon, R., Miller, S., Carbotte, S., Cormier, M.-H. and Shor, A. (1988). A new view of the mid-ocean ridge from the behaviour of ridge-axis discontinuities, *Nature* **335**.

Macdonald, K. C., Scheirer, D. S. and Carbotte, S. M. (1991). Mid-ocean ridges: Discontinuities, segments and giant cracks, *Science* **253**: 986–994.

Macdonald, K. C., Sempere, J. C., Fox, P. J. and Tyce, R. (1987). Tectonic evolution of ridge-axis discontinuities by the meeting, linking, or self-decapitation of neighboring ridge segments, *Geology* **15**: 993–997.

Malinverno, A. (1991). Inverse square-root dependence of mid-ocean-ridge flank roughness on spreading rate, *Nature* **352**: 58–60.

Martinez, F. and Hey, R. (2017). Propagating buoyant mantle upwelling on the reykjanes ridge, *Earth and Planetary Science Letters* **457**: 10–22.

Matthews, K. J., Muller, R. D., Wessel, P. and Whittaker, J. M. (2011). The tectonic fabric of the ocean basins, *Journal of Geophysical Research: Solid Earth* **116**: 1–28.

McKenzie, D. (1986). The geometry of propagating rifts, *Earth and Planetary Science Letters* **77**: 176–186.

Michael, P. J., Forsyth, D. W., Blackman, D. K., Fox, P. J., Hanan, B. B., Harding, A. J., Macdonald, K. C., Neumann, G. A., Orcutt, J. A., Tolstoy, M. and Weiland, C. M. (1994).

Mantle control of a dynamically evolving spreading center: Mid-atlantic ridge 31-34degs, *Earth and Planetary Science Letters* **121**: 451–468.

Morgan, J. P. and Chen, Y. J. (1993). The genesis of oceanic crust: magma injection, hydrothermal circulation, and crustal flow, *Journal of Geophysical Research* **98**: 6283–6297.

Morgan, J. P. and Parmentier, E. (1985). Causes and rate limiting mechanisms of ridge propagation: A fracture mechanics model, *Journal of Geophysical Research* **90**: 8603–8612.

Morgan, J. P. and Sandwell, D. T. (1994). Systematics of ridge propagation south of 30 degrees s, *Earth and Planetary Science Letters* **121**.

Müller, R. D., Seton, M., Zahirovic, S., Williams, S. E., Matthews, K. J., Wright, N. M., Shephard, G. E., Maloney, K. T., Barnett-Moore, N., Hosseinpour, M., Bower, D. J. and Cannon, J. (2016). Ocean basin evolution and global-scale plate reorganization events since pangea breakup, *Annual Review of Earth and Planetary Sciences* **44**: 107–138.

Parker, R. L. (1972). The rapid calculation of potential anomalies, *Geophysical Journal of the Royal Astronomical Society* **31**: 447–455.

Picard, K., Brooke, B. P., Harris, P. T., Siwabessy, P. J., Coffin, M. F., Tran, M., Spinoccia, M., Weales, J., Macmillan-Lawler, M. and Sullivan, J. (2018). Malaysia airlines flight mh370 search data reveal geomorphology and seafloor processes in the remote southeast indian ocean, *Marine Geology* **395**: 301–319.

Rea, D. K. (1978). Asymmetric sea-floor spreading and a nontransform axis offset: The east pacific rise 20degs survey area, *Bulletin of the Geological Society of America* **89**: 836–844.

Sandwell, D. and Schubert, G. (1982). Lithospheric flexure at fracture zones, *Journal of Geophysical Research* **87**: 4657–4667.

Sandwell, D. T., Harper, H., Tozer, B. and Smith, W. H. (2019). Gravity field recovery from geodetic altimeter missions, *Advances in Space Research* .

Sandwell, D. T. and Smith, W. H. (2009). Global marine gravity from retracked geosat and ers-1 altimetry: Ridge segmentation versus spreading rate, *Journal of Geophysical Research: Solid Earth* **114**: 1–18.

Schouten, H. and White, R. S. (1980). Zero-offset fracture zones, *Geology* **8**: 175–179.

Sempéré, J. C., Lin, J., Brown, H. S., Schouten, H. and Purdy, G. M. (1993). Segmentation and morphotectonic variations along a slow-spreading center: The mid-atlantic ridge (24deg00' n-30deg40' n), *Marine Geophysical Researches* **15**: 153–200.

Sempéré, J. C., Purdy, G. M. and Schouten, H. (1990). Segmentation of the mid-atlantic ridge between 24degn and 30deg40' n, *Nature* **344**: 427–431.

Small, C. and Sandwell, D. T. (1989). An abrupt change in ridge axis gravity with spreading rate, *Journal of Geophysical Research* **94**.

Small, C. and Sandwell, D. T. (1994). Imaging mid-ocean ridge transitions with satellite gravity, *Geology* **22**: 123–126.

Tozer, B., Sandwell, D. T., Smith, W. H., Olson, C., Beale, J. R. and Wessel, P. (2019). Global bathymetry and topography at 15 arc sec: Srtm15+, *Earth and Space Science* **6**: 1847–1864.

Tucholke, B. E., Lin, J., Kleinrock, M. C., Tivey, M. A., Reed, T. B., Goff, J. and Jaroslow, G. E. (1997). Segmentation and crustal structure of the western mid-atlantic ridge flank, 25deg25'-27deg10'n and 0-29 m.y., *Journal of Geophysical Research: Solid Earth* **102**: 10203–10223.

Watts, A. B. and Moore, J. D. (2017). Flexural isostasy: Constraints from gravity and topography power spectra, *Journal of Geophysical Research: Solid Earth* **122**: 8417–8430.

Watts, A. B., Sandwell, D. T., Smith, W. H. and Wessel, P. (2006). Global gravity, bathymetry, and the distribution of submarine volcanism through space and time, *Journal of Geophysical Research: Solid Earth* **111**: 1–26.

Wessel, P., Luis, J. F., Uieda, L., Scharroo, R., Wobbe, F., Smith, W. H. F. and Tian, D. (2019). The generic mapping tools version 6, *Geochemistry, Geophysics, Geosystems* **20**: 5556–5564.

Wessel, P. and Lyons, S. (1997). Distribution of large pacific seamounts from geosat/ers-1: Implications for the history of intraplate volcanism, *Journal of Geophysical Research* **102**.

Wessel, P., Matthews, K. J., Muller, R. D., Mazzoni, A., Whittaker, J. M., Myhill, R. and Chandler, M. T. (2015). Semiautomatic fracture zone tracking, *Geochemistry, Geophysics, Geosystems* **16**: 2462–2472.

West, B. P., Lin, J. and Christie, D. M. (1999). Forces driving ridge propagation, *Journal of Geophysical Research: Solid Earth* **104**: 22845–22858.

Wilson, D. S. (1990). Kinematics of overlapping rift propagation with cyclic rift failure, *Earth and Planetary Science Letters* **96**: 384–392.

Wilson, J. T. (1965). Transform faults, oceanic ridges, and magnetic anomalies southwest of vancouver island, *Science* **150**: 482–485.

Zheng, T., Tucholke, B. E. and Lin, J. (2019). Long-term evolution of nontransform discontinuities at the mid-atlantic ridge, 24degn–27deg30'n, *Journal of Geophysical Research: Solid*

*Earth* **124**: 10023–10055.

# Chapter 2

# Ridge propagation and the stability of small mid-ocean ridge offsets

## 2.1 Introduction

The global mid-ocean ridge system comprises a series of spreading segments and spreading segment offsets (transform faults and propagating ridges). Ridges and transform faults commonly trend perpendicular and parallel to the direction of spreading, respectively. Why this configuration of ridges and transform faults is so prevalent is an unanswered question of plate tectonics. Lachenbruch and Thompson (1972) proposed that an orthogonal configuration of ridges and transform faults minimizes the forces that resist plate spreading. An implication of this model is that the force resisting plate motion along a transform fault is much less than the resistive force along the spreading boundary–i.e., transforms are weak. Oldenburg and Brune (1975), in analyzing the wax models of Oldenburg and Brune (1972), also conclude the resistive forces along a transform must be less than the shear strength of the solid material. Observations of patterns in seismicity and oblique faulting at the ends of ridge segments suggest variations from the regional stress field which may be the result of weak transform faults. Studies of seismic moment budget (Boettcher and Jordan; 2004) find a cumulative moment release deficit of 85-90% compared to kinematic models, suggesting weak coupling at oceanic transform faults. Shi et al. (2022) showed that seismic activity of many oceanic transform faults is spatially segmented and that variations in fault zone properties (such as coupling) must vary along strike. Morgan

and Parmentier (1984) estimated the ratio of normal stress along the ridge to shear stress on the transform fault and found a stress ratio of 3-5 was required to explain observed faulting patterns. Behn et al. (2002) investigated the effect of oceanic transform faults on the stress state of the lithosphere and found that low values of mechanical coupling (5%) along transform faults best explains the observed faulting patterns near large transforms, consistent with the results of Morgan and Parmentier (1984).

Transform faults tend to remain stable, or stationary with respect to the plate boundary, for long periods of time. Fracture zones, the off-axis traces of transform faults, provide critical information for plate reconstructions of the ocean basins as they trace the small circles of a pole of rotation. The stable ridge-transform-ridge configuration is common where ridge offsets are large. However, for small segment offsets (less than about 30 km), the observed configurations are not so simple. Instead of a transform fault, the offset may appear as an overlapping spreading center (common at fast-spreading ridges) or the more general non-transform offset (common at slow- and intermediate-spreading ridges) (e.g. Carbotte et al.; 2016). Grindlay et al. (1991) suggested that, for shorter offsets, the ratio of ridge normal stress to offset shear stress is closer to unity and that coupling may be enhanced at short offsets. Grindlay and Fox (1993) found, for 3 of 5 example offsets, a ridge normal to offset shear stress ratio of 1-3 best explains the observed deformation patterns. Shorter offsets may migrate along the strike of a ridge, accompanied by the lengthening and shortening of the adjacent ridges (the propagating and failing ridges, respectively).

Hey (1977) provides a kinematic model for ridge propagation and identifies some key morphological features such as the outer pseudofault and inner pseudofault/sheared zone complex (Figure 2.1a). Ridge propagation rates are generally similar to local half-spreading rates (Morgan and Sandwell; 1994) although there are exceptions to this rule (e.g. Kleinrock et al.; 1997). There are many non-exclusive driving mechanisms invoked to explain ridge propagation such as: regional topographic gradients (e.g, (Morgan and Sandwell; 1994)); changes in direction of plate motion (e.g. Hey et al.; 1980); or changes in magma supply, either hot-spot driven (e.g.

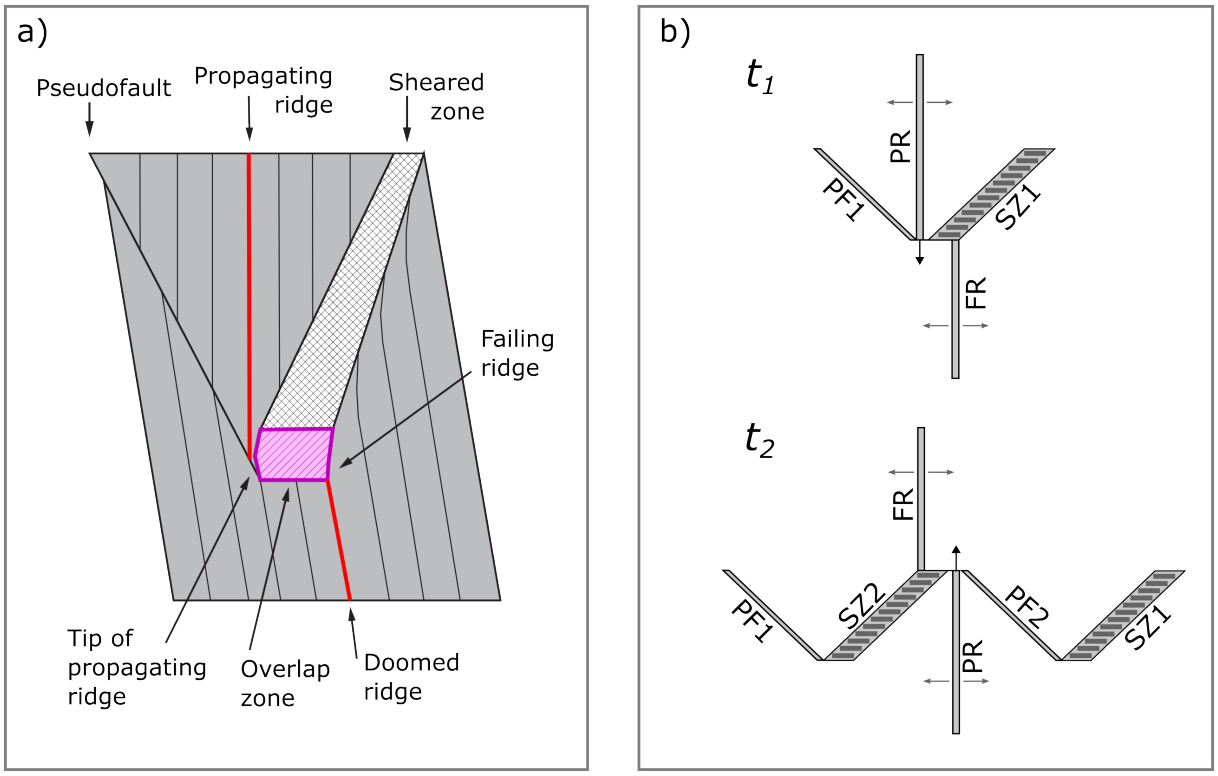


**Figure 2.1.** (a) Plan view schematic diagram of propagating ridge, modified from Hey (2001), all major features labeled. Spreading axes are colored red. The overlap zone, in pink, is a region of active shearing. (b) Schematic diagram of a "seesaw" propagating ridge showing an epoch of propagation (upper) followed by a reversal and second epoch of propagation (lower). PF = pseudofault, SZ = sheared zone, PR = propagating ridge, FR = failing ridge. Both are examples of migrating ridge offsets.

Brozena and White; 1990; Hey et al.; 2010) or segment-scale variations in magmatic inputs (e.g. Dannowski et al.; 2018; Zheng et al.; 2019). Ridge propagation models (and ridge segmentation models more generally) may be classified as either tectonic or magmatic. To explain ridge segmentation and propagation patterns, tectonic models suggest tectonic forces as the cause, whereas magmatic models posit mantle melting patterns as the mechanism.

A propagating ridge may propagate uniformly in one direction, or the direction of propagation may reverse over time (the former propagating ridge becomes the failing ridge, vice versa) (Figure 2.1b). Recently, several studies have documented off-axis scars of propagating ridges in satellite-derived gravity, mostly on seafloor generated at half-spreading rates between 10 and 35 mm/yr (Matthews et al.; 2011; Harper et al.; 2021). The scars show that the direction

of propagation along the ridge often reverses leaving symmetrical “W” patterns in the seafloor. The seesaw patterns are not congruent along nearby seafloor of similar age as could occur if the propagation was driven by minor changes in spreading direction of the two plates. Using satellite-derived gravity measurements, one can examine numerous present-day propagating ridges and the associated ridge offsets (Figure 2.2). From our previous analysis (Harper et al.; 2021), we determine that propagating ridges mostly occur when an offset is less than 30 km (or about 2.5 Myr for the observed range of spreading rates) (Figure 2.2c). For offset distances greater than 30 km, ridge offsets are almost entirely transform faults and do not migrate. The reason for this threshold offset length is not obvious.

Morgan and Parmentier (1985) suggested that ”when a transform fault grows too long, the energy available for propagation will be less than the extra work required to cause transform migration.” The goal of this study is to examine the offset distance threshold that separates transform faults from propagating ridges, which we model as migrating transform fault zones. We define a stable offset to be stationary with respect to a plate boundary, and we hypothesize that the stability of an offset is related its length by the shear stress required to migrate the transform fault (or shear zone) through new lithosphere. We approach this problem with an energy balance model first proposed by Morgan and Parmentier (1985) which we modify to include the energetic effects of a migrating offset. We apply this model to a collection of ridge segments and offsets at slow- to intermediate-spreading ridges to test whether the shear strength of the oceanic lithosphere is a key factor of ridge propagation and offset stability.

## 2.2 Energy balance of stable and unstable ridges

Morgan and Parmentier (1985) proposed an energy balance for propagating ridges where, for a ridge to propagate, the energy available for propagation must be greater than the energy dissipated due to propagation. The energy balance for a stable spreading ridge with no forces driving propagation can be stated:

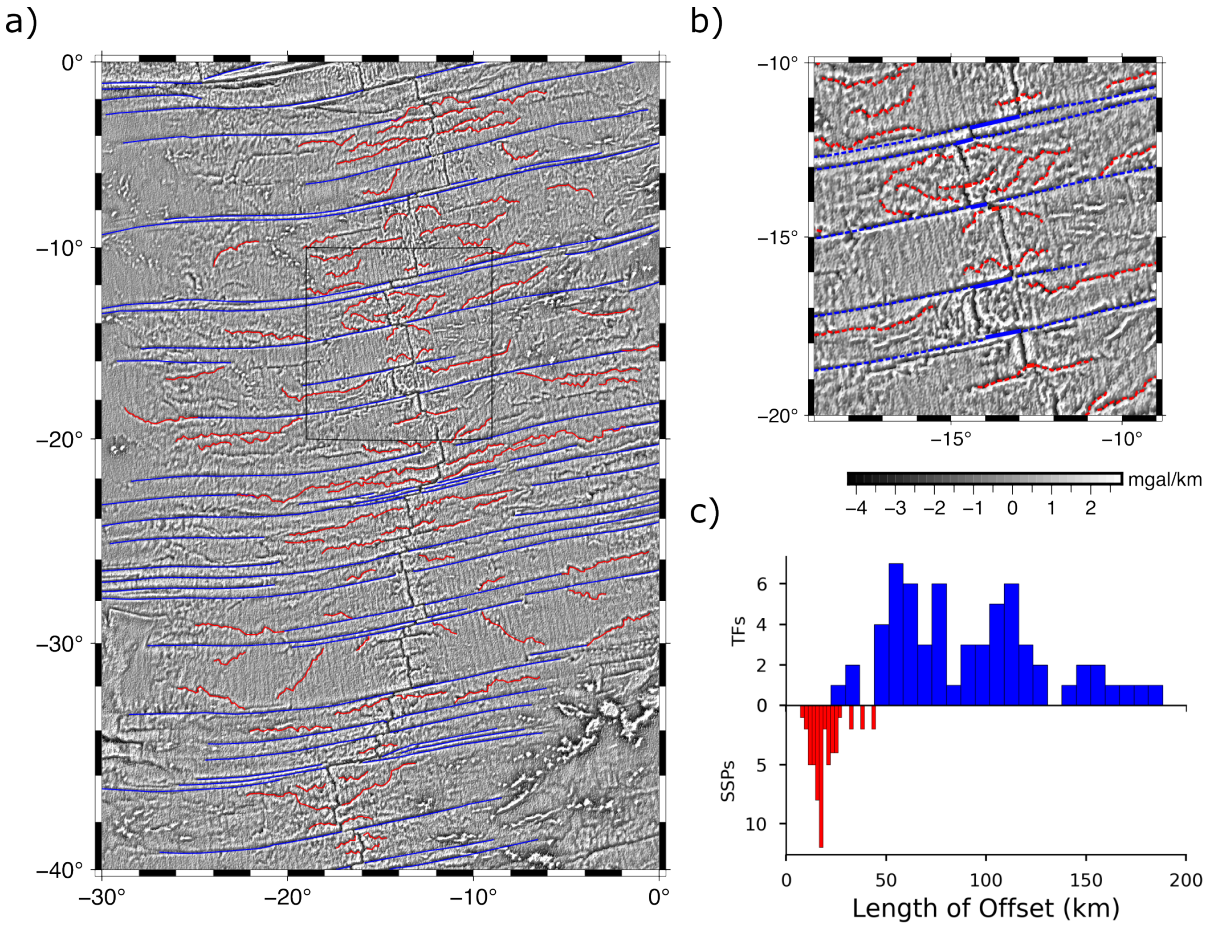


**Figure 2.2.** (a) Vertical gravity gradient (VGG) map of southern Mid-Atlantic Ridge. Fracture zones (created at ridge transform faults) are highlighted in blue. Seesaw propagators (SSPs) presented in Harper et al. (2021) are shown in red. Box shows region in (b). (b) Zoomed-in view of stable and migrating ridge offsets. Where SSPs can be followed to the spreading ridge, we digitize the present ridge offset. SSP ridge offsets are shown in thicker red pen. Transform fault offsets are shown in thicker blue pen. (c) (after Harper et al.; 2021) Measured length of ridge offsets for stable transform faults (upper, blue) and "seesaw" propagators (lower, red).

$$F\,dx = \Phi\,dt\,, \tag{2.1}$$

where $F$ is the force acting on the lithosphere in the spreading direction; $dx$ is the increment of spreading in the time interval $dt$; $\Phi$ is the energy dissipation at the spreading segment from both viscous resisting forces at the spreading center and shear resistance along the transform fault (although the latter term will be small as transform faults are known to be weak). In their model, the spreading ridge is treated as a mode 1 fracture, and an additional force driving propagation of the fracture, $F^*$, is balanced by additional viscous dissipation, $\Phi^*$ and decrease in material strain energy from incremental fracture growth. The force driving propagation is from a gravity spreading stress associated with an anomalously shallow ridge axis.

Here, we use the same basic approach of separating the driving forces into two parts–the force $F$ needed to drive normal ridges and transform faults and an additional force $F^*$ that drives ridge propagation. However, we do not treat the ridge segments as mode 1 fractures. We propose that the forces driving propagation must at least exceed the integrated shear resistance associated with the ridge offset. If we assume equation 2.1 is true and the excess force, $F^*$, may drive propagation, we have:

$$(F + F^*)\,dx = (\Phi + \Phi^*)\,dt \tag{2.2}$$

$$F^*U = \Phi^*\,, \tag{2.3}$$

where $\Phi^*$ is dissipation associated with ridge propagation and $U$ is the half spreading rate ($dx/dt$). We will consider migrating the transform fault or zone the primary mechanism of dissipation. The condition that the driving force must at least exceed the shear resistance is then:

$$F^*U \geq \Phi^*_O\,, \tag{2.4}$$

where $\Phi^*_O$ is the offset shear resistance.

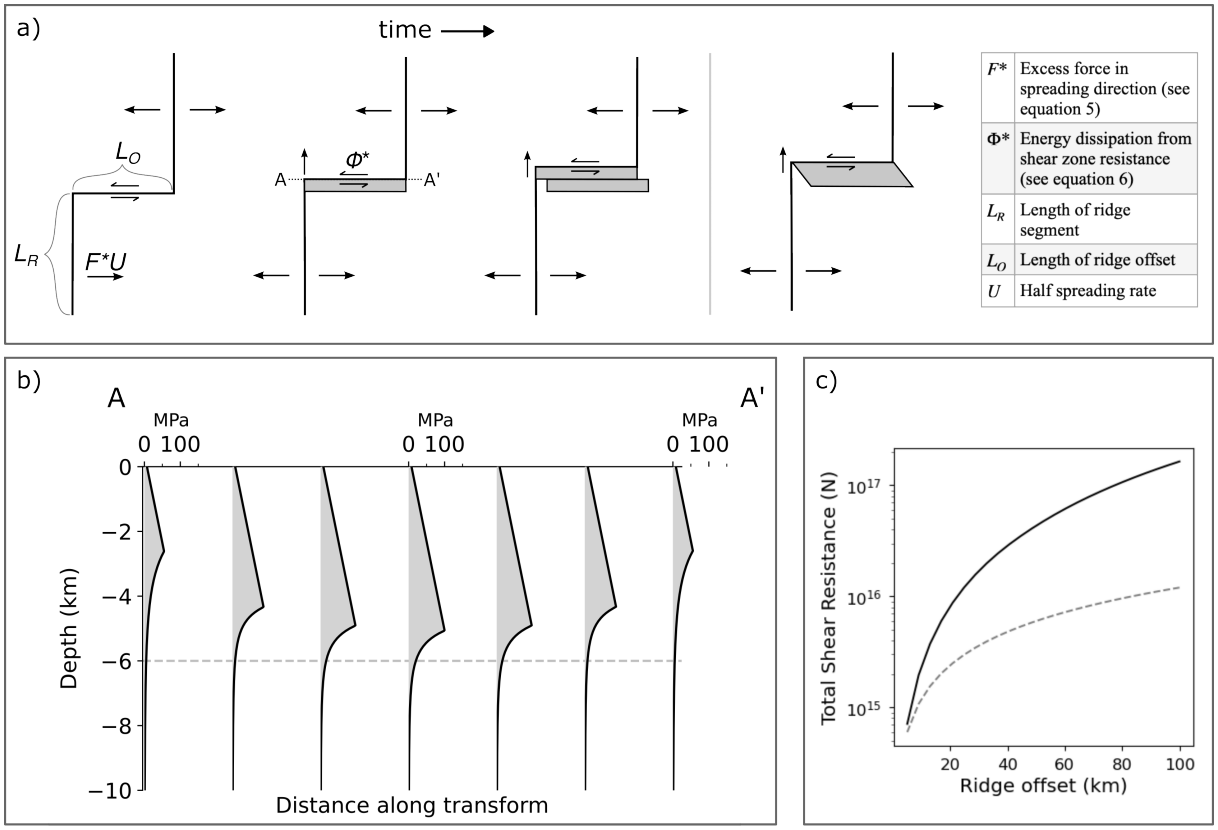


| | |
|---|---|
| $F^*$ | Excess force in spreading direction (see equation 5) |
| $\Phi^*$ | Energy dissipation from shear zone resistance (see equation 6) |
| $L_R$ | Length of ridge segment |
| $L_O$ | Length of ridge offset |
| $U$ | Half spreading rate |

**Figure 2.3.** (a) Kinematics of a migrating ridge offset in plan view–as a ridge propagates, a finite zone is sheared to accommodate transform motion. Continuous shear deformation is shown on the right. Values and limits of integration in equations 2.5 and 2.6 are annotated and listed in the table. (b) Yield strength envelope versus depth using a modified halfspace cooling model for the profile $AA'$. Yield strength is integrated over depth and length of the offset to estimate total shear strength of a 2D offset zone. (c) Total shear strength in offset zone as offset length increases. Solid line is for a yield strength envelope model with coefficient of friction of 0.7. Dotted line is the total resistance using an average shear strength of 10 MPa.

For a ridge segment of length $L_R$, we have the driving force:

$$F^* = \int_{L_R} F_s \, dL, \tag{2.5}$$

where $F_s$ is the excess force per unit length in the direction of spreading.

When a ridge incrementally propagates, new material enters the transform shear zone (Figure 2.3a). Within this zone, the material is stressed beyond its yield strength, so the total resistance of shearing the offset zone is:

$$\Phi_O^* = 2U \int_{L_O} S \, dL. \tag{2.6}$$

$S$ is the vertically-integrated yield strength at a point along the offset and $L_O$ is the length of the offset. Since both sides of equation 2.4 contain the spreading rate $U$, we can compare the forces instead of energy:

$$F^* \geq 2 \int_{L_O} S \, dL. \tag{2.7}$$

We will then refer to the transform resisting force rather than the transform energy dissipation. We emphasize that this yield strength is not the same as the strength of the mature transform fault which is known to be weak.

This model describes the propagation of one ridge segment–the implicit assumption is that the adjacent "failing" ridge has an excess force ($F_{FR}^*$) of zero. For a ridge-offset-ridge system where either segment has an excess force in the spreading direction, both segments contribute to the instability of the offset, so the excess ridge forces will sum ($F^* = F_{PR}^* + F_{FR}^*$). What then determines which segment propagates and which fails or which direction the ridge offset migrates? We posit that a greater total excess force along one ridge should cause a migration of the offset in the direction of the lower excess force ridge ($F_{PR}^* > F_{FR}^*$). An implication of this is that propagation will continue in the same direction unless the state of loading along the ridge segments changes, but these dynamical problems are outside the scope of this study.

We use simple thermal models along with models of the yield strength of the cooling oceanic plate to calculate the transform resistive force from migration of the shear zone ($\Phi_O^*/U$). This force depends on the age offset of the ridges. For example, the lithosphere on either side of a large offset transform is very strong because it is colder, so there is a great resistance that must be overcome.

## 2.3 Methods

### 2.3.1 Yield strength envelope

To assess the strength of the lithosphere and the force required to migrate a ridge offset, we use a brittle failure criterion as defined by Byerlee's law and a ductile flow criterion described by power law flow. Byerlee's law describes the maximum shear stress that rock can support without brittle failure and has the form $\tau_s = S_0 + \mu\sigma_n$ where $\sigma_n$ is the normal stress, $S_0$ is an inherent shear strength, and $\mu$ is the coefficient of friction (Byerlee; 1978). Byerlee's law assumes potential failure on all possible planes, so this stress is a lower bound. Byerlee (1978) found that $\mu = 0.85, S_0 = 0$ at low pressure and $\mu = 0.6, S_0 = 50$ MPa at higher pressures, independent of rock type. We will consider yield strength models with frictional coefficients as low as 0.3. Additional parameter values are given in Appendix A.

The power law flow model describes the maximum differential stress the lithosphere can support without ductile yielding. This value depends on strain rate, temperature (age), and experimentally determined parameters dependent on the composition of the medium (Goetze; 1978; Watts; 2001). We find that varying strain rate does not strongly affect the integrated strength, so we use a constant strain rate of 1e-14 $s^{-1}$. Full flow law details and parameter values are given in Appendix A.

The ductile yield strength depends strongly on temperature of the medium. Near a ridge axis where the crust is hot and newly formed, ductile strength is low and the ductile flow law describes the yield strength. As that material moves away from the ridge and cools, the ductile

strength increases beyond the brittle strength, changing the failure regime (Figure 2.3(b)). There are many different models to describe the cooling of the oceanic lithosphere with age. Two simple 1-D models are the halfspace cooling model and plate cooling model which are basically identical for ages less than 50 Ma.

Simple thermal models don't account for variations in temperature along a spreading axis. They will work well for the middle of a ridge segment, but our areas of concern are ridge tips and discontinuities where there is variability in temperature in the ridge-parallel dimension. Modern ridge thermal models address the problem of ridge offsets (e.g. Behn et al.; 2007; Grevemeyer et al.; 2021), but they can be computationally expensive and, because these studies focus on large transform faults, it's unclear that they apply to shorter offsets. Abercrombie and Ekstrom (2001) approximated transform fault thermal structure by averaging two halfspace thermal profiles on either side of a transform, and Behn et al. (2007) found this model produced thermal profiles similar to their 3-D finite element model. We consider this simple averaging of halfspace cooling models as our preferred cooling model.

Between brittle and ductile yield stress, the lesser value determines the overall yield strength envelope. For a given age or distance along an offset, we integrate the yield strength over the thickness of the lithosphere to estimate the strength as a function of age ($S$ in equation 2.6).

### 2.3.2 Driving forces: estimating $F^*$

We model the driving force as the topographic ridge push force in the direction of spreading. We derive the ridge push force from the stress tensor field. The ridge push force acting from a point $A$ to a point $B$ is related to the difference in pressure at depth at the two points:

$$F_s = \int_{-L}^{0} \Delta P\,(z)\; dz\,, \tag{2.8}$$

where $L$ is the depth of compensation. From conservation of momentum, the horizontal forces at $A$ and $B$ must balance, $F_{HA} = F_{HB}$. If we have:

$$F_{HB} = \int_{-L}^{0} P_B(z)\, dz, \tag{2.9}$$

then:

$$F_{HA} = \int_{-L}^{0} P_A(z) + \tau(z)\, dz \tag{2.10}$$

$$\int_{-L}^{0} \tau(z)\, dz = \int_{-L}^{0} \Delta P(z)\, dz. \tag{2.11}$$

So the ridge push force from $A$ to $B$ is equivalent to the integrated deviatoric normal stress in the direction of $AB$.

We compute the stress field in the crust using the method of Luttrell and Sandwell (2012). Excess topography is treated as a vertical load acting on the crust. We then compute the isostatic balancing force on the Moho, which depends on the elastic thickness of the plate. These loading functions are convolved with the Greens function response for a point load, and the stresses are calculated from the displacement field. We use a Moho depth of 6 km, elastic thickness of 0 km (Airy compensation), and crustal density of 2900 kg m$^{-3}$.

As discussed above, ridge propagation is driven by the excess topography of the spreading ridge with respect to the normal topography needed to drive seafloor spreading. We assume this excess topography is near the ridge. In order to isolate this topography and calculate the excess driving force from a global topography grid we first need to remove large topographic variations related to continents, trenches and other major features that would dominate the stress computation. This was accomplished by masking all continents and oceanic crust older than 70 Myr. The remaining submarine topography is scaled by a factor of $(\rho_c - \rho_w)/\rho_c$ to account for the load of the water column. The topography is then high pass filtered with a cosine taper from spherical harmonic degrees 10 to 20 ($\approx$ 3600 km to 1900 km). The filtering removes the longest wavelength topographic signals such as the overall negative topography of the ocean basins, but

we note that these harmonic degrees are somewhat arbitrary (see discussion).

After determining the stress field due to topography, we determine the normal tractions acting along a vertical surface that coincides with the ridge segment (surface normal $\sim$ parallel to spreading direction). We integrate these tractions along the ridge segment to estimate the loading force $F^*$ (equation 2.5).

### 2.3.3 Digitized ridge segments and offsets

To apply equations 2.5 and 2.6 to real ridge-offset-ridge systems, we approximate the mid-ocean ridge system as a series of spreading segments and lateral offsets. The off-axis SSPs were described and digitized by Harper et al. (2021). For the present day SSPs in that set (i.e., they can be traced continuously to the ridge axis), we digitize the adjacent ridge segments and the offset. All of these features are approximated as simple line segments.

For most of these features, the spreading center has an axial valley morphology and appears as a distinct local low in the VGG. The morphology in the greater offset zone varies in complexity, but offsets are typically associated with slight VGG lows. The offset is digitized to approximately connect the tips of the adjacent ridge segments. Of the two ridge segments per feature group, one is called the propagating ridge and one the failing ridge based on the propagation direction determined from the off-axis morphology of the SSP. Additional details and an example of a digitized feature group are given in Appendix B. In many cases, the rate of propagation may be low enough or the deformation patterns too complex to confidently determine the present direction of propagation (see Discussion).

In all, we digitize 55 ridge-offset-ridge features for model evaluation. We additionally digitize 69 ridge-transform fault-ridge features in a similar manner. We restrict the set of transform faults to the same ridge systems where we identify SSPs–i.e., the northern and southern Mid-Atlantic Ridge, the central and southeast Indian Ridge, and the Nazca-Antarctica Ridge. For each digitized ridge-offset-ridge feature, we estimate an offset shear resistance based on a range of yield strength models (friction coefficient of 0.3 to 0.7). For the ridge segments, we

estimate a loading force using the method described above. The success of the model is evaluated by two tests. The first tests the condition for instability described by equation 2.7. We add the loading forces of the two ridge segments and compare the sum to the offset shear resistance. If the condition for instability is met, then this test passes. The second tests whether the model predicts the right (observed) direction of propagation. The loading force of the propagating ridge segment ($F^*_{PR}$) is compared to the loading force of the failing ridge segment ($F^*_{FR}$), and if $F^*_{PR} > F^*_{FR}$, then this test passes.

## 2.4 Results

### 2.4.1 Major propagating ridges

We first test this model on major propagating ridges in two regions: the Cocos-Nazca spreading center and the southeast Indian Ridge (Figure 2.4a-b). We selected these systems because the propagation direction is unambiguous and has remained uniform over time. These tests are, in a loose sense, to validate the model approach and parameter selection–i.e., if the conditions for ridge propagation are not met at these obvious cases, then some part of the model is flawed.

The section of the Cocos-Nazca spreading center between the Galapagos hotspot and the Galapagos Triple Junction contains one of the earliest observed propagating ridges (Hey and Vogt; 1977) (Figure 2.4a). The primary feature in a suite of westward-propagating segments is a $\sim$ 500 km long segment bounded to the east by the Galapagos Transform Fault. To the west, the segment is truncated by a $\sim$ 40 km offset which is followed by a $\sim$ 100 km long failing ridge. The present half spreading rate is 30 mm/yr, and the ridge propagates westward 50 mm/yr relative to the plate boundary (Hey et al.; 1980). In the VGG maps, the inner pseudofault/sheared zone appear as a low, trending WNW-ESE, but the outer pseudofault does not have a strong signal. The Galapagos propagating ridge has been modeled with a fracture mechanics approach by Morgan and Parmentier (1985) who developed the energy balance we begin with in this study.

The suite of propagating ridges in the SEIR are not as well-studied as the Galapagos case, but the signature in the VGG maps is striking (Figure 2.4b). The series of westward propagating segments lies to the east of the Australian-Antarctic discordance, an anomalously deep section of the ridge (Palmer et al.; 1993). The ridge segments are axial highs, and the half spreading rate is $\sim$ 34 mm/yr (Seton et al.; 2020). In the VGG maps, the outer pseudofaults appear as continuous lows trending NE-SW, and the inner pseudofaults/sheared zones appear as linear discontinuous highs (ridges) trending NW-SE. Morgan and Sandwell (1994) identified these propagators using Geosat-derived gravity data and estimated propagation rates of 40-49 mm/yr based on the geometry of the outer pseudofaults and NUVEL-1 spreading rates (DeMets et al.; 1990). Another study of propagating ridges along the SEIR, West et al. (1999), includes the western-most of these features (SEIR_03).

Model results for each of these ridge-offset-ridge systems are shown in Figure 2.4c-d. The first test checks that the total loading force (the sum of the propagating and failing ridge forces) exceeds the resistance associated with the migration of the shear zone (calculated from equation 2.6). The estimated shear resistance depends strongly on the choice of coefficient of friction, so these values are shown as a gray bar representing the range of 0.3 to 0.7. In all 4 cases, the total loading force exceeds the shear resistance of the ridge offset for even the greatest friction coefficients, predicting that these segments are unstable and will propagate. The magnitude of these forces is, to first order, related to the length of the features. The longer ridge segments have greater loading forces, $F^*$, and the shorter segments have the lowest loading forces (e.g. Galapagos FR, SEIR_03). Shear resistance, $\Phi_O^*/U$, is also related to the length of the offset. Among these features, the offset lengths don't vary greatly, so neither do the estimates shear resistance.

The second test checks that our model correctly predicts the observed propagation direction. For each of the features shown in Figure 2.4a-b, 2.4d shows the estimated force along the adjacent propagating ridge (calculated from equation 2.5) compared to the estimated force along the adjacent failing/retreating ridge. In order for each ridge to propagate in the observed

direction, we expect the force along the propagating segment to exceed the force along the retreating segment. We find this is the case at three of the four offsets considered (Galapagos, SEIR_03, SEIR_02), while at the fourth (SEIR_01) the forces along the propagating and retreating segments are about equal. As mentioned in the first test, the ridge segment length is the greatest influencing factor on $F^*_{PR}$ and $F^*_{FR}$ here.

We have applied the model and tests to four cases of major propagating ridges, and we see the approach correctly predicts the migration of the ridge offsets for these cases. The test for propagation direction succeeds in three of the four cases. Next, we apply our model method to a larger catalog of ridge-offset-ridge features, both those that are observed to propagate and transform faults.

### 2.4.2 Transform faults

An important test of our model framework is that, in addition to predicting propagation, it should also predict stability at transform faults. Figure 2.5 shows the total loading force versus shear resistance for a set of 69 stable ridge-transform-ridge features, calculated using the same approach as Figure 2.4c. Across this set of features, there is a much wider range of shear resistance and total loading force values (note the logarithmic scales). For each feature, even the weakest shear resistance estimates exceed the loading force, typically by an order of magnitude or more. This is consistent with the observed stability of the features. The results for transform faults, especially when compared to the propagating ridge results, give us confidence that the model framework can distinguish between transform faults and propagating ridges/migrating offsets.

### 2.4.3 Seesaw propagators

Now we apply the model to the set of present day seesaw propagators (SSPs). The set of 55 SSPs comprises 34 features from the north and south Mid-Atlantic Ridge, 17 from the northern and southeast Indian ridge, and 4 from the Nacza-Antarctic ridge. All of these ridge

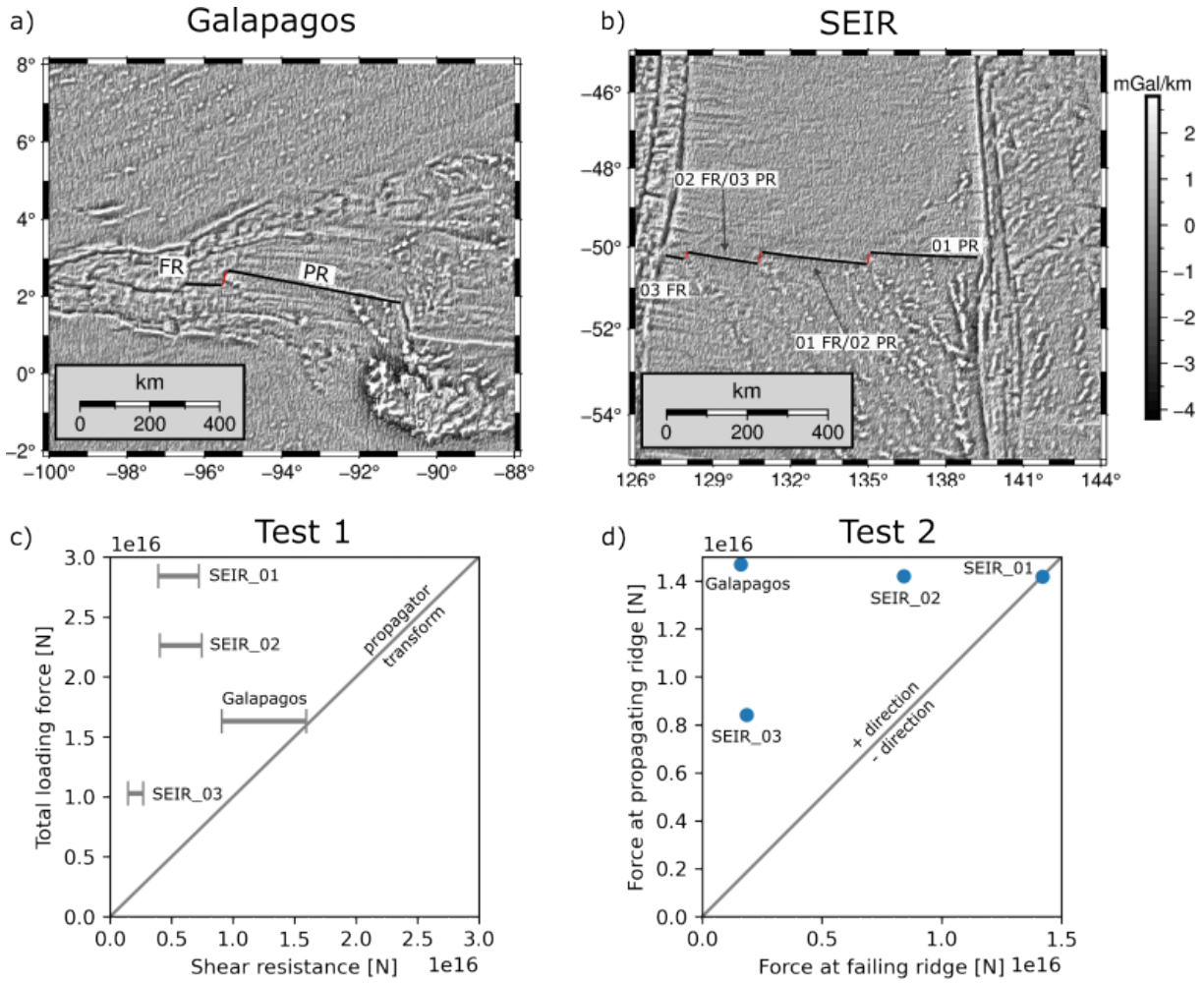


**Figure 2.4.** Vertical gravity gradient map view of (a) Galapagos propagating ridge and (b) southeast Indian propagating ridges. Individual segments (black lines) and offsets (red lines) are labeled. PR = propagating ridge, FR = failing ridge. (c) The total loading force on the ridge segments ($F^*_{PR} + F^*_{FR}$) vs the estimated shear resistance of the migrating offset. Area above the solid line (1:1) indicates the loading force exceeds the resistance and the offset is unstable. A range of strength models is shown, with friction coefficients from 0.3 (weakest) to 0.7 (strongest). (d) Loading forces on the failing and propagating ridges for the systems shown in (a,b). Solid gray line is 1:1.

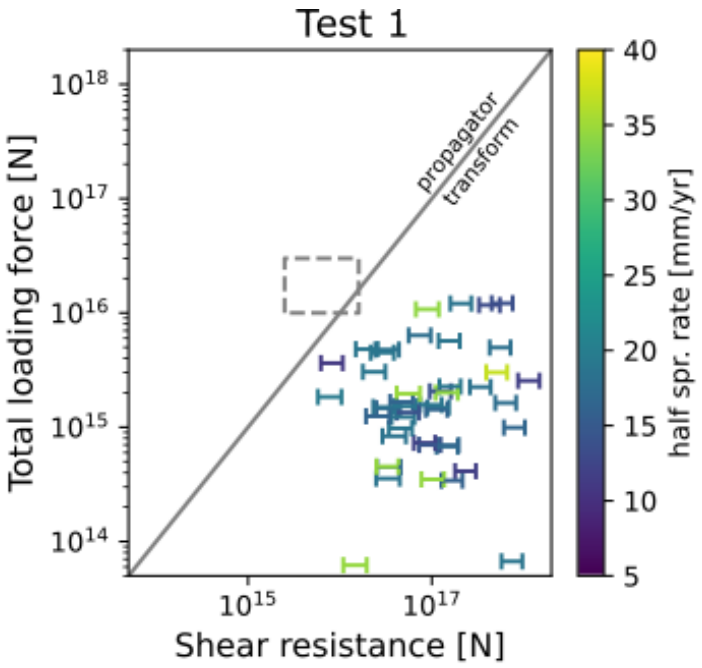


**Figure 2.5.** Results for stable transform fault offsets: total loading force on adjacent ridge segments vs. the estimated shear resistance of a migrating offset. Area below the solid gray line (1:1) indicates the shear strength exceeds the available loading force. Note the logarithmic scales. A range of strength models is shown with friction coefficients from 0.3 (weakest) to 0.7 (strongest). Points are shaded by half spreading rate (Seton et al.; 2020). Dash-outlined box shows the range of values in Figure 2.4c.

segments have axial valley morphologies. For this set of features, the half spreading rates range from 11 mm/yr to 37 mm/yr.

The results of the model tests are shown in Figure 2.6. Using the same driving force model as above, the estimated resisting force is too great to allow offset migration for many of the features (35/55) for even the weakest models of strength.

For 41/55 SSPs, the observed propagation direction is predicted by the model ($F^*_{PR} > F^*_{FR}$) (Figure 2.6b). Among the features that fail either of these tests, there are no exclusive underlying similarities (e.g., they aren't clustered spatially, no spreading-rate dependence). Among the features where the total loading force exceeds the shear resisting force, 18/20 of the observed propagation directions are predicted. There are 8/55 features with net negative loading forces. A negative loading force indicates the stress due to topography resists plate motion.

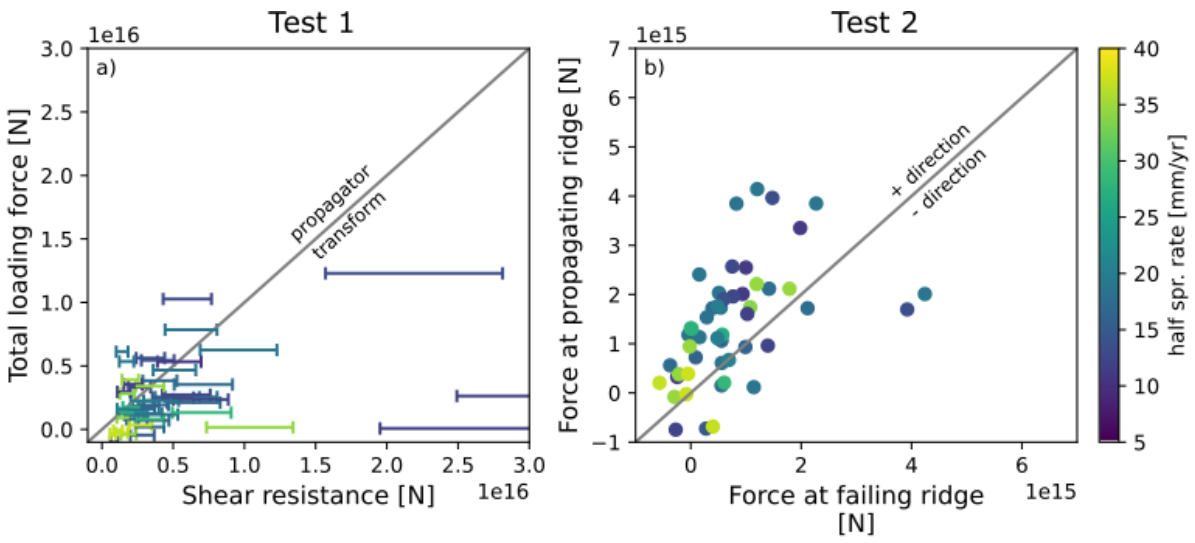


**Figure 2.6.** (a) The total loading force on the ridge segments ($F^*_{PR} + F^*_{FR}$) vs the estimated shear resistance of the migrating offset for the set of seesaw propagators (SSPs). Area above the solid line (1:1) indicates the loading force exceeds the resistance and the offset is unstable. A range of strength models is shown, with friction coefficients from 0.3 (weakest) to 0.7 (strongest). (b) Loading forces on the failing and propagating ridges for the set of SSPs. Solid gray line is 1:1. Points are shaded by half spreading rate (Seton et al.; 2020).

## 2.5 Discussion

In this study, we've built on the model framework proposed by Morgan and Parmentier (1985) to examine the stability of spreading ridge offsets and the relation to offset length and strength of the lithosphere. We posited that the forces driving ridge propagation must at least exceed the shear resistance of the lithosphere in the migrating shear zone region. We examined the success of this model framework with two tests applied to real ridge-offset-ridge features to determine whether the model 1) predicts the observed stability or propagation of a feature and 2) predicts the observed direction of propagation of a feature.

This model of ridge-offset stability succeeds for four cases of major ridge propagation (offset migration is possible). The model succeeds for all 69 cases of transform faults (stability is predicted). For slow-spreading seesaw propagators, the model only succeeds (offset migration is possible) in 20/55 cases using a yield strength envelope with a frictional coefficient of 0.3. The observed propagation direction is predicted by the model for 41/55 cases.

The model tests fail if the total loading force does not exceed the offset shear resistance or the failing ridge loading force exceeds the propagating ridge loading force. For the set of SSPs, there are only 20/55 cases where the first test passes, even using the weakest models of lithospheric strength. Considering a coefficient of friction as low as 0.1 does improve the results for SSPs (35/55 pass), but a strength model this weak would allow offset migration at one transform fault.

For SSPs, there are 14/55 cases where the wrong propagation direction is predicted. We consider that for such low rates of propagation or complex deformation patterns near the ridge axis, it's difficult to confidently label which ridge segment is presently propagating. We select 24 of the 55 SSPs for which we can confidently identify the present propagation direction, and find 20/24 are correctly predicted by the model–this is not much of an improvement, and we don't believe this explains much of the model's inaccuracy. There are many simplifying assumptions in the calculations and model framework that may contribute to the cases of failure, and we will examine those here.

### 2.5.1 Shear resistance exceeds loading force

For propagating ridges, the first model test fails when the total propagation force does not exceed the shear resistance associated with migrating the offset (equation 2.7 does not hold). The failure of the model in this way could be a result of overestimating the real strength of the lithosphere, or underestimating the real driving forces of propagation.

First, we will consider that the yield strength envelope model is overestimating the strength of the lithosphere. In estimating the total offset resistance, the most important component is the length of the offset. Each offset has a measured spreading rate which is inversely proportional to the total strength (but is proportional to the dissipation rate). The other yield strength parameters are free. For a given length offset, the total offset dissipation is most sensitive to the chosen friction coefficients. However, the friction coefficients we have considered (0.3) are very low. Even with a friction coefficient of 0.1, 20/55 of the seesaw propagators fail this test.

The other major influence on yield strength is the temperature of the medium. At the ridge-offset intersection, 3-D variations in thermal structure are significant. Simple 2-D thermal models can't be applied without some modification (the total strength will be far too high). We use the simple approach of averaging two temperature profiles to overcome this problem (Abercrombie and Ekstrom; 2001). There are some differences in the resulting isotherms compared to a more sophisticated model–e.g., Behn et al. (2007) predict isotherms are deepest at ridge-offset intersections rather than the offset midpoint. However, the total strength would not be affected by this.

In addition to a possible overestimate of lithospheric strength, our estimate of ridge loading force may also be biased. In describing the methods for calculating $F^*$, we mentioned the masking and filtering steps we apply to the global topography. One of the goals of this processing is to approximately separate the long wavelength force driving plate motion, $F$, from the short wavelength force, $F^*$, from excess topography. Using the filter approach, we must decide on appropriate spherical harmonic degrees for the cosine taper, so there is ambiguity in the absolute magnitude of the ridge push force. We note that as longer wavelengths are removed from the input topography model, the estimated force decreases, and fewer example features will have sufficient loading force to overcome the offset shear resistance.

In addition, there are some constraints in the stress model that are worth exploring. We presented model results for uniform crustal thickness of 6 km. Using a slightly thicker crust of 8 km, the first order effect will be an increase in loading force since the limits of integration in equation 2.8 are increased by 2 km. Increasing the crustal thickness to 8 km globally, the test results improve to 30/55 cases passing. However, the thicker crust changes the internal stress field in ways that are not obvious, and the predictions of propagation direction suffer.

**Model framework**

Beyond necessary simplifications in the calculations of force and resistance, there are physical processes our model framework doesn't include. One possibility is that the mechanism

of deformation is not accurately described by our model. Perhaps a two-stage accretion model (Grevemeyer et al.; 2021) or the local off-transform deformation of the crust (Zhang et al.; 2022) may create instabilities and initiate the onset of propagation episodes. We also note the lack of excess resisting forces along the ridge axis in our model–however, the exclusion of these doesn't interfere with the criterion that the driving forces must at least exceed offset shear resistance.

Finally, loading forces that are not expressed in the topography may influence the stability of offsets or the direction of ridge propagation. Our model has assumed all of the loading force is due to excess topography. There are possibly non-isostatic regional forces such as along-ridge asthenosphere flow driving ridge offset instability (e.g. West et al.; 1999). Segment-scale effects such as dynamic upwelling of magma sources may provide additional propagation forces (e.g. Zheng et al.; 2019). Such localized effects are likely important for seesaw propagators, where propagation direction is not consistent for adjacent features and changes over time.

### 2.5.2 Direction of propagation

The other type of model failure is when the driving force along the observed failing ridge exceeds the driving force along the propagating ridge $F^*_{FR} > F^*_{PR}$. Why might the model fail in these cases? The discussion of the biases in estimating loading force applies to this problem as well. When the input topography is filtered to shorter wavelengths, the results change in non-obvious ways. Using a cosine taper filter from spherical harmonic degrees 20 to 30 ($\sim 1900 - 1290$ km), the results for this test are slightly worse (38/55 pass). As mentioned in the previous section, when more long wavelength topography is removed, the total loading force is too small.

The same factors regarding the ridge loading model framework mentioned in the previous section are also important here. It's possible we are missing non-isostatic driving forces contributing to loading on either ridge segment. It's important to note that for SSPs, the observed direction of propagation is not consistent spatially–i.e., adjacent propagators do not necessarily propagate in the same direction. For this reason, we believe local effects are more likely than

missing regional mechanisms.

Finally, our model attempts to isolate ridge-offset-ridge features from the greater series of spreading ridges and offsets that comprise the whole mid-ocean ridge system. For example, how does one propagating ridge/migrating offset affect the adjacent ridge offsets–are propagation forces that aren't dissipated within that feature added to the propagation force of another segment? The complex inter-relationships of such a system are beyond the specific scope of this model.

### 2.5.3 Comparisons to other models

As previously stated, our model is based on an energy balance presented by Morgan and Parmentier (1985), and we will clarify some key differences between our models. One major difference is in our treatment of the forces resisting propagation where we suggest the limiting factor is resistance associated with migrating the ridge offset. In contrast, Morgan and Parmentier (1985) models the limiting resistive process as dynamic viscous forces in an axial magma chamber–we don't model any viscous processes on the ridge axis. Calculating a viscous resisting force requires an estimate of propagation rate which, for many of the features in this study, is very low.

West et al. (1999) applied the Morgan and Parmentier (1985) model framework to five propagating ridges of the southeast Indian Ridge. Four of these features lie to the west of the Australian-Antarctic discordance (AAD) and presently propagate eastward; the other (the same feature as SEIR_03 of this study) lies to the east of the AAD and propagates westward. Their application of the model predicts the incorrect sense of propagation for all features, so they require an additional regional force, along-axis asthenospheric flow, to drive propagation towards the AAD. This study includes four of the five features from West et al. (1999), and for each of those, the condition for instability is met for low coefficients of friction and the correct direction of propagation is predicted.

Complex propagation patterns are likely a result of variations in mantle melting at individual ridge segments, and this is treated more explicitly in magmatic models such as

Tucholke et al. (1997); Dannowski et al. (2018); Zheng et al. (2019) among others. For example, increased melt supply at a segment will increase the amount of plate motion accommodated by magmatic emplacement and decrease ridge-normal strain, while segments with decreased melt supply will undergo increased tectonic strain (e.g. Wang et al.; 2015). Varying tectonic strain rates at adjacent segments may result in ridge propagation, but in some cases the along-ridge migration of a magmatic body may be what drives ridge propagation (Martinez et al.; 2020). Such models are not necessarily mutually exclusive to our approach since our driving forces, calculated from topography, are likely magmatic in origin. A possible implication of magmatic models is that the migration of short offsets (and stability of larger offsets) is related to the continuity of mantle upwelling regimes (Martinez and Hey; 2022). This is quite different from our yield strength hypothesis, but not mutually exclusive, since migration of a shear zone is still necessary. However, in our model, we do not account for differing strength profiles that may be the result of complex mantle melting patterns (Martinez and Hey; 2022).

### 2.5.4 Model implications

Estimates of ridge loading forces may be biased and the modeling of deformation may be too simplistic to explain all cases of ridge propagation, but conceptually this model attempts to describe a ridge segment system that wants to constantly evolve but is held together or buttressed by strong lithosphere at long offsets. When excess driving forces are great enough, this configuration is degraded. This is why large-scale regional anomalies, even if the offsets are of great length, can propagate. This also explains why those large propagators are mostly unidirectional as the driving force is not likely to rapidly reverse. Short offsets, where the energy requirement is not so great, may migrate in response to smaller changes along ridge segments–changes that reverse relatively quickly, resulting in "seesaw" propagation and general offset instability. The question remains–what are the causes of seesaw propagation? There are many non-exclusive potential mechanisms, but they are most likely related to complex patterns of small-scale mantle melting and convection (Dannowski et al.; 2018; Zheng et al.; 2019; Martinez

and Hey; 2022). Our model is agnostic to the origin of these forces, but assumes they are expressed topographically. Similarly, the lengthening or shortening of an offset and the transition from unstable to stable offset, or vice versa (e.g. Matthews et al.; 2011), is not explained by our model.

We have mentioned that our model of shear zone deformation may be too simplistic to explain all cases of ridge propagation. Using the basic yield strength envelope approach, we have made some qualitative observations of offset zone lithospheric strength that we believe may be related to ridge offset stability. Depending on the choice in crustal rheology, a weak zone may develop in the lower crust where ductile crust overlies a rigid mantle. This modeled weak zone resembles the decoupling layer suggested by Chen and Morgan (1990), and it is possible that the presence of a lower decoupling region in the offset zone aids offset migration by reducing the shear strength of the lithosphere.

Plate coupling introduces additional complexities to shear zone deformation and the physics of our model. If plate coupling at an offset is too low, the energy from excess spreading force will not all be dissipated by shear deformation. At weakly-coupled transform faults, this would effectively reduce the total loading force of the ridges. In our model, we are establishing a threshold on how much energy is required to migrate an offset, and this should be independent of the plate coupling. The influence of plate coupling, especially as the quantity varies with offset length or how it might relate to the yield strength envelope, is surely important to the problem of ridge propagation, but we have not addressed those complexities here.

**Minimizing resistance**

Recall the classic argument that the configuration of ridges and transform faults seeks to minimize the resistance to plate motion (Lachenbruch and Thompson; 1972). Assume, for any ridge offset, there is a transform fault with a given average shear strength of 10 MPa. For short offsets, it may be that the the strength of the lithosphere (computed from the YSE) is weaker than a transform fault, so the transform fault is not the path of least resistance. By seeking to

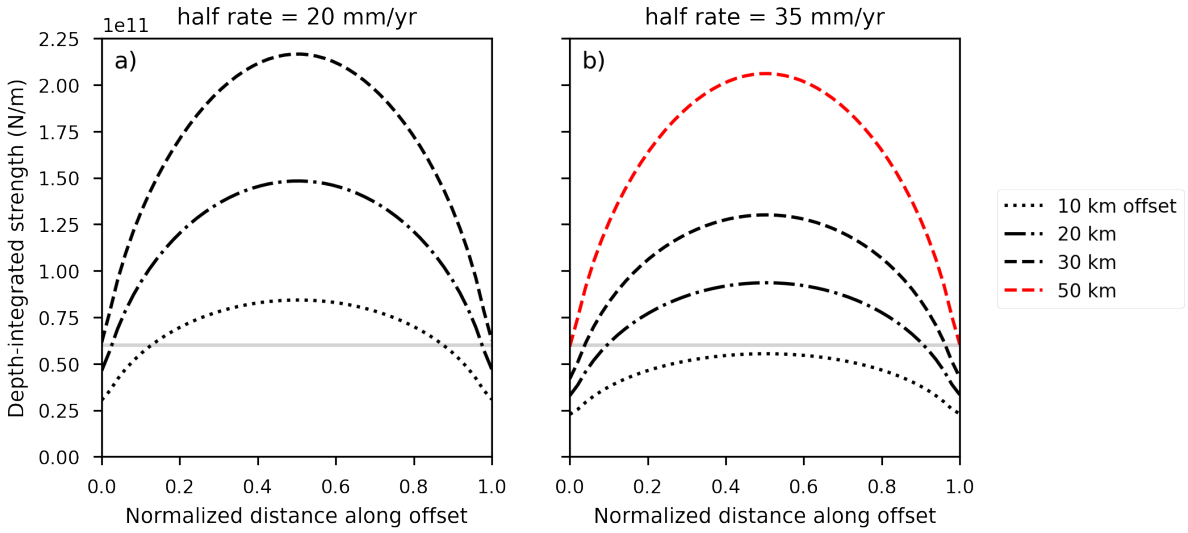


**Figure 2.7.** Depth-integrated shear strength vs. normalized distance along an offset for growing offset length. (a) friction coefficient of 0.7, crustal thickness of 6 km, half spreading rate of 20 mm/yr; (b) friction coefficient of 0.7, crustal thickness of 6 km, half spreading rate of 35 mm/yr. In both figures, the solid line is the strength of a theoretical transform fault using an estimated 10 MPa shear strength (integrated over a 6 km crust).

minimize the resistance to spreading motion, off-transform deformation and ridge propagation may result from young, weak lithosphere.

Figure 2.7 shows such a comparison of yield strength at an offset to an average strength of 10 MPa typical of oceanic transform faults (Morgan and Parmentier; 1984). For shorter offsets, the relatively weak lithosphere may accommodate shear strain with less resistance than a pre-existing transform fault, and deformation proceeds into an overlap zone. For larger offsets, the lithosphere is stronger than the transform fault, so deformation is confined to this weakly-resistant zone. There will be variability in this offset length threshold due to real thermal complexities, spreading rate, and crustal thickness, but this simple argument avoids assumptions about the ridge loading force.

## 2.6 Conclusions

We began this study with observations of seesaw propagating ridges at slow- and intermediate-spreading sites. For this set of SSPs, the maximum ridge offset length is about 30 km–larger offsets are transform faults, and ridge propagation is rarely observed. We hypothesized that the strength of the lithosphere at a ridge offset limits whether a ridge can propagate and that this could explain the threshold offset length between propagating ridges and transform faults. Adapting a framework developed by earlier workers, we tested this hypothesis on observed transform faults and propagating ridges/migrating offsets. We found that major propagating ridges and transform faults support our framework. For a set of seesaw propagators, the model framework does not work strictly, but it's clear that the features are a population distinct from stable transform faults. It stands that the weak lithosphere at small offsets is essential to produce ridge propagation and, conversely, that strong lithosphere at transform faults contributes to their stability.

## 2.7 Appendix: Yield strength envelope parameters

### 2.7.1 Brittle strength parameters

To compute the brittle strength of the lithosphere, we use Byerlee's law which has the form:

$$\tau_S = S_0 + \mu \sigma_n \,, \tag{2.12}$$

where $S_0$ is the cohesion, $\mu$ is the coefficient of friction, and $\sigma_n$ is the normal stress. Although Byerlee (1978) suggested a piecewise function for low and high normal stress, the models in this study use a single coefficient of friction (or a range of coefficients for different models) and zero cohesion. The normal stress is a combination of water column overburden, rock overburden, and pore fluid pressure. We give the top 6 km of the lithosphere (the crust layer) a density of $\rho_c = 2900$ kg m $^{-3}$ and the deeper lithosphere a density of $\rho_m = 3300$ kg m $^{-3}$. In the top 6 km,

we include the influence of pore fluids as a ratio of pore fluid pressure to lithostatic pressure (Brace and Kohlstedt; 1980) which has the effect of lowering the brittle yield strength.

### 2.7.2 Ductile flow law and parameters

The ductile strength is computed using a power law flow model (Goetze; 1978) which has the form:

$$\tau_S = \left(\frac{\dot{\varepsilon}}{A}\right)^{1/n} \exp\left(\frac{Q}{nRT}\right) \tag{2.13}$$

$T$ is temperature, $R$ is the ideal gas constant. The material constant $A$, activation energy $Q$, and stress exponent $n$ are laboratory-derived quantities dependent on mineral composition. We use parameters for wet olivine in the top 6 km ($n = 3, A =$ 1.9e-15 $\text{Pa}^{-n}$ $\text{s}^{-1}$, $Q =$ 4.2e5 J $\text{mol}^{-1}$) (Karato et al.; 1986), and dry olivine in the lower lithosphere ($n = 3.5, A =$ 2.4e-16 $\text{Pa}^{-n}$ $\text{s}^{-1}$, $Q =$ 5.4e5 J $\text{mol}^{-1}$) (Karato et al.; 1986). Strain rate $\dot{\varepsilon}$ is set to 1e-14 $\text{s}^{-1}$.

## 2.8 Appendix: Example digitized ridge segments

Because the VGG includes the gravitational effects of both bathymetry and the Moho, it is a better independent resource for identifying the ridge axis than bathymetry alone. However, when the ridge axis is not obvious in the VGG, we use depth data from SRTM15+V2 (Tozer et al.; 2019) to help identify the extent of the ridge. Figure 2.8 shows an example of digitized ridge segments and ridge offset. While high-resolution bathymetry shows greater short-wavelength detail than the vertical gravity gradient (VGG), the ridge axis is more prominent in the VGG. Subtle ridge discontinuities such as devals are ignored in our digitizations, and they are suppressed in the VGG due to a lack of Moho compensation. Ridge segments are terminated at offsets or, in some cases, changes in trend of ridge axis.

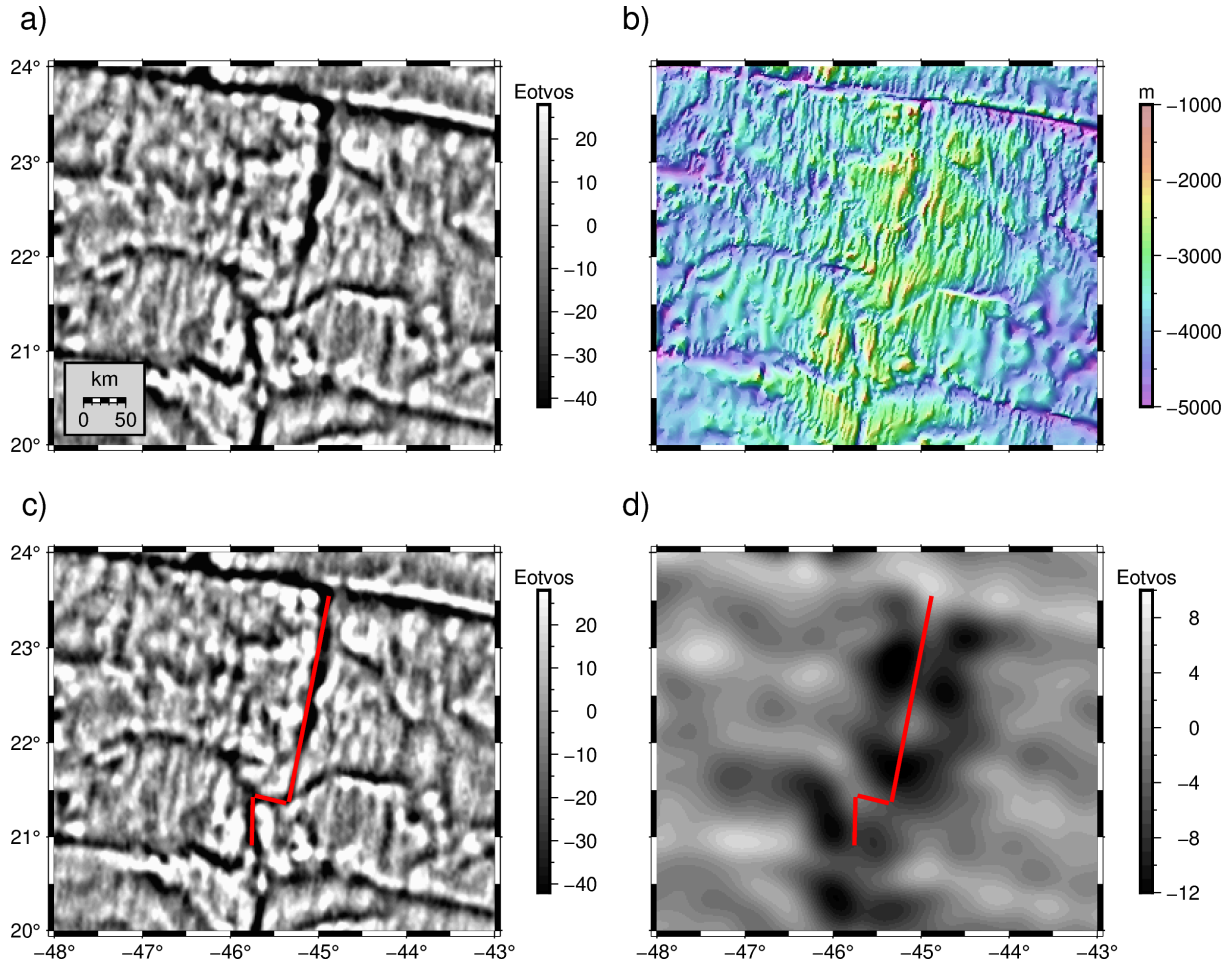


**Figure 2.8.** An example in the North Atlantic. a) Satellite-derived vertical gravity gradient (VGG). b) Bathymetry at 15 arc second resolution (Tozer et al.; 2019). c) The VGG with digitized ridge segments and migrating offset shown in red. d) The VGG signal from the Moho, computed from bathymetry, a mean crustal thickness of 6 km, and an elastic thickness of 3.2 km that minimizes rms error near the ridge axis; digitized features from (c) are overlain.

## 2.9 Acknowledgements

We thank Ross Parnell-Turner, Dave May, and Jeff Gee for their suggestions and comments on an earlier version of the manuscript. We thank the associate editor and two anonymous reviewers for their constructive feedback that greatly improved the quality of this manuscript. This work was supported by the NASA SWOT program (80NSSC20K1138) and the Office of Naval Research (N00014-17-1-2866). Hugh Harper was supported by a NASA FINNEST fellowship (80NSSC20K1616).

This chapter, in full, is a reprint of material that has been submitted for publication in the Journal of Geophysical Research Solid Earth: Harper, H.; Luttrell, K.; Sandwell, D. T. "Ridge propagation and the stability of small mid-ocean ridge offsets", in rev. The dissertation author was the primary investigator and author of this paper.

# References


Abercrombie, R. E. and Ekstrom, G. (2001). Earthquake slip on oceanic transform faults, *Nature* **410**.

Behn, M. D., Boettcher, M. S. and Hirth, G. (2007). Thermal structure of oceanic transform faults, *Geology* **35**: 307–310.

Behn, M. D., Lin, J. and Zuber, M. T. (2002). Evidence for weak oceanic transform faults, *Geophysical Research Letters* **29**: 1–4.

Boettcher, M. S. and Jordan, T. H. (2004). Earthquake scaling relations for mid-ocean ridge transform faults, *Journal of Geophysical Research: Solid Earth* **109**: 1–21.

Brace, W. F. and Kohlstedt, D. L. (1980). Limits on lithospheric stress imposed by laboratory experiments, *Journal of Geophysical Research* **85**: 6248–6252.

Brozena, J. M. and White, R. S. (1990). Ridge jumps and propagations in the south atlantic ocean, *Nature* **348**: 149–152.

Byerlee, J. (1978). Friction of rocks, *Rock friction and earthquake prediction*, Springer, pp. 615–626.

Carbotte, S. M., Smith, D. K., Cannat, M. and Klein, E. M. (2016). Tectonic and magmatic segmentation of the global ocean ridge system: A synthesis of observations, *Geological Society Special Publication* **420**: 249–295.

Chen, Y. J. and Morgan, W. J. (1990). Rift valley/no rift valley transition at mid-ocean ridges, *Journal of Geophysical Research* **95**: 17571–17581.

Dannowski, A., Morgan, J., Grevemeyer, I. and Ranero, C. (2018). Enhanced mantle upwelling/melting caused segment propagation, oceanic core complex die off, and the death of a transform fault: the mid-atlantic ridge at 21.5n, *Journal of Geophysical Research: Solid Earth* **123**.

DeMets, C., Gordon, R. G., Argus, D. and Stein, S. (1990). Current plate motions, *Geophysical journal international* **101**(2): 425–478.

Goetze, C. (1978). The mechanisms of creep in olivine, *Philosophical Transactions of the Royal Society of London. Series A, Mathematical and Physical Sciences* **288**(1350): 99–119.

Grevemeyer, I., Rüpke, L. H., Morgan, J. P., Iyer, K. and Devey, C. W. (2021). Extensional tectonics and two-stage crustal accretion at oceanic transform faults, *Nature* **591**: 402–407.

Grindlay, N. R. and Fox, P. J. (1993). Lithospheric stresses associated with nontransform offsets of the mid-atlantic ridge: implications from a finite element analysis, *Tectonics* **12**: 982–1003.

Grindlay, N. R., Fox, P. J. and MacDonald, K. C. (1991). Second-order ridge axis discontinuities in the south atlantic: Morphology, structure, and evolution, *Marine Geophysical Researches* **13**: 21–49. Probably the key paper to cite.

Harper, H., Tozer, B., Sandwell, D. T. and Hey, R. N. (2021). Marine vertical gravity gradients reveal the global distribution and tectonic significance of "seesaw" ridge propagation, *Journal of Geophysical Research: Solid Earth* pp. 1–16.

Hey, R. (1977). A new class of "pseudofaults" and their bearing on plate tectonics: A propagating rift model, *Earth and Planetary Science Letters* **37**: 321–325.

Hey, R. (2001). Propagating rifts and microplates, *Encyclopedia of Ocean Sciences* pp. 597–605.

Hey, R., Duennbier, F. K. and Morgan, W. J. (1980). Propagating rifts on midocean ridges, *Journal of Geophysical Research* **85**: 3647–3658.

Hey, R., Martinez, F., Höskuldsson, Á. and Benediktsdóttir, Á. (2010). Propagating rift model for the v-shaped ridges south of iceland, *Geochemistry, Geophysics, Geosystems* **11**(3).

Hey, R. and Vogt, P. (1977). Spreading center jumps and sub-axial asthenosphere flow near the galapagos hotspot, *Tectonophysics* **37**: 41–52.

Karato, S.-I., Paterson, M. S. and Fitzgerald, J. D. (1986). Rheology of synthetic olivine aggregates: influence of grain size and water, *Journal of Geophysical Research* **91**: 8151–8176.

Kleinrock, M. C., Tucholke, B. E., Lin, J. and Tivey, M. A. (1997). Fast rift propagation at a slow-spreading ridge, *Geology* **25**: 639–642.

Lachenbruch, A. H. and Thompson, G. A. (1972). Oceanic ridges and transform faults: their intersection angles and resistance to plate motion, *Earth and Planetary Science Letters* **18**.

Luttrell, K. and Sandwell, D. (2012). Constraints on 3-d stress in the crust from support of mid-ocean ridge topography, *Journal of Geophysical Research: Solid Earth* **117**: 1–19.

Martinez, F. and Hey, R. (2022). Mantle melting, lithospheric strength and transform fault stability: Insights from the north atlantic, *Earth and Planetary Science Letters* **579**.

Martinez, F., Hey, R. and Ármann Höskuldsson (2020). Reykjanes ridge evolution: Effects of plate kinematics, small-scale upper mantle convection and a regional mantle gradient, *Earth-Science Reviews* **206**.

Matthews, K. J., Mller, R. D., Wessel, P. and Whittaker, J. M. (2011). The tectonic fabric of the ocean basins, *Journal of Geophysical Research: Solid Earth* **116**: 1–28.

Morgan, J. P. and Parmentier, E. (1984). Lithospheric stress near a ridge-transform intersection, *Geophysical Research Letters* **11**.

Morgan, J. P. and Parmentier, E. (1985). Causes and rate limiting mechanisms of ridge propagation: A fracture mechanics model, *Journal of Geophysical Research* **90**: 8603–8612.

Morgan, J. P. and Sandwell, D. T. (1994). Systematics of ridge propagation south of 30 degrees s, *Earth and Planetary Science Letters* **121**.

Oldenburg, D. W. and Brune, J. N. (1972). Ridge transform fault spreading pattern in freezing wax, *Science* **178**: 301–304.

Oldenburg, D. W. and Brune, J. N. (1975). An explanation for the orthogonality of ocean ridges and transform faults, *Journal of Geophysical Research* **80**: 2575–2585.

Palmer, J., Sempéré, J.-C., Christie, D. M. and Morgan, J. P. (1993). Morphology and tectonics of the australian-antarctic discordance between 123 e and 128 e, *Marine Geophysical Researches* **15**(2): 121–152.

Seton, M., Müller, R. D., Zahirovic, S., Williams, S., Wright, N. M., Cannon, J., Whittaker, J. M., Matthews, K. J. and McGirr, R. (2020). A global data set of present-day oceanic crustal age and seafloor spreading parameters, *Geochemistry, Geophysics, Geosystems* **21**: 1–15.

Shi, P., Wei, M. M. and Pockalny, R. A. (2022). The ubiquitous creeping segments on oceanic transform faults, *Geology* **50**: 199–204.

Tozer, B., Sandwell, D. T., Smith, W. H., Olson, C., Beale, J. R. and Wessel, P. (2019). Global bathymetry and topography at 15 arc sec: Srtm15+, *Earth and Space Science* **6**: 1847–1864.

Tucholke, B. E., Lin, J., Kleinrock, M. C., Tivey, M. A., Reed, T. B., Goff, J. and Jaroslow, G. E. (1997). Segmentation and crustal structure of the western mid-atlantic ridge flank, 25deg 25'-27deg 10'n and 0-29 m.y., *Journal of Geophysical Research: Solid Earth* **102**: 10203–10223.

Wang, T., Tucholke, B. E. and Lin, J. (2015). Spatial and temporal variations in crustal production at the mid-atlantic ridge, 25deg n–27deg 30'n and 0–27ma, *Journal of Geophysical Research: Solid Earth* **120**.

Watts, A. B. (2001). *Isostasy and Flexure of the Lithosphere*, Cambridge University Press.

West, B. P., Lin, J. and Christie, D. M. (1999). Forces driving ridge propagation, *Journal of Geophysical Research: Solid Earth* **104**: 22845–22858.

Zhang, F., Lin, J., Zhou, Z., Yang, H. and Morgan, J. P. (2022). Mechanism of progressive broad deformation from oceanic transform valley to off-transform faulting and rifting, *The Innovation* **3**.

Zheng, T., Tucholke, B. E. and Lin, J. (2019). Long-term evolution of nontransform discontinuities at the mid-atlantic ridge, 24n–27 30n, *Journal of Geophysical Research: Solid Earth* **124**: 10023–10055.

# Chapter 3

# Global predicted bathymetry using neural networks

## 3.1 Introduction

Less than 25% of the ocean floor has been mapped at 15 arcsecond resolution (GEBCO compilation group; 2023), and at 1 arcminute resolution, this figure is still less than 30%. From efforts such as the Seabed 2030 project (Mayer et al.; 2018), coverage in publicly-available compilations has improved in recent years, but the distribution of shipboard depth measurements remains heterogeneous and sparse, providing nearly complete high resolution coverage in some coastal areas but leaving unmapped gaps the size of western US states in remote regions (Figure 3.1a). While there is no substitute for shipboard surveys to recover high resolution bathymetry, we can make a good guess of the seafloor depth, at a limited resolution, in these gaps using gravity field data derived from satellite altimeters (e.g Smith and Sandwell; 1994).

Satellite measurements have provided a wealth of information on the gravity field with global coverage, at a resolution of 12 km and accuracy nearing 1 mgal (Sandwell et al.; 2021). A new generation of swath altimeters will improve the resolution of the gravity field may improve the accuracy beyond 1 mgal. Since gravity anomaly and depth are correlated within certain wavelength bands (Smith; 1998), we can infer depth from gravity. Within a restricted region, depths may be directly inverted from gravity measurements (e.g. (Parker; 1972)), but this requires a priori knowledge of crustal density other geologic quantities such as the degree of isostatic

compensation (Watts; 2001). There are limitations to this method preventing its application at very large scales. How exactly one should combine sparse depth measurements with global gravity measurements to generate global predicted depths is not trivial.

Smith and Sandwell (1994) developed (and revised in Smith and Sandwell (1997)) an algorithm for this purpose with tremendous success. The procedure uses admittance theory to design filters for bathymetry and gravity to linearize their relationship. The filtering steps remove most assumptions of isostatic compensation. After filtering, they determine the local slope of the bathymetry-gravity relationship on a coarse grid–full details may be found in Smith and Sandwell (1994)–and the predicted bathymetry is the product of the filtered gravity and slope. This paper terms the post-filtering process the "inverse Nettleton," referring to Nettleton (1939) to describe the process of selecting a best-fitting slope to describe the relationship of gravity anomaly and topography. As such, we will refer to this method as the Nettleton method. The quality of the estimation has improved with increasingly precise gravity recovery (number of measurements, orbits, instrument quality, processing techniques) and the greater quantity of shipboard measurements, especially in the so-called gaps. The most recent iteration of this prediction is described in detail by Tozer et al. (2019). While the predicted depth product has been widely adopted, some of the details in the prediction method may not be optimal and leave room for improvement.

There has been recent interest in using modern methods from machine learning to improve upon the prediction of bathymetry. For example Annan and Wan (2022) and Wan et al. (2023) have used neural networks with various architectures to predict absolute depth from gravity and gravity-related quantities (e.g. deflections of the vertical, gravity gradients). An investigation by Moran et al. (2022) tested many machine learning algorithms in an attempt to predict depth from a set of geophysical and oceanographic features. These models are all limited to a particular study area–training and predictions are restricted to selected regions. The present study is an attempt to update the global predicted depth grid, and our goal is to replace the Nettleton method of depth estimation with a new approach using techniques from machine learning. Specifically,

we will train a deep neural network (DNN) to predict depth using a publicly-available collection of depth measurements. We distinguish our method from previous predicted bathymetry studies in a few key ways: we attempt a global prediction; we predict depth in a certain waveband rather than the absolute depth; and we split training and testing data in a unique way.

## 3.2 Methods

Jupyter notebooks to reproduce the steps described below are available at https://doi.org/10.5281/zenodo.8029925 (Harper and Sandwell; 2023).

### 3.2.1 Data preparation and feature generation

We begin with the collection of shipboard depth measurements. The collection is based on the collection used in the SRTM15+V2 product (Tozer et al.; 2019), and a description of the data sources is found in that study and Becker et al. (2009). Since Tozer et al. (2019), data from 905 cruises (retrieved from NCEI) have been added to the collection. Data have been manually edited to remove erroneous measurements. For our purposes, data provenance is treated equally, and data are not distinguished by cruise ID or instrument type (multibeam or single-beam). Raw shipboard data are reduced by a median filter to 15 arcsecond resolution. These data are combined and blockmedian-reduced to 1 arcminute resolution on a spherical Mercator projected grid, spanning -80.738° to 80.738° latitude. The result is a collection of 52,253,670 records of type [longitude, latitude, depth] (or $[\phi, \theta, d]$).

We can use the coordinates $\phi, \theta$ of any constrained depth record to sample the global gravity anomaly grid (Figure 3.1c) (Sandwell et al.; 2021). Since the constrained depth cells are co-registered with the gravity grid, sampling is trivial, but sampling may also be done via interpolation. The result is records of type $[\phi, \theta, d, g]$. From these records, the target quantity we wish to predict is depth, and the features we may use to train the prediction are $\phi, \theta$, and $g$. We could use other geophysical or geographical grids as features, since they can be sampled by longitude and latitude. We will explore such additional features in the discussion.

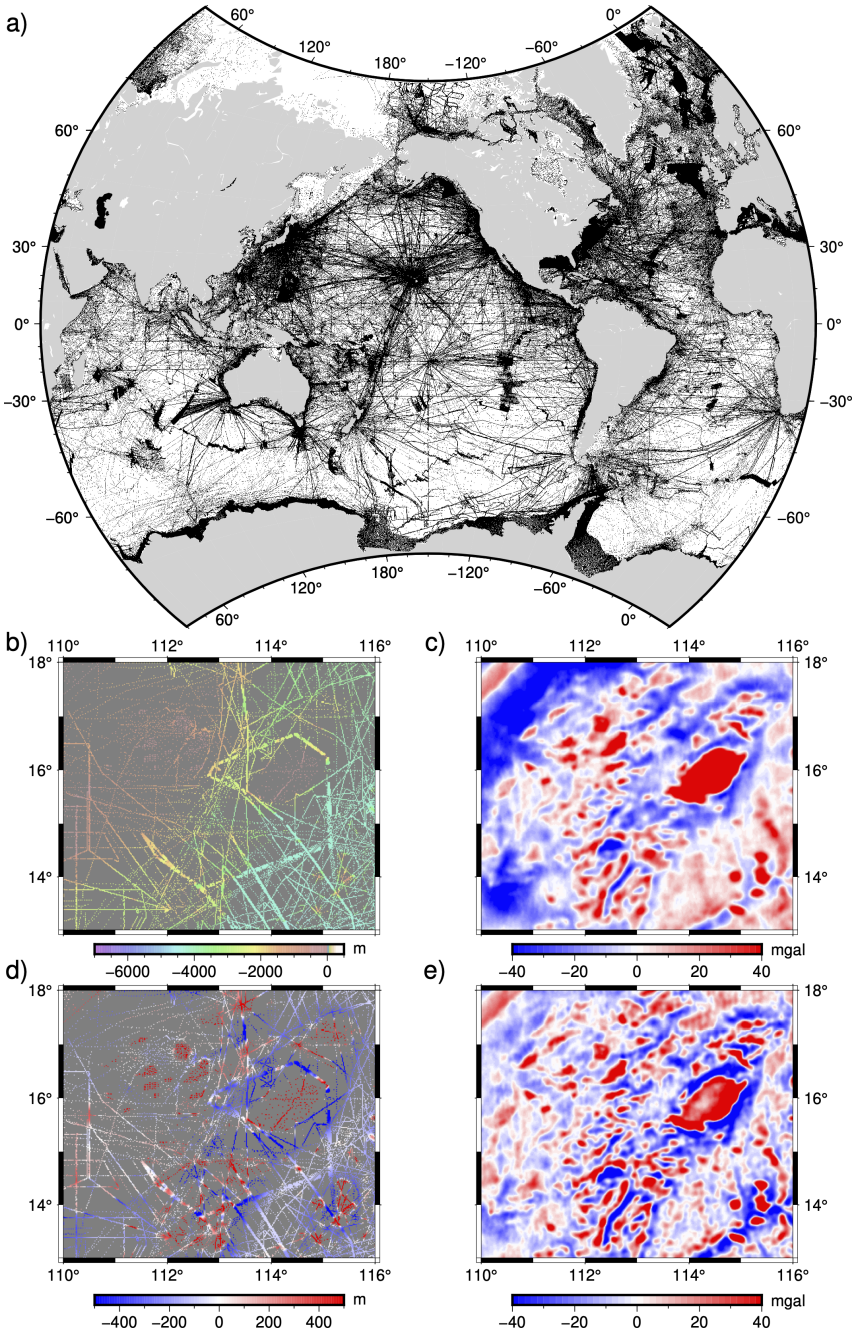


**Figure 3.1.** An overview of the datasets in map view. (a) Distribution of shipboard depth measurements in the global oceans based on publicly-available data. (b) Zoomed-in view of depth measurements in the South China Sea, colored by absolute depth. (c) Free air gravity anomaly for the same region as (b). (d) High-pass filtered depths and (e) filtered gravity anomaly–filtering described in the text.

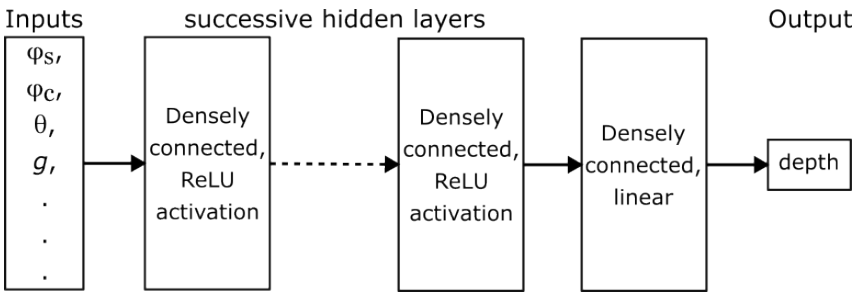


**Figure 3.2.** Schematic of the neural network architecture. A feature vector with normalized inputs is transformed by successive hidden layers to predict depth.

That longitude is cyclical is not captured by the simple numerical value, so we decompose the longitude, $\phi$, to $\sin\left(\frac{\phi\pi}{180}\right)$ and $\cos\left(\frac{\phi\pi}{180}\right)$, or $\phi_s, \phi_c$. With this treatment of longitude, we avoid a discontinuity at the Greenwich Meridian in the predicted depth grid. Following this amendment, our feature vector is $[\phi_s, \phi_c, \theta, g]$.

**Filtering depth and gravity**

Since gravity and bathymetry are only correlated over certain wavelengths (Smith; 1998), it would be less-than-optimal to try and predict the absolute depth. Here we use the filtering steps established by Smith and Sandwell (1994). The depth measurements are gridded on a 1 arcminute spherical Mercator grid using continuous splines in tension (Smith and Wessel; 1990), and this grid is separated into low- and high-frequency components with a Gaussian filter with 0.5 gain at 160 km (eq. 9, (Smith and Sandwell; 1994)). The low-pass depth grid is saved. The high-pass depth is then low-pass filtered with 0.5 gain at 16 km, resulting in a 160 km - 16 km band-pass depth grid–we will call this $h$. The constrained points of this depth grid are extracted (Figure 3.1d). We are losing some high-frequency information this way in order to match the spectral content of the gravity. The gravity anomaly is high-pass filtered in the same way as the depth measurements. Finally, the high-pass filtered gravity anomaly is downward-continued to the low-pass filtered depth using a depth-dependent Wiener filter (eq. 11, (Smith and Sandwell; 1994))–we will call this $g^*$(Figure 3.1e). We will examine the effects of omitting this pre-processing step in the discussion.

### 3.2.2 Data splitting

We must split our dataset into training, validation, and testing sets. If we are to simply select 20% for testing and validation at random, then we will find that almost any given record in the testing or validation set is within 1 arc minute of a record in the training set. Marks et al. (2010), analyzing predicted depths generated by the Nettleton procedure, showed the prediction error increases with distance from constrained nodes. How strong this effect is depends on the roughness of the seafloor, but it appears the errors become decorrelated beyond a certain distance (15-30 km). In other words, records that are sufficiently close in position are not independent (Figure 3.3b). In practice, the training loss and validation (and testing) loss will be nearly identical, and we will not have a good idea of when the model is overfitting during training or how the model generalizes to the unmapped gaps.

By splitting the data into longitude, latitude bins and randomly selecting bins for testing and validation, we can reduce the dependence of the datasets (Figure 3.3c). We use a bin size of 30 arc minutes ($\sim$ 50 km at the equator) to group records, and then randomly select those bins for training, validation, and testing. This bin size could be made larger or smaller, or it could be made to vary based on prior knowledge of seafloor roughness, but it's important not to tune the bin size by model loss performance. The training, validation, and testing datasets comprise 31,320,896, 10,460,197, and 10,472,576 records respectively.

### 3.2.3 Model architecture and training

We use the TensorFlow software library to design and train the neural network (Abadi et al.; 2015). The neural network comprises only successive densely-connected layers using a ReLU activation function (Figure 3.2). Input features are normalized by the mean and variance of their distribution in the training dataset. We use eight successive dense layers with 256 neurons per layer, and a final linear output layer. Model architecture can be tweaked ad nauseum, so we cannot claim this is a strictly optimal configuration, but this particular arrangement was selected

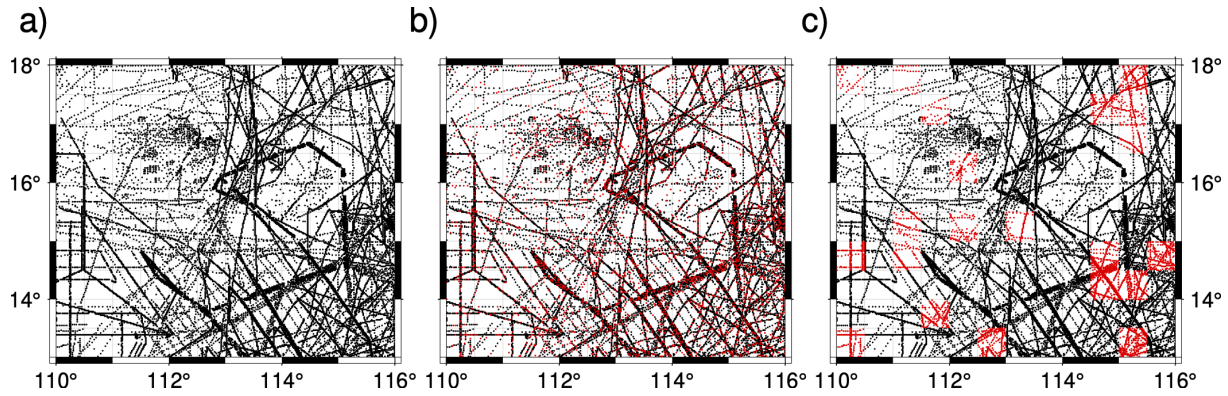


**Figure 3.3.** An example of partitioning the data. Same map area shown in Figure 3.1b-e. (a) The collection of depth measurements. The data must be partitioned into a training, testing, and validation set. (b) Randomly withholding 20% of the data, sampled uniformly. Withheld data are shown in red. Using this partition scheme, almost any withheld point has a nearly identical point in the training set, so the sets are not independent. (c) Sampling the data after binning into groups of 30 arc minutes. Withheld data are shown in red.

because we found it performed as well as a wider but shallower model (e.g., 4 layers of 1024 neurons each) while using far fewer parameters (4e5 vs. 3e6).

We choose mean squared error (MSE) as the loss function. Each dense layer is regularized with L2 regularization ($\lambda = 0.01$). We use the Adam optimizer (Kingma and Ba; 2017) with a learning rate of 0.001. Model training proceeds until the validation loss is no longer decreasing.

### 3.2.4 Inference: generating the global predicted grid

The end goal of this model is a global grid of predicted depths. After the model is trained, predictions of $h$ are generated on a 1 arcminute spherical mercator grid (on-shore values are masked). The long wavelength depth, saved from the filtering step, are added to the predicted depth, $h$, to give absolute depth, $d$. Finally, for distribution, the predicted depth grid is "polished" with the constrained depth measurements, but this step is omitted in the following discussion and analysis.

## 3.3 Results

### 3.3.1 Base model

Using the feature vector $[\phi_s, \phi_c, \theta, g^*]$ to predict $h$, we achieve a training RMSE of 85 m, validation RMSE of 108 m, and testing RMSE of 109 m. Loss values are useful for comparing one trained model against another, but they are imperfect when comparing to the Nettleton method. Since no "testing" data is withheld from the Nettleton method (i.e., the prediction is tuned on all available data), we must caution the comparison of RMSE between the two methods. With that in mind, the RMSE of the Nettleton prediction and $h$ is about 143 m. We will look more carefully at model misfit in the discussion.

**Modeling without filtering depths and gravity**

For comparison, a model trained without filtering depths and gravity anomaly performs much worse and offers no improvement over the Nettleton method. For this model, we achieve a training RMSE of 140 m, validation RMSE of 173 m, and testing RMSE of 175 m. This poor performance may be because the distribution of depth is more variable with location. For example, where the regional depth is 6000 m, the mean depth will be near 6000 m, and similar for a regional depth of 1000 m. By high-pass filtering the depth, the overall variance of the data are reduced. Omitting the low-pass filter at 16 km also contributes to the worse performance. The Nettleton method RMSE above is for the band-pass filtered data, $h$. If the short wavelengths are included, the Nettleton RMSE is about 165 m.

Alternatively, we can high-pass filter depth and gravity but omit the low-pass filter at 16 km–in fact, we may desire to do this so we don't lose short-wavelength details. For this model, we achieve a training RMSE of 124 m, validation RMSE of 141 m, and testing RMSE of 142 m. We can't compare these directly to the base model since the target quantities are different. Instead we can evaluate the RMSE of the base model prediction and the high-pass depth. In this case, testing RMSE values are nearly identical for the two models, suggesting the trained models

are similar and the greater loss reflects the greater variance of the target data.

### 3.3.2 Added features

It would seem that adding features from other global grids would be an easy way to decrease model loss and improve performance. For example, the spreading rate at the time crust is created is known to affect the roughness of bathymetry (Small and Sandwell; 1994). Crustal age and sediment cover will also influence the correlation of gravity and bathymetry (Smith and Sandwell; 1994). We use $\phi, \theta$ to sample grids of crustal age, paleo-spreading rate (Seton et al.; 2020), and sediment thickness (Whittaker et al.; 2013), add these to the feature vector, and train a new model. In practice, there are problems with using these features.

Firstly, these grids have many regions of missing data, and the missing values must be handled somehow. Since a key purpose of this model is prediction on a global grid, grid cells with missing values can't simply be thrown out. We tested different schemes to replacing missing values: replacement with the mean feature value; replacement with mean feature value plus an additional boolean feature indicating replacement; and filling missing values with nearest neighbor interpolation of the feature grid. In our attempts to use crustal age, paleo-spreading rate, and sediment thickness as features, validation and testing loss are not improved (nor are they improved by any one such feature), and in fact model loss is worse with the additional features. In addition, at inference time, sharp discontinuities in the feature grids get mapped to the prediction grid creating unwanted artifacts.

Other gravity-related quantities such as deflection of the vertical and vertical gravity gradient (VGG) may be good features to use, but they may only be redundant. We found that adding VGG as a feature (Sandwell et al.; 2021) improves model training RMSE only slightly, and it slightly worsens validation and testing RMSE. This model has a training RMSE of 85 m, a validation RMSE of 109 m, and a testing RMSE of 110 m. Since there is no improvement on the base model, we will consider that the preferred model and refer to it as simply the "DNN" model in the following discussion.

## 3.4 Discussion

### 3.4.1 Generating a predicted depth grid

After training, we generate model predicted depths on a global 1 min mercator grid. One problem that results is short wavelength artifacts or "hallucinations" (Figure 3.4e). These hallucinations typically occur with wavelengths shorter than the 16 km wavelength filter that was applied to the original gravity and bathymetry, so they must be a product of the DNN training. We can reduce these with regularization during training, but not completely nor in a deterministic way. For the distributed predicted depth grid, we apply a low pass filter with 0.5 gain at 16 km to remove these hallucinations. This post-inference filtering method does not weaken model results. In fact, error metrics are very slightly improved, and the prediction RMSE of $h$ after filtering is 107 m for the testing dataset. We use the predictions on the filtered grid in the following discussion.

### 3.4.2 Comparison to Nettleton model

While not quantitative, it's important to visually inspect the DNN predicted depth grid and make comparisons to the Nettleton grid (Figure 3.4). The most obvious qualitative difference is in continental margin areas or areas of relatively smooth seafloor. In these areas, the Nettleton predicted bathymetry has a rough "orange peel" texture (Figure 3.4d), an artifact of downward continuation of noisy gravity data. This type of seafloor is smoother in the DNN prediction.

Using all available depth measurements (not partitioned for training/testing), we compare the error distribution of the Nettleton method and the DNN method. These results are shown in Figure 3.5. For the Nettleton method, the predicted depth is within 68 m for 50% of points and within 168 m for 80% of points. For the DNN method, these percentiles are 45 m and 128 m, respectively. Additionally, the mean error has been reduced from 13 m for the Nettleton to 3 m for the DNN, indicating a less-biased estimate. Figure 3.5b shows the distribution of absolute model error in the southern oceans. Overall, the spatial patterns of misfit are similar for the two

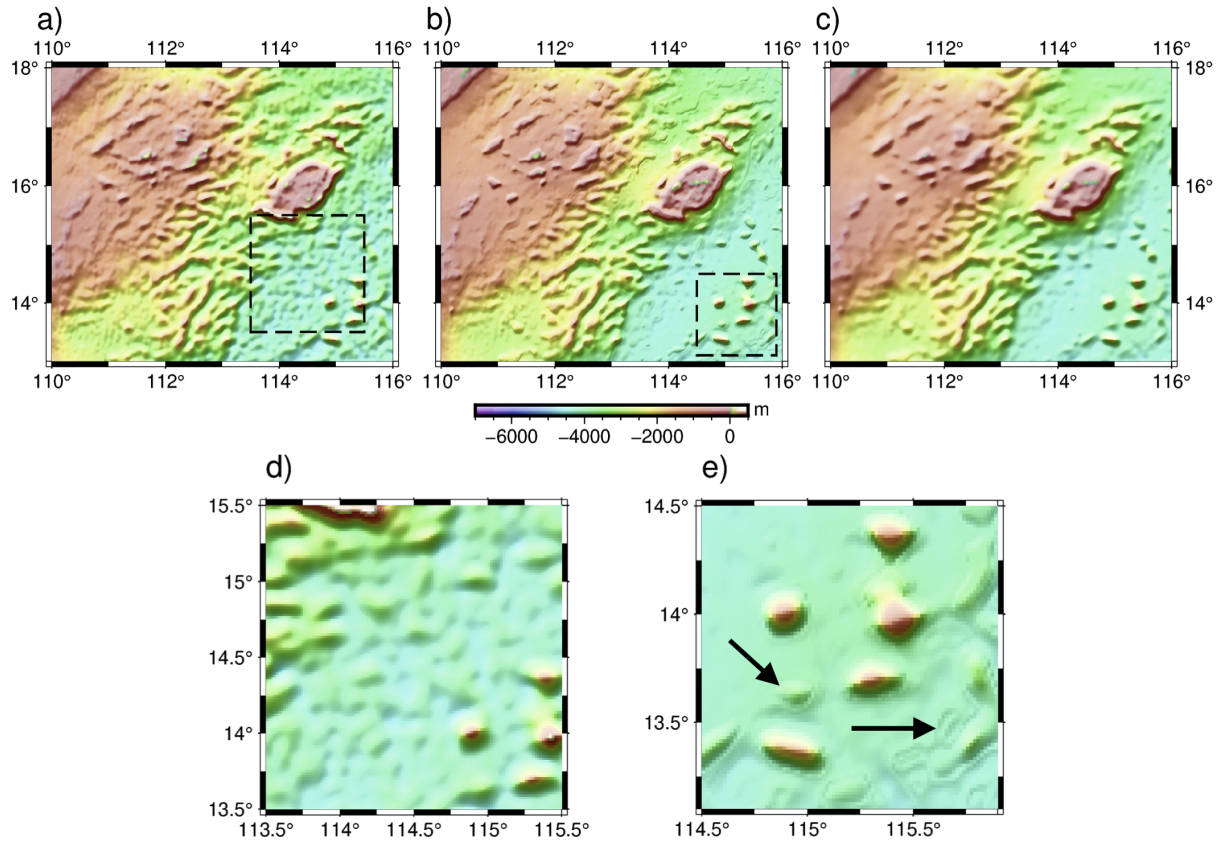


**Figure 3.4.** Model-predicted depths with long-wavelength depth added. The same map area shown in Figure 3.1b-e. (a) Nettleton method; (b) Raw DNN-predicted grid; (c) DNN-predicted grid, low-pass filtered at 12 km. (d) Example of the "orange peel" texture in the Nettleton prediction, boxed region in (a). (e) Example of "hallucinations" in DNN prediction, boxed region in (b).

models. At this scale, the noticeable differences are found nearer to land–e.g., the West Antarctic Peninsula, Chile, Australia–where the DNN model shows clear improvements over the Nettleton.

**BODC data**

Because the Nettleton prediction is tuned using all available data, we don't have a concrete idea of how well it generalizes to unseen areas of seafloor. It is useful to reserve a dataset that is not used in either model's construction. To compare the performance of the Nettleton and the DNN model, we used a collection of depth measurements from 279 cruises from the British Oceanographic Data Centre (BODC) that are not yet incorporated into the prediction model. The raw data are decimated to 15 sec, and measurements that overlap with data already in the prediction dataset are removed. We did not thoroughly inspect the BODC data for erroneous measurements, so measurements that differ from either predicted grid by more than 2000 m are removed. In total, there are 6,242,414 points. The Nettleton prediction has an RMSE of 150 m for the BODC dataset. The final DNN model has an RMSE of 104 m.

If we restrict the analysis spatially to the highest concentration of measurements (80% of the data are around the British Isles), the Nettleton RMSE is 73 m and the DNN model RMSE is 62 m–much lower than testing RMSE (Figure 3.6). This almost certainly reflects the proximity of these data to those in our training set. However, we see from the error distribution that the slight bias in the Nettleton prediction is not present in the DNN prediction.

### 3.4.3 Potential for improvements

Our model is a simple implementation of a neural network to predict depth globally, and we have shown its clear improvement over the Nettleton method. Yet, there are many possible directions for improvement depending on one's objectives. Expansion of the training dataset, modifications of model architecture, or a multi-regional approach to the problem all offer potential to improve on our model.

If coverage of publicly available bathymetry compilations continues to improve as it has

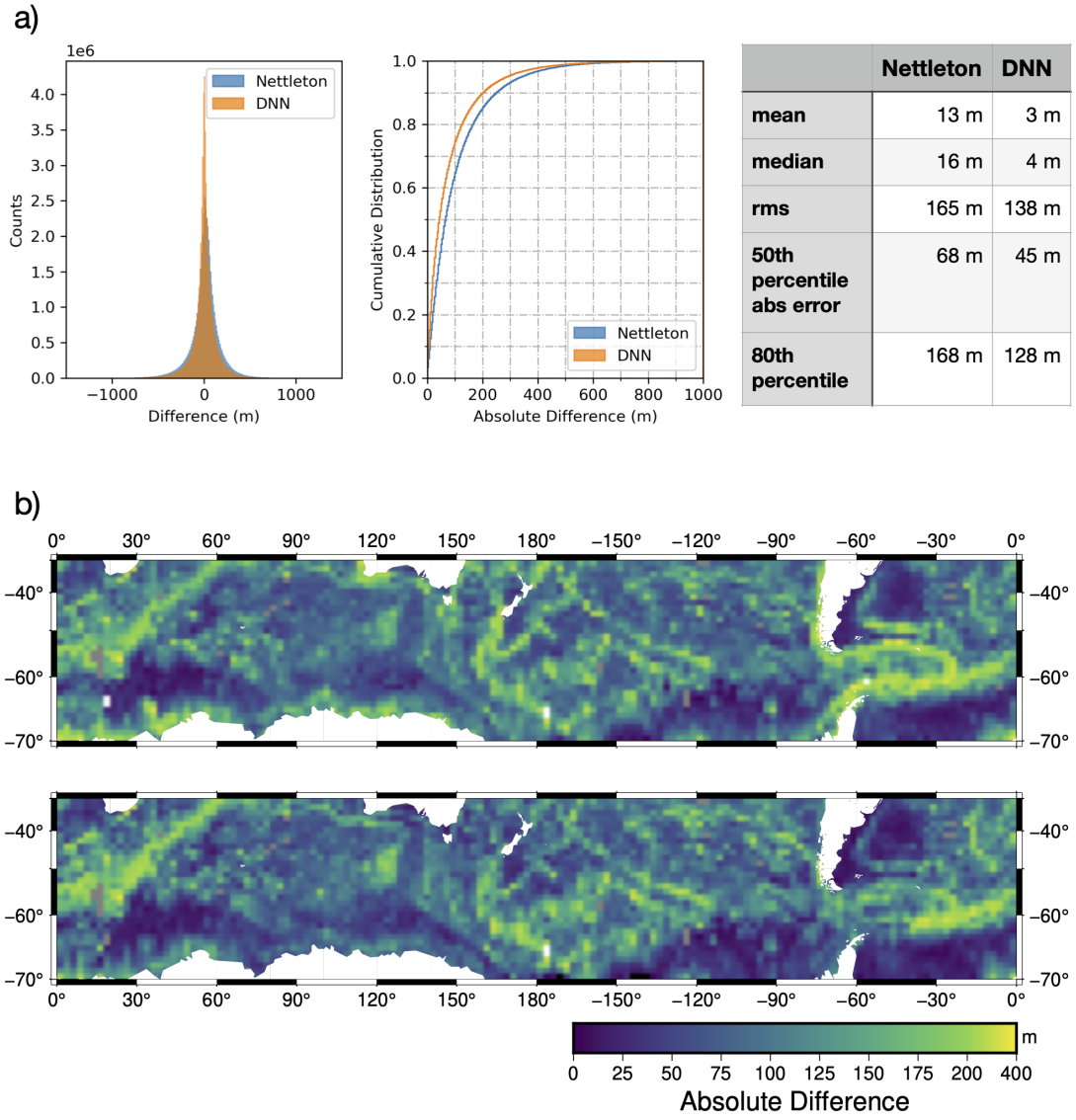


| | Nettleton | DNN |
|---|---|---|
| **mean** | 13 m | 3 m |
| **median** | 16 m | 4 m |
| **rms** | 165 m | 138 m |
| **50th percentile abs error** | 68 m | 45 m |
| **80th percentile** | 168 m | 128 m |

**Figure 3.5.** Comparison of Nettleton and DNN models by prediction error. (a) Distribution of prediction error for all 1 arc minute data (N=52,253,670). (b) Average absolute difference (prediction - measurement) for Nettleton (upper) and DNN (lower) models.

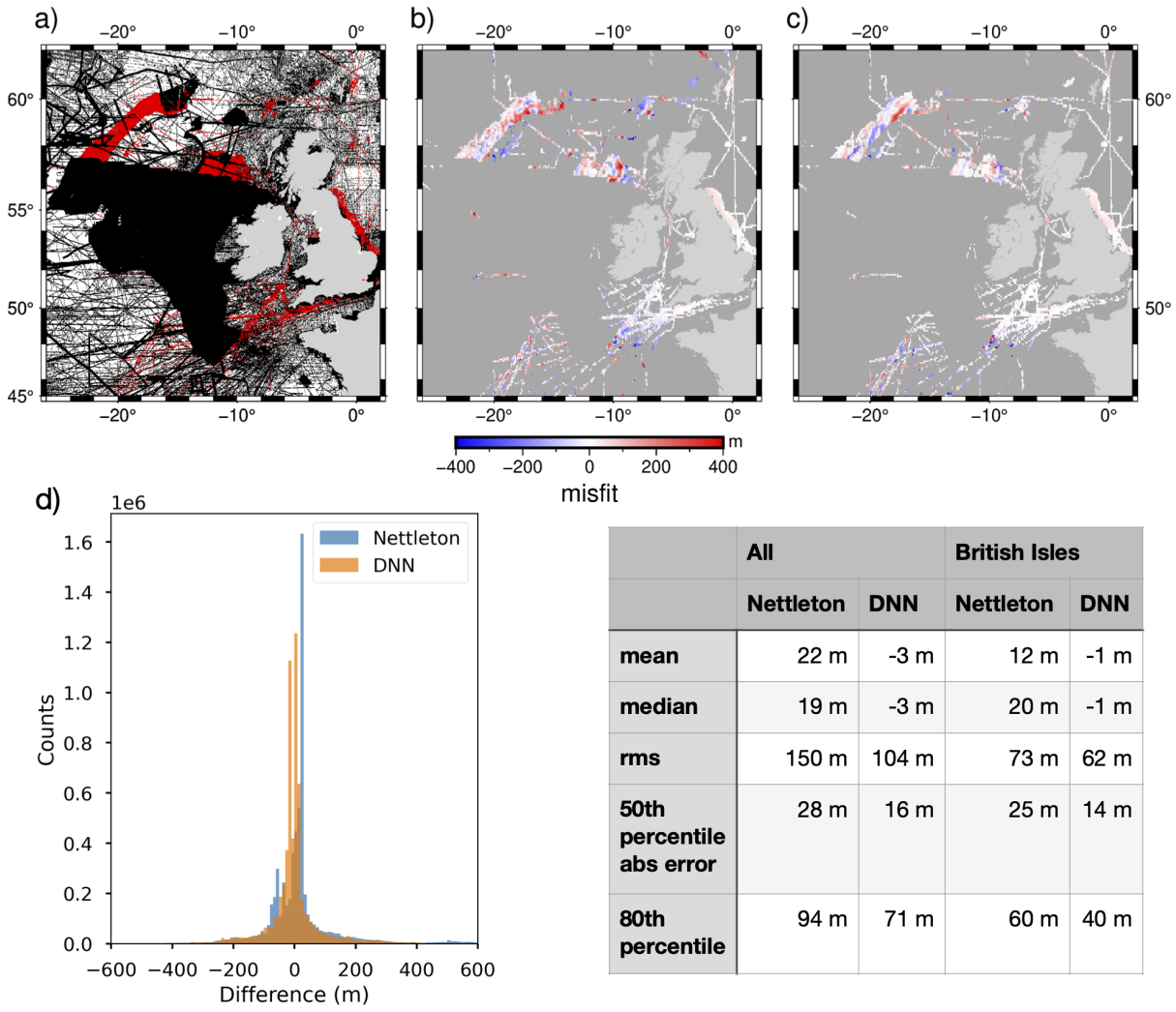


| | All | | British Isles | |
|---|---|---|---|---|
| | **Nettleton** | **DNN** | **Nettleton** | **DNN** |
| **mean** | 22 m | -3 m | 12 m | -1 m |
| **median** | 19 m | -3 m | 20 m | -1 m |
| **rms** | 150 m | 104 m | 73 m | 62 m |
| **50th percentile abs error** | 28 m | 16 m | 25 m | 14 m |
| **80th percentile** | 94 m | 71 m | 60 m | 40 m |

**Figure 3.6.** Nettleton and DNN model predictions for withheld BODC data. (a) Depth measurements in the full dataset shown in black, measurements from the disjoint BODC dataset shown in red. Misfit of BODC data for (b) Nettleton predicted depth and (c) neural network predicted depth. (d) Distribution of BODC data misfit for Nettleton predicted depth and neural network predicted depth.

in recent years–and it likely will (Mayer et al.; 2018)–model predictions will clearly improve (this would be true of any model). Low-resolution data in remote regions, which can be collected by autonomous vehicles, will likely offer the greatest benefit in our model approach.

We haven't made use of high-resolution multibeam data in our model, and we do not aim to predict features at such resolution. Upward continuation of gravity anomalies limits the resolution of gravity from satellite altimetry to a length scale of about $\pi$ times the regional depth (e.g Smith and Sandwell; 2004), so it is not possible to realistically predict depth from only gravity (and its derivatives) at such scales. An approach using convolutional neural networks, as demonstrated by Annan and Wan (2022), may successfully learn from higher resolution bathymetry in regional settings.

A prediction model trained on regional data will, everything else equal, perform better in that region than a model trained on global data. Moran et al. (2022) identified regions where various learning algorithms might preferentially excel. This suggests a global model should alternatively be constructed from a suite of regional models. A particular case where such a multi-regional model would excel is in predicting higher resolution depth in areas where that is realistic. Susa (2022) showed such an approach to predicting depth in near-coastal regions. In this setting, altimetric ranging and gravity accuracy suffer from land contamination (Raney and Phalippou; 2011), and visible spectra may be correlated with bathymetry, making this an ideal case for alternative depth prediction.

## 3.5 Conclusions

1. Using a large collection of depth measurements and satellite-derived gravity anomalies, we trained a deep neural network to predict seafloor depth.

2. We find that applying filters (described by Smith and Sandwell (1994)) to bathymetry and gravity before training is necessary for a good result, and conforms the data more closely with the assumption of identical distributions.

3. When dealing with sparse heterogeneous sampling, the training-testing split must be treated carefully. If the training and testing split is a random partition at the same resolution as the data, the training and testing sets are not independent, and model misfit results will be too optimistic.

4. Adding features sampled from geologic grids–crustal age, paleo-spreading rate, sediment thickness–do not improve model results.

5. Our preferred DNN-predicted model improves on the results of the Nettleton procedure, lowering the prediction RMSE from 165 m to 138 m.

6. While improvements will be made with additional depth measurement data, higher resolution predictions are limited by the upward continuation of gravity, so likely shouldn't be attempted with this method.

## 3.6 Acknowledgements

This chapter, in full, is currently being prepared for publication as Harper, H. and Sandwell, D. T. "Global predicted bathymetry using neural networks". The dissertation author was the primary investigator and author of this material.

# References


Abadi, M., Agarwal, A., Barham, P., Brevdo, E., Chen, Z., Citro, C., Corrado, G. S., Davis, A., Dean, J., Devin, M., Ghemawat, S., Goodfellow, I., Harp, A., Irving, G., Isard, M., Jia, Y., Jozefowicz, R., Kaiser, L., Kudlur, M., Levenberg, J., Mané, D., Monga, R., Moore, S., Murray, D., Olah, C., Schuster, M., Shlens, J., Steiner, B., Sutskever, I., Talwar, K., Tucker, P., Vanhoucke, V., Vasudevan, V., Viégas, F., Vinyals, O., Warden, P., Wattenberg, M., Wicke, M., Yu, Y. and Zheng, X. (2015). TensorFlow: Large-scale machine learning on heterogeneous systems. Software available from tensorflow.org.
**URL:** *https://www.tensorflow.org/*

Annan, R. F. and Wan, X. (2022). Recovering bathymetry of the gulf of guinea using altimetry-derived gravity field products combined via convolutional neural network, *Surveys in Geophysics* **43**: 1541–1561.

Becker, J. J., Sandwell, D. T., Smith, W. H., Braud, J., Binder, B., Depner, J., Fabre, D., Factor, J., Ingalls, S., Kim, S. H., Ladner, R., Marks, K., Nelson, S., Pharaoh, A., Trimmer, R., von Rosenberg, J., Wallace, G. and Weatherall, P. (2009). Global bathymetry and elevation data at 30 arc seconds resolution: Srtm30_plus, *Marine Geodesy* **32**: 355–371.

GEBCO compilation group (2023). Gebco 2023 grid.

Harper, H. and Sandwell, D. (2023). Global predicted bathymetry using neural networks.
**URL:** *https://doi.org/10.5281/zenodo.8029925*

Kingma, D. P. and Ba, J. (2017). Adam: A method for stochastic optimization.

Marks, K. M., Smith, W. H. and Sandwell, D. T. (2010). Evolution of errors in the altimetric bathymetry model used by google earth and gebco, *Marine Geophysical Research* **31**: 223–238.

Mayer, L., Jakobsson, M., Allen, G., Dorschel, B., Falconer, R., Ferrini, V., Lamarche, G., Snaith, H. and Weatherall, P. (2018). The nippon foundation-gebco seabed 2030 project: The quest to see the world's oceans completely mapped by 2030, *Geosciences (Switzerland)* **8**.

Moran, N., Stringer, B., Lin, B. and Hoque, M. T. (2022). Machine learning model selection for predicting bathymetry, *Deep-Sea Research Part I: Oceanographic Research Papers* **185**: 103788.

Nettleton, L. L. (1939). Determination of density for reduction of gravimeter observations, *Geophysics* **4**.

Parker, R. (1972). The rapid calculation of potential anomalies, *Geophysical Journal of the*

*Royal Astronomical Society* **31**: 447–455.

Raney, R. K. and Phalippou, L. (2011). *The Future of Coastal Altimetry*, Springer Berlin Heidelberg, Berlin, Heidelberg, pp. 535–560.

Sandwell, D. T., Harper, H., Tozer, B. and Smith, W. H. (2021). Gravity field recovery from geodetic altimeter missions, *Advances in Space Research* **68**(2): 1059–1072.

Seton, M., Müller, R. D., Zahirovic, S., Williams, S., Wright, N. M., Cannon, J., Whittaker, J. M., Matthews, K. J. and McGirr, R. (2020). A global data set of present-day oceanic crustal age and seafloor spreading parameters, *Geochemistry, Geophysics, Geosystems* **21**: 1–15.

Small, C. and Sandwell, D. T. (1994). Imaging mid-ocean ridge transitions with satellite gravity, *Geology* **22**: 123–126.

Smith, W. H. F. (1998). Seafloor tectonic fabric from satellite altimetry, *Annual Review of Earth and Planetary Sciences* **26**: 697–738.

Smith, W. H. and Sandwell, D. T. (1994). Bathymetric prediction from dense satellite altimetry and sparse shipboard bathymetry, *Journal of Geophysical Research* **99**.

Smith, W. H. and Sandwell, D. T. (1997). Global sea floor topography from satellite altimetry and ship depth soundings, *Science* **277**: 1956–1962.

Smith, W. H. and Sandwell, D. T. (2004). Conventional bathymetry, bathymetry from space, and geodetic altimetry, *Oceanography* **17**: 8–23.

Smith, W. H. and Wessel, P. (1990). Gridding with continuous curvature splines in tension, *Geophysics* **55**(3): 293–305.

Susa, T. (2022). Satellite derived bathymetry with sentinel-2 imagery: Comparing traditional techniques with advanced methods and machine learning ensemble models, *Marine Geodesy* **0**: 1–20.

Tozer, B., Sandwell, D. T., Smith, W. H., Olson, C., Beale, J. R. and Wessel, P. (2019). Global bathymetry and topography at 15 arc sec: Srtm15+, *Earth and Space Science* **6**: 1847–1864.

Wan, X., Annan, R. F. and Ziggah, Y. Y. (2023). Altimetry-derived gravity gradients using spectral method and their performance in bathymetry inversion using back-propagation neural network, *Journal of Geophysical Research: Solid Earth* **128**.

Watts, A. B. (2001). *Isostasy and Flexure of the Lithosphere*, Cambridge University Press.

Whittaker, J. M., Goncharov, A., Williams, S. E., Müller, R. D. and Leitchenkov, G. (2013).

Global sediment thickness data set updated for the australian-antarctic southern ocean, *Geochemistry, Geophysics, Geosystems* **14**(8): 3297–3305.

# Chapter 4

# Conclusions

We began this thesis introducing the powerful method of gravity from satellite altimetry, a means by which we can image the ocean floor where conventional maps don't exist. In the first two chapters, we used maps of gravity anomalies and vertical gravity gradients to focus our investigation on a class of tectonic features we call "seesaw" propagators. In chapter 1, we documented the global distribution of seesaw propagators, analyzed their distribution and nature with respect to tectonic setting and tested mechanisms to explain their formation and behavior. We showed that seesaw ridge propagation is a ubiquitous phenomenon that occurs at slow and intermediate spreading ridges and that SSPs form almost exclusively at ridge offsets with lithospheric age contrasts less than $\sim$2.5 Ma (or $\sim$30 km).

In chapter 2, we examined the offset length threshold identified in chapter 1, and sought to explain why ridge propagation should cease when an offset grows larger than about 30 km. We hypothesized that the strength of the lithosphere at a ridge offset limits whether a ridge can propagate and that this could explain the threshold offset length between propagating ridges and transform faults. Adapting a framework developed by earlier workers, we tested this hypothesis on observed transform faults, propagating ridges/migrating offsets, and observed SSPs. Some aspects of the model framework were unsuccessful, but it's clear that SSPs are a population distinct from stable transform faults. It stands that the weak lithosphere at small offsets is essential to produce ridge propagation and, conversely, that strong lithosphere at transform faults

contributes to their stability.

There are still remaining questions regarding SSPs and the behavior of small ridge offsets, some of which could be answered at this time. For example: can features like SSPs help constrain crustal age grids and plate tectonic reconstructions? Because SSPs are symmetric about ridge axes, the inflection points (where propagation reverses direction) of fossil SSPs can be used as a relative age constraint as these points must meet at the ridge axis when reconstructed to their time of formation. These inflection point pairs may aid in developing plate reconstruction models, help refine the global age grid, and reveal details of past basin opening.

Full three-dimensional thermomechanical modeling of even simple mid-ocean ridge processes is very complicated (Gerya; 2013). Replicating previous simpler simulations (e.g. Behn et al.; 2002, 2007) and focusing on small ridge offsets may help understand the fundamental differences between short and long ridge offsets. Similar to Shi et al. (2022), an analysis of seismic moment release rate with a focus on short vs long offsets may yield enlightening results. Since we suggest coupling varies with offset length, we might expect moment release per unit length to decrease sharply around the same threshold we observe.

Chapter 3 was a departure from the subject of the first two chapters. We sought to update the method of depth prediction in unmapped ocean areas. Using a large collection of depth soundings and satellite-derived gravity anomalies, we trained a deep neural network to predict seafloor depth. We found high-pass filtering depth and gravity according to the admittance theory laid out by (Smith and Sandwell; 1994) was necessary for result that improved upon the old "Nettleton" model. Our preferred DNN-predicted model improved on the results of the Nettleton procedure, lowering the prediction RMSE from 165 m to 138 m.

There was a subtle point we believe bears repeating: when dealing with sparse heterogeneous sampling, the training-testing split must be treated carefully. If the training and testing split is a random partition at the same resolution as the data, the training and testing sets are not independent, and model misfit results will be too optimistic. We also recommended a few possibilities for improving the prediction model (there are many), but suggest higher resolution

predictions are limited by the upward continuation of gravity, so likely shouldn't be attempted with this method.

We've said that less than 25% of the seafloor has been mapped at a resolution of 15 arcseconds, but only a few years ago, this figure was closer to 18% Mayer et al. (2018). Part of this impressive increase can be attributed to the Seabed 2030 project, which aims to aggregate all available bathymetric data and facilitate data collection to produce the definitive map of the world ocean floor by 2030. Of course, incremental improvements in coverage will improve accuracy of predicted depth models, but it is unlikely that the extent of the oceans will be fully surveyed in this time. (That may be a product of wishful thinking since it will render my special skill obsolete).

Underlying all of this work is the recovery of gravity from satellite altimeters. Over the course of this dissertation, the recovery of gravity from satellite altimeters has been incrementally improved by the altimeters SARAL/AltiKa, Jason-2 (deactivated 2019), and Cryosat-2. The result is a gravity field with 1 mgal accuracy in many places (Sandwell et al.; 2021)–this is essentially as good as shipboard gravimetry (Smith and Sandwell; 2004), albeit at lower spatial resolution. SWOT, an entirely new type of altimeter that images 2-D swaths rather than the nadir, was launched in late 2022. This new mission will improve the resolution of the gravity field, particularly in the cross-track direction, and help us understand the spatial variability of noise sources such as ocean waves. At the time of this writing, the SWOT altimeter is active, but data are not yet available. It will likely be a few years before the power of SWOT can be fully realized.

# References


Behn, M. D., Boettcher, M. S. and Hirth, G. (2007). Thermal structure of oceanic transform faults, *Geology* **35**: 307–310.

Behn, M. D., Lin, J. and Zuber, M. T. (2002). Evidence for weak oceanic transform faults, *Geophysical Research Letters* **29**: 1–4.

Gerya, T. V. (2013). Three-dimensional thermomechanical modeling of oceanic spreading initiation and evolution, *Physics of the Earth and Planetary Interiors* **214**: 35–52.

Mayer, L., Jakobsson, M., Allen, G., Dorschel, B., Falconer, R., Ferrini, V., Lamarche, G., Snaith, H. and Weatherall, P. (2018). The nippon foundation-gebco seabed 2030 project: The quest to see the world's oceans completely mapped by 2030, *Geosciences (Switzerland)* **8**.

Sandwell, D. T., Harper, H., Tozer, B. and Smith, W. H. (2021). Gravity field recovery from geodetic altimeter missions, *Advances in Space Research* **68**(2): 1059–1072.

Shi, P., Wei, M. M. and Pockalny, R. A. (2022). The ubiquitous creeping segments on oceanic transform faults, *Geology* **50**: 199–204.

Smith, W. H. and Sandwell, D. T. (1994). Bathymetric prediction from dense satellite altimetry and sparse shipboard bathymetry, *Journal of Geophysical Research* **99**.

Smith, W. H. and Sandwell, D. T. (2004). Conventional bathymetry, bathymetry from space, and geodetic altimetry, *Oceanography* **17**: 8–23.